SURFACE LOCALIZED SUB-BANDGAP STATES IN LEAD CHALCOGENIDE NANOCRYSTALS

by

CHRISTIAN F. GERVASI

A DISSERTATION

Presented to the Department of Chemistry and Biochemistry
and the Division of Graduate Studies of the University of Oregon
in partial fulfillment of the requirements
for the degree of
Doctor of Philosophy

June 2022

DISSERTATION APPROVAL PAGE

Student: Christian F. Gervasi

Title: Surface Localized Sub-Bandgap States in Lead Chalcogenide Nanocrystals

This dissertation has been accepted and approved in partial fulfillment of the requirements for the Doctor of Philosophy degree in the Department of Chemistry and Biochemistry by:

Michael E. Kellman	Chairperson
George V. Nazin	Advisor
James E. Hutchison	Core Member
Hailin Wang	Institutional Representative

and

Krista Chronister	Vice Provost for Graduate Studies

Original approval signatures are on file with the University of Oregon Division of Graduate Studies.

Degree awarded June 2022

DISSERTATION ABSTRACT

Christian F. Gervasi

Doctor of Philosophy

Department of Chemistry and Biochemistry

June 2022

Title: Surface Localized Sub-Bandgap States in Lead Chalcogenide Nanocrystals

In our information technology-based world semiconductors are essential to our modern way of life, they are the basis upon which the vast majority of our modern optoelectronic and computing technologies work. As industry has sought to increase performance, decrease the size and cost, and expand the capabilities of these technologies, nano-materials such as semiconducting nanocrystals are playing an ever-larger role in achieving these objects. Indeed, semiconducting nanocrystals are quickly gaining industry acceptance in an array of technological applications including flat screen displays, photovoltaics, lasers, chemical sensing and medical imaging applications, among others.

The versatility of semiconducting nanocrystals derives from their superlative opto-electronic and charge transport properties, the chief of which is their ability to efficiently absorb and emit light, across the visible and near-infrared regions of the electromagnetic spectrum. The tunability of photon absorption and emission in semiconducting nanocrystals is based on factors such as chemical composition and stoichiometry, size, and crystal morphology. This tunability allows for the production of nanocrystals with frequency-specific light emission and absorption characteristics, important for many evolving technologies. Semiconductor nanocrystal charge transport capabilities and the ability for charge carrier manipulation, such as multiple exciton generation (MEG), present other avenues for technological innovation and improved efficiency over current semiconductor-based technologies. Most importantly, as a result of their solution processability, as opposed to

traditional semiconductor manufacturing processes, technologies based on semiconducting nanocrystal have the potential for vast improvements in production efficiency, waste reduction, and considerable savings with respect to energy consumption and cost.

Semiconducting nanocrystal technologies present scientists and engineers an array of options for novel device functionalities and architectures. However, because of their size and surface to volume ratio, the optoelectronic properties of semiconducting nanocrystal QDs are susceptible to significant perturbations depending on the surface chemistry and crystal defects, as well as internal composition and structure. Chemical and structural irregularities at their surfaces can lead to substantial alteration of their optoelectronic properties, presenting headaches, but also avenues of exploitation for scientists and device engineers. The research presented in this dissertation explores the existence of sub-bandgap states in PbS nanocrystals' electronic structure due to differing local surface stoichiometry and surface reconstruction resulting from removal, or lack of passivating ligands.

CURRICULUM VITAE

NAME OF AUTHOR: Christian F. Gervasi

GRADUATE AND UNDERGRADUATE SCHOOLS ATTENDED:

University of Oregon, Eugene, Oregon
Southern Oregon University, Ashland, Oregon
University of Portland, Portland, Oregon

DEGREES AWARDED:

Doctor of Philosophy, Chemistry, 2022, University of Oregon
Bachelor of Science, Physics, 2012, Southern Oregon University
Bachelor of Arts, Performing Arts, 1999, University of Portland

AREAS OF SPECIAL INTEREST:

Semiconductor Nanocrystal Quantum Dots
Carbon nanotubes
Scanning Tunneling Microscopy and Spectroscopy
Density Functional Theory

PROFESSIONAL EXPERIENCE:

Graduate Research Assistant, Department of Chemistry and Biochemistry, University of Oregon, Eugene, OR, 2013-2018

Graduate Teaching Assistant, Department of Chemistry and Biochemistry, University of Oregon, Eugene, OR, 2012-2013, 2017-2018

Science Literacy Program Fellow, Department of Chemistry and Biochemistry, University of Oregon, Eugene, OR, 2017

Lecturer, Department of Chemistry and Biochemistry, University of Oregon, Eugene, OR, 2018-2021

GRANTS, AWARDS, AND HONORS:

Graduate Student Award for Excellence in the Teaching of Chemistry,
Department of Chemistry and Biochemistry, University of Oregon, 2012-2013

PUBLICATIONS:

Kislitsyn, D. A.; Gervasi, C. F.; Allen, T.; Palomaki, P. K. B.; Hackley, J. D.; Maruyama, R.; Nazin, G. V. Spatial Mapping of Sub-Bandgap States Induced by Local Nonstoichiometry in Individual Lead Sulfide Nanocrystals. *J. Phys. Chem. Lett.* **2014,** 5 (21), 3701–3707.

Gervasi, C. F.; Kislitsyn, D. A.; Allen, T. L.; Hackley, J. D.; Maruyama, R.; Nazin, G. V. Diversity of Sub-Bandgap States in Lead-Sulfide Nanocrystals: Real-Space Spectroscopy and Mapping at the Atomic-Scale. *Nanoscale* **2015**, 7 (46), 19732–19742.

Taber, B. N.; Kislitsyn, D. A.; Gervasi, C. F.; Mannsfeld, S. C. B.; Zhang, L.; Briseno, A. L.; Nazin, G. V. Adsorption-Induced Conformational Isomerization of Alkyl- Substituted Thiophene Oligomers on Au(111): Impact on the Interfacial Electronic Structure. *ACS Appl. Mater. Interfaces* **2015**, 7 (28), 15138–15142.

Kislitsyn, D. A.; Taber, B. N.; Gervasi, C. F.; Mannsfeld, S. C. B.; Zhang, L.; Briseno, A. L.; Nazin, G. V. Coverage-Dependent Self-Assembly Regimes of Alkyl- Substituted Thiophene Oligomers on Au(111): Scanning Tunneling Microscopy and Spectroscopy. *J. Phys. Chem. C* **2015**, 119 (48), 26959–26967.

Kislitsyn, D. A.; Taber, B. N.; Gervasi, C. F.; Zhang, L.; Mannsfeld, S. C. B.; Prell, J. S.; Briseno, A. L.; Nazin, G. V. Oligothiophene Wires: Impact of Torsional Conformation on the Electronic Structure. *Phys. Chem. Chem. Phys.* **2016**, 18 (6), 4842– 4849.

Taber, B. N.; Kislitsyn, D. A.; Gervasi, C. F.; Mills, J. M.; Rosenfield, A. E.; Zhang, L.; Mannsfeld, S. C. B.; Prell, J. S.; Briseno, A. L.; Nazin, G. V. Real-Space Visualization of Conformation-Independent Oligothiophene Electronic Structure. J. Chem. Phys. 2016, 144 (19), 194703.

Kislitsyn, D. A.; Kocevski, V.; Mills, J. M.; Chiu, S.-K.; Gervasi, C. F.; Taber, B. N.; Rosenfield, A. E.; Eriksson, O.; Rusz, J.; Goforth, A. M.; et al. Mapping of Defects in Individual Silicon Nanocrystals Using Real-Space Spectroscopy. J. Phys. Chem. Lett. 2016, 7 (6), 1047–1054.

Kislitsyn, D. A.; Mills, J. M.; Kocevski, V.; Chiu, S.-K.; DeBenedetti, W. J. I.; Gervasi, C. F.; Taber, B. N.; Rosenfield, A. E.; Eriksson, O.; Rusz, J.; et al. Communication: Visualization and Spectroscopy of Defects Induced by Dehydrogenation in Individual Silicon Nanocrystals. J. Chem. Phys. 2016, 144 (24), 241102.

Taber, B. N.; Gervasi, C. F.; Mills, J. M.; Kislitsyn, D. A.; Darzi, E. R.; Crowley, W. G.; Jasti, R.; Nazin, G. V. Quantum Confinement of Surface Electrons by Molecular Nanohoop Corrals. J. Phys. Chem. Lett. 2016, 3073–3077.

Kislitsyn, D. A.; Mills, J. M.; Chiu, S. K.; Taber, B. N.; Barnes, J.D.; Gervasi, C. F.; Goforth, A. M.; Nazin, G. V. Creation and Annihilation of Charge Traps in Silicon Nanocrystals: Experimental Visualization and Spectroscopy. *J. Phys. Chem. Lett.* **2018**, 9, 710-719.

To be published journal article of Ab-Initio DFT calculations of the effect of surface reconstruction on Lead-sulfide.

ACKNOWLEDGMENTS

I wish to express sincere appreciation to my advisor, George Nazin, a continuous source of academic and intellectual rigor. Also, to my funny, diligent, sometimes infuriating and variously talented lab-mates, Benjamin Tabor, Jon Mills, Dmitry A. Kislitsyn, Jason Hackley, Motoaiki Honda, and Hank Seeley, and honorary member Thomas Allen; the scientific discoveries we made together were truly the result of a team effort and I could not have succeeded without their knowledge, efforts and support. I am also deeply grateful for my many passionate and engaging mentors for ongoing inspiration, wisdom and opportunities, with special thanks to Andreas Stonas, Deborah Exton, Thomas Greenbowe, Michael Kellman, and Mark Lonergan.

To my family, especially my spirited and vivacious wife, fiercely loving and devoted mother, generous brothers, and caring mother in law for all the time, patience, childcare and support they have provided along the path of my research and study. And to my father, I offer unending gratitude for always believing in me and trusting in my path.

I would like to offer special thanks to Jennifer Jess, Natalie Dunn, and all the student clerks at Science Stores for “holding down the fort” on the many occasions when the writing of this dissertation would not wait any longer. To Ellen Siem, who introduced me to the brutality of physics examinations that taught me the value of resilience, and stamina. To Doug Chapman for his effervescent and stimulating lectures. To Peter Ka-Chai Wu, and George Quainoo for their firm and guiding influences. To Christopher Thompson, for being there and always being willing to listen.

To my family, especially my loving and very patient wife Viola, you always supported me when the going got rough, tough, and at times went off the rails.

TABLE OF CONTENTS

Chapter Page

I. INTRODUCTION 1

1.1 Very Small Things Can Have a Big Effect 1

1.2 Semiconducting Nanocrystal Quantum Dots 3

1.3 Introduction to Quantum Tunneling and Scanning Tunneling Microscopy 5

1.4 Scanning Tunneling Microscopy and Spectroscopy in Practice 7

1.5 Dissertation Summary 11

II. SPATIAL MAPPING OF SUB-BANDGAP STATES INDUCED BY LOCAL NON-STOICHIOMETRY IN INDIVIDUAL LEAD-SULFIDE NANOCRYSTALS 15

2.1 Introduction 15

2.2 Experimental Methods 16

2.3 Experimental Findings 18

2.4 Conclusions 29

2.6 Acknowledgements 29

2.6 Bridge 29

III. DIVERSITY OF SUB-BANDGAP STATES IN LEAD-SULFIDE NANOCRYSTALS: REAL-SPACE SPECTROSCOPY AND MAPPING AT THE ATOMIC-SCALE 30

3.1 Introduction 30

3.2 Experimental Methods 34

3.3 Experimental Results 35

3.3.1 Sample Preparation 35

3.3.2 Density of States Spectroscopy of NCs 37

3.3.3 Surface-Reconstruction Observed in Density of States Spectroscopy: Results 40

3.3.4 Surface-Reconstruction: Discussion 45

3.3.5 NCs with Edge-Defects 49

3.4 Conclusion 54

3.5 Acknowledgements 55

3.6 Bridge 55

IV. IMPACT OF SURFACE RECONSTRUCTION ON THE ELECTRONIC STRUCTURE OF LEAD-SULFIDE: Ab INITIO DENSITY FUCNTIONAL THEORY CALCULATIONS 56

4.1 Introduction 56

4.2 DFT Theoretical Methods 62

4.3 Theoretical Modeling Results and Discussion 65

4.3.1 Slab Relaxation Calculations, Surface Energy and Lowdin Population Analysis 65

4.3.2 Electronic Structure 70

4.3.2.1 Super-Cell Brillouin Zone (SBZ) Band Diagram Dispersion Characteristics 70

4.3.2.2 Atomic Orbital Projection onto SBZ Bands 81

4.3.2.3 Projected Density of States 84

4.3.3 Electron Probability Density Cross-sections 86

4.3.4 Effective Band Structure; Band Unfolding and PC Eigenstate Contribution 100

4.3.4.1 Band Unfolding Methodology; A Brief Discussion 100

4.3.4.2 Band Unfolding and the Resultant Effective Band Structure . 103

4.4 Conclusion 108

V. CONCLUSION 110

APPENDICES 114

A. SUPPORTING MATERIAL FOR CHAPTER II 114

B. SUPPORTING MATERIAL FOR CHAPTER III 120

C. APPENDIX TITLE IN ALL CAPS 00

REFERENCES CITED 128

LIST OF FIGURES

Figure Page

2.1 Representative dI/dV spectra for five PbS NCs (Set point voltages and currents range from 1.2 V to 2.5 V, and 10 pA to 30 pA for the spectra shown). The bias voltage effectively serves as the energy scale (see, however, discussion associated with Figure S2 for a more complete description of the relationship between the bias voltage and energy). Occupied and unoccupied states are indicated by arrows and marked with an 'H' and 'E' for holes and electrons respectively. The apparent band gaps for each of the NCs are marked with double sided arrows. 19

2.2 STM/STS characterization of a representative nanocrystal NC_1. (a) STM topography image of NC_1 [set point 1.0 V, 1.0 pA]. (b) Topographical features attributable to step edges oriented along specific crystallographic directions. The majority of features indicate 120° angles, which suggests that the top facet of NC_1 corresponds to a {111} plane. (c) A cross-section of the topography [path indicated by the arrow in (a)] showing that the top facet of NC_1 is at a small angle with respect to the Au(111) surface. Individual steps are marked with dashed lines, with the step height (0.342 nm) corresponding to the distance between the sulfur {111} planes. (d) A representative STS spectrum [set point 2.0 V, 15 pA] measured at the location marked by the star in (a). Prominent occupied and unoccupied states are marked with an 'H' and 'E' respectively. 20

2.3 Spatial STS mapping across nanocrystal NC_1. (a) Topographic image [set point 1.0 V, 1 pA] showing the path of mapping (points P_1 through P_5). (b) Density of states [set point 2.0 V, 10 pA] as a function of bias voltage and position x along the path shown in (a). (c) Individual STS spectra from (b) measured at points P_2 through P_5. Occupied and unoccupied states are marked 'H' and 'E' respectively in both (b) and (c). Spectral feature H^{**} corresponds to “reverse” tunneling[31-32] through a localized occupied state outside of the mapping path. ... 22

2.4 (a) Topographic images of NC_1 [set point 1.0 V, 1 pA]. Bottom image is marked to indicate step edges with 120° angles oriented along <110> directions, the same set of marks is used in the bottom images of (b) and (c) for reference. (b) DOS maps for unoccupied states of NC_1 [set point 2.0 V, 15 pA] measured at the indicated bias voltages. Parallel dashed red lines indicate the apparent orientation of stripe-like features associated with states $E_{1,n}$. (c) DOS maps for occupied states of NC_1 [set point 2.0 V, 15 pA] measured at the indicated bias voltages. High intensity signals in the top left and top right of the H_2 map in (c) are attributed to spectral features of nearby NCs. The spatial extent of maps in (b) and (c) corresponds to the yellow rectangle shown in (a). Numbered markers in the bottom images of (b) and (c) [identical for both sets of maps] indicate locations of high DOS intensity for states $E_{1,n}$ (1-9) and E_2 (10-15). Location

16 marks a region with a localized higher energy state [~1.9 V, map not shown], likely corresponding to a smaller NC (with a different crystallographic orientation) that is in the process of merging with NC_1. 24

3.1 STM topographies of ligand-covered (a)-(c) and ligand-free (d)-(f) PbS NCs. Figures (g)-(i) highlight topographical features observed in (d)-(f). The crystallographic directions and NC boundaries are identified with the aid of STS DOS mapping. All STM topographies measured with setpoint 2.0 V bias, 1-2 pA tunneling current. 35

3.2 (a) DOS spectra for six representative PbS NCs (individual spectra shifted for clarity). Occupied (unoccupied) states denoted by Hn (En) respectively. All dI/dV curves measured with set-point 1.6-2.6 V bias, 15-30 pA tunneling current. Histogram (bottom) of energetic locations and distributions for discernible states E1,1, E2, and H1 for 13 NCs, bin size 0.2 eV (b) Bandgaps vs. height for measured NCs overlaid on data for two limiting cases: spherical NCs and 2D PbS quantum wells. Open symbols correspond to the E1,1 - H1 energy differences, whereas closed symbols correspond to values obtained from PIAB orbitals differences of many measured DOS spectra in Figure 2a are considerably lower than those (as determined from DOS mapping). The curve for spherical PbS NCs, and gray shaded region corresponding to 2D PbS quantum wells, were obtained from Moreels et al.[65] and Lee et al.,[66] respectively. 37

3.3 (a) STM topographic image of a PbS NC. (b) DOS "cross-section" mapping along the path of the dotted line in (a). (c) Individual DOS spectra measured at locations marked in (a). STS measurements in (b) and (c) were taken with a set-point of 1.9 V bias and 30 pA tunneling current. Variations in the energies of electronic states across the NC roughly follow the NC topography, which is a result of the locations-specific variation of the bias voltage drop inside the NC.[56] 41

3.4 STM topographic image of NC1. (b) DOS mapping of NC1 along the path of the dotted line in (a). (c) Individual DOS spectra for locations marked in (a). STS measurements in (b) and (c) were taken with set-point 1.6 V, 30 pA tunneling current. 41

3.5 2D DOS maps of unoccupied (a-c) and occupied (d, e) states for NC1. DOS state representations show (from left to right) combination topography/DOS map overlay (yellow outline indicates area of DOS mapping), DOS map only, and DOS map with black lines showing DOS features that are in registry with NC1 crystallographic features from Figure 1g. Parameter α is distance between two neighboring {211} planes, as shown in the model in Figures 6a and b. STS measurements taken with set-point 1.6 V bias, 30 pA tunneling current. STM topography image measured with set-point 2.0 V bias, 2 pA tunneling current. .. 44

3.6 Model representations of relevant PbS fcc crystallographic facets with idealized reconstruction features. (a, c) (111)-plane views showing rows of Pb adatoms oriented along <110> and <211> directions respectively, with indicated inter-atomic-row distances in integer multiples of distances α and β respectively. (b, d) (110)-, and (211)-plane side-views of the same features as in (a) and (c) showing vertical atomic steps responsible for appearance of varied distances between the bright DOS "stripes" in Figure 5 and Figure 8. 46

3.7 DOS spectra for NC2 measured at locations P1-3 shown in the inset STM topography. Sections of spectra P1 and P2 containing relevant states have been magnified by designated amount for clarity. STS measurements were taken with set-points of 1.5-2.2 V bias, 10-20 pA tunnelling current. STM topography image measured with set-point 2.0 V bias, 1 pA tunnelling current. 49

3.8 Same as Figure 5 for NC2. Parameters α and β are the distances between two neighboring {211} and {110} planes respectively, as shown in the model in Figures 6. STM topography image measured with set-point 2.0 V bias, 1 pA tunneling current. STS maps measured with set-point 1.5 V bias, 20 pA tunneling current. 51

4.1 Enhanced STM topography of PbS NC with crystallographic features in registry with (111) facet, including features with 120° angles (a). Single point STS showing progression of sub-bandgap states $E_{1,n}$ (b) for points P1 and P2 in (c). Enhanced topography and real space correspondence (c) with single point STS spectra seen in (b) and 2D dI/dV intensity map from (d). Single energy 2D dI/dV intensity map of sub-bandgap state $E_{1,1}$ of PbS NC showing the commensurability of dI/dV intensity features with NC (111) facet topographic features in (a) 58

4.2 Idealized model of a PbS 2x1 reconstructed (111)Pb surface (a), with real space crystallographic directions (black dashed arrows) and corresponding reciprocal space wave-vector directions (red arrows and 1st BZ special point labels). Pb atoms are gray circles with cyan outlines, S atoms are yellow circles with dashed black outlines, Pb surface vacancies transparent with cyan outlines. Subfigure (b) shows a top-down view – (111) facet – of the real space displacement (in x, and y) between unrelaxed and relaxed atomic positions of Idealized model of a PbS 2x1 reconstructed (111)Pb surface seen in (a). Sub-figure (c) is the side view – (101) facet – for the model slab described above, highlighting displacements of slab atoms along the direction normal to the surface facet. 62

4.3 Representation of, and reciprocal (k) space relationships between, 3D- and surface 2D-Primitive cell Brillouin Zones (PBZ) and the Super cell Brillouin Zone (SBZ) for the 2 x 1 (111)Pb reconstructed FCC PbS supercell. FCC structure 3D, surface 2D PBZ, and surface SBZ represented in solid black, purple hashmark, and solid cyan lines respectively. Reciprocal space special

points labeled for both 3D (L, X special points marked by red, and dark blue circles respectively) and surface 2D (letters with over-bars) representations. The corresponding symmetry point correspondences between different BZ representations indicated with vertical colored (L_a symmetry in pink, L_b symmetry in dark blue, and L_c symmetry in green) hash-marked lines. Corresponding real space crystal directions added for reference. 70

4.4 Figure 4.4a and 4.4b present dispersion band diagrams for the un-relaxed and relaxed 2 x 1 (111)Pb reconstructed SC, respectively. Red-black-blue colored bands indicate a high-normal-low atomic orbital character contribution for each 2D surface SBZ band for surface Pb atomic orbitals of the SC. Wave-vectors corresponding to special points of the Surface SBZ are indicated with horizontal dashed lines and correspond to wave-vectors along the path of the red box in Figure 4.3. 73

4.5 Figure 4.5a and 4.5b present dispersion band diagrams for the un-relaxed and relaxed 2 x 1 (111)Pb reconstructed SC, respectively. Red-black-blue colored bands indicate a high-normal-low atomic orbital character contribution for each 2D surface SBZ band for core Pb atomic orbitals of the SC. Wave-vectors corresponding to special points of the Surface SBZ are indicated with horizontal dashed lines and correspond to wave-vectors along the path of the red box in Figure 4.3. 74

4.6 Figure 4.6a and 4.6b present dispersion band diagrams for the un-relaxed and relaxed 2 x 1 (111)Pb reconstructed SC, respectively. Red-black-blue colored bands indicate a high-normal-low atomic orbital character contribution for each 2D surface SBZ band for subsurface S atomic orbitals of the SC. Wave-vectors corresponding to special points of the Surface SBZ are indicated with horizontal dashed lines and correspond to wave-vectors along the path of the red box in Figure 4.3. 75

4.7 Figure 4.7a and 4.7b present dispersion band diagrams for the un-relaxed and relaxed 2 x 1 (111)Pb reconstructed SC, respectively. Red-black-blue colored bands indicate a high-normal-low atomic orbital character contribution for each 2D surface SBZ band for core S atomic orbitals of the SC. Wave-vectors corresponding to special points of the Surface SBZ are indicated with horizontal dashed lines and correspond to wave-vectors along the path of the red box in Figure 4.3. 76

4.8 Histograms for the gamma point Pb d-state eigenvalues of the un-relaxed (top), relaxed (bottom) 2 x 1 (111)Pb reconstructed PbS SC. Surface(core) Pb d-state eigenvalues are highlighted in red(blue). 79

4.9 Projected Density of States (PDOS) vs. Total Density of States (TDOS) for specified atoms of the 2 x 1 (111)Pb reconstructed SC. Inset PDOS and TDOS

curves centered on the band-gap region, for specified atoms, increased by a factor of ten for clarity. 84

4.10 Electron density cross-sections of the $\overline{\Gamma}/\overline{M}$ ($\Gamma/L_a/L_b$) point along $[0\bar{1}0]$ facets (red/green planes - top/bottom Pb rows inset crystal image at right) for the 2 x 1 (111)Pb reconstructed SC slab before relaxation. Corresponding S (yellow) and Pb (gray) atoms in their unrelaxed lattice positions shown for clarity. Electron density denoted by inset color gradient, with red(blue) indicating high(low) electron density. 87

4.11 Electron density cross-sections of the $\overline{\Gamma}/\overline{M}$ ($\Gamma/L_a/L_b$) point along $[0\bar{1}0]$ facets (red/green planes - top/bottom Pb rows inset crystal image at right) for the 2 x 1 (111)Pb reconstructed SC slab after relaxation. Corresponding S (yellow) and Pb (gray) atoms in their relaxed lattice positions are shown for clarity. Electron density denoted by inset color gradient, with red(blue) indicating high(low) electron density. 88

4.12 Electron density cross-sections of the $\bar{}$M' (Lc) point along $[01\bar{}0]$ facets (red/green planes - top/bottom Pb rows inset crystal image at right) for the 2 x 1 (111)Pb reconstructed SC slab before relaxation. Corresponding S (yellow) and Pb (gray) atoms in their unrelaxed lattice positions shown for clarity. Electron density denoted by inset color gradient, with red(blue) indicating high(low) electron density. 89

4.13 Electron density cross-sections of the $\bar{}$M' (Lc) point along $[01\bar{}0]$ facets (red/green planes - top/bottom Pb rows inset crystal image at right) for the 2 x 1 (111)Pb reconstructed SC slab after relaxation. Corresponding S (yellow) and Pb (gray) atoms in their relaxed lattice positions shown for clarity. Electron density denoted by inset color gradient, with red(blue) indicating high(low) electron density. 90

4.14 Electron density cross-sections of the $\overline{\Gamma}/\overline{M}$ ($\Gamma/L_a/L_b$) point along $[10\bar{1}]$ facets (red plane inset crystal image at right) for the 2 x 1 (111)Pb reconstructed SC slab before relaxation. Corresponding S (yellow) and Pb (gray) atoms in their unrelaxed lattice positions are shown for clarity. Electron density denoted by inset color gradient, with red(blue) indicating high(low) electron density. 91

4.15 Electron density cross-sections of the $\overline{\Gamma}/\overline{M}$ ($\Gamma/L_a/L_b$) point along $[10\bar{1}]$ facets (red plane inset crystal image at right) for the 2 x 1 (111)Pb reconstructed SC slab after relaxation. Corresponding S (yellow) and Pb (gray) atoms in their relaxed lattice positions are shown for clarity. Electron density denoted by inset color gradient, with red(blue) indicating high(low) electron density. 92

4.16 Electron density cross-sections of the $\overline{M}'$ (L_c) point along $[01\bar{1}]$ facets (blue plane inset crystal image at right) for the 2 x 1 (111)Pb reconstructed SC slab after relaxation. Corresponding S (yellow) and Pb (gray) atoms in their relaxed

lattice positions are shown for clarity. Electron density denoted by inset color gradient, with red(blue) indicating high(low) electron density. 93

4.17 Effective Band Structure (EBS) for the individual L_n segments (where n = a, b, c) of the 2 x 1 (111)Pb reconstructed SC slab produced by sampling reciprocal lattice vectors in the [111] direction and using the band unfolding procedure described previously. Colored arrows, representing direction, and special point labels correspond to those seen in the 3D PBZ representation at right (4.16b). The spectral weight, as described in the unfolding methodology, is visualized through a normalized (over all bands of the specified PBZ direction L_n) gray scale gradient scheme and represents the probability of one or more PC eigenstate's contribution to a particular SC state.[11] In essence, the greater the spectral weight intensity (darker gray-black) for wave vectors of the SC EBS, the greater the number of contributing PC eigenstates, and the more bulk-like, or more "physical", the corresponding SC wave-vector. Corresponding calculated bulk PbS bands (red dotted lines) are overlaid for comparison. 102

A.1 STM topographic images showing crystallographic features for three PbS NCs. (a), (b), (c) Topographies for three representative NCs. (d), (e), (f) NC topographies, [same as in (a), (b), and (c) respectively] with lines and relative angles indicating orientations of crystallographic features for each NC. The observed angles suggest that the top NC facets corresponds to crystal planes (111), (100), and (100) respectively. (g), (h), (i) Enhanced topographic images [for the same NCs] with same crystallographic markings as in (d), (e) and (f)..... 112

A.2 Voltage drop in a biased STM junction with a NC under the STM tip. 113

A.3 Plot of the energy difference between the E_2 and $E_{1,1}$ states vs. the energy difference between the $E_{1,1}$ and H_1 states for 10 measured NCs. During this experiment, many of the measured NCs did not exhibit clearly-defined H_1 or E_2 states, and thus were not included here. 114

A.4 Absorbance and PL spectra of PbS NCs following thiol-ligand exchange. The emission peak at 977 nm (1.27 eV) corresponds to an approximate diameter of 3.2 nm PbS NC. 116

B.1 Shows the prominent unoccupied states for NC1. Subfigures (a-f) include (from left to right) a combination of topography(grayscale), and DOS map(color) overlay (where the yellow outline encloses the area of DOS mapping), DOS map only, and DOS map with black lines showing DOS features that are in registry with NC1 crystallographic features from Figure 1g in the main text. Parameter α is defined as the distance between two neighboring {211} planes, as shown in the model in Figures 6a and b in the main text. STS measurements taken with set-point 1.6 V bias, 30 pA tunneling current. STM topography image measured with set-point 2.0 V bias, 2 pA tunneling current. 118

B.2 Shows the prominent occupied states for NC1. Same area and representation as Figure S1 for the occupied states of NC1. Parameter β is defined as the distance between two neighboring {110} planes, as shown in the model in Figures 6c and d in the main text. Set-points of STM topography image and STS maps same as in Figure B.1 119

B.3 Shows the prominent unoccupied states of NC2. Same representation as in Figure S1 for NC1. Parameter β is defined as before for figure S2, and as shown in the model in Figures 6c and d in the main text. STM topography measured with set-point 2.0 V bias, 1 pA tunneling current. STS maps measured with set-point 1.5 V bias, 20 pA tunneling current. 120

B.4 Shows the prominent occupied states of NC2. Same representation as in Figure S3 for NC2. Parameter α is defined as the distance between two neighboring {211} planes, as shown in the model in Figures 6a and b in the main text. Set-points of STM topography image and STS maps same as in Figure B.3 121

B.5 Shows examples of PbS NCs displaying localized defect-related states in their DOS. Unoccupied $E_{1,n}$ and occupied H_1 states show marked intensity differences depending on location, and are associated with the reconstruction of polar PbS (111) surfaces or regions of marked non-stoichiometry in which excess S (Pb) atoms at the surface lead to sub-bandgap states broken off from the valence(conduction) bands. These observations are in keeping with and further support conclusions made with regard to the sub-bandgap states observed for NCs discussed in the main journal article. 122

B.6 DOS maps for $H_{1,n}$ and $E_{1,n}$ states of NC2 showing anti-correlation in their spatial distributions. White circles (black x's) mark locations of local high intensity for states $E_{1,n}$ ($H_{1,n}$). 123

LIST OF TABLES

Table Page

4.1 Löwdin Charge Analysis for Un-relaxed 2 x 1 (111)Pb SC Slab 67

4.2 Löwdin Charge Analysis for Relaxed 2 x 1 (111)Pb SC Slab 68

CHAPTER I
INTRODUCTION

1.1 Very Small Things Can Have a Big Effect

Lead-chalcogenide (PbX, where X=S, Se) semiconducting nanocrystals (NC), and optoelectronic devices incorporating thin-films constructed from them, are an active area of research[1-6] due to their superlative optoelectronic properties, and highly controllable solution processability.[7-9] These materials are particularly appealing for use in the next generation of solar-energy converters because of the tunability of their optical properties,[10-12] efficient multiple exciton generation[13-18], and potential for extraction of unrelaxed hot carriers[19]. Indeed, the power conversion efficiency of photovoltaic devices constructed from PbX NC thin films has increased rapidly over the course of a decade, with solar cell device architectures employing ever improving NC surface passivation techniques resulting in increasing external quantum efficiencies from 8% to 13% during that time[1, 2, 5, 6]. This steady increase in device performance has been, in part, the result of an improved understanding of the role played by the PbX NC's surface atomic structure, and its effects on the surface electronic environment (i.e. surface trap states), in determining the optoelectronic properties of these nano-materials. Indeed, identification and understanding of the origin of surface trap states in semiconducting NCs is of singular importance to this nascent area of research in order to improve the optoelectronic performance of NCs and bring them on par with established semiconducting technologies.

Numerous different experimental tools have been employed to determine the origin of sub-bandgap and surface tap states in PbX NCs including various X-ray spectroscopy techniques, Ultraviolet photoelectron spectroscopy, UV-Vis-NIR absorbance

spectroscopy, transient absorption spectroscopy, and photoluminescence spectroscopy.[20] However, all of these techniques offer only ensemble level information regarding NC sub-bandgap trap states, and provide little information on surface atomic structure, if at all. To augment these experimental findings, important theoretical work has been done to understand the mechanisms, and underlying physical and chemical surface structures, of sub-bandgap states in PbX NCs.[21-23] As a result of these findings considerable research has been devoted to various techniques for the passivation of surface trap states in PbX NCs, resulting from NC surface structural imperfections and capping ligand interactions.[20, 24] Though improvements in the understanding and control of surface states in semiconducting NCs have undoubtedly been made, it is clear that more work in this area needs to be done.

To provide further insights into the specific surface structures, and chemical compositions that give rise to sub-bandgap and trap states in individual semiconducting NCs the Nazin group has recently undertaken several studies of both PbS and Si NCs utilizing the powerful, sub-nanometer scale experimental tool of Scanning Tunneling Microscopy/Spectroscopy (STM/S).[25-28] STM/S affords a suite of interrogative techniques that provides a unique opportunity to probe surface structure, atomic composition, and electronic properties of NCs, all at the same time, and to combine this information to produce a real-space description of NC electronic states. These STM/S explorations of PbS and Si NCs have provided a wealth of information on the correlation between surface structures, atomic composition, and the electronic states that arise from them, and led to a deeper understanding of the fundamental relationship between surface states, specifically band edge and sub-bandgap states, and their relationship to the local NC surface environment.

1.2 Semiconducting Nanocrystal Quantum Dots

Semiconducting NCs are meta-stable inorganic structures ten-thousandth the size of a human hair with diameters less than 20 nm, and containing between several hundreds to thousands of atoms depending on chemical composition; semiconducting NCs lie in a size regime between atoms and bulk materials.[29-32] Resembling the composition of their parent material, they maintain the periodic crystal structure of the bulk and in so doing its semiconducting nature. Yet due to the nanoscale size of semiconducting NCs, which are smaller than or comparable to the spatial extent of their excitons, the motions of electrons and holes are constrained within the spatial extent of the semiconducting NCs, leading to the quantum confinement of charge carriers, which has a direct effect on the optoelectronic properties of these systems.[31] Where the parent bulk material exhibits continuous valence and conduction bands, NCs exhibit a discrete electronic structure, or density of states (DOS), arising from this confinement effect leading to molecule-like optoelectronic behavior. As a result of the quantum confinement effect in NC systems the band gap of the parent bulk material is seen to blue-shift as NC dimension decreases, consequently semiconducting NCs are able to efficiently absorb and emit light over a specific tunable frequency range.[31]

The focus of the following research is on PbS semiconducting NCs, which are a IV–VI compound semiconductor with face centered cubic (fcc) rock salt crystal structure. PbS has a four-fold degenerate direct bandgap, centered on the L-points of the fcc Brillouin zone, with a bulk bandgap of ~ 0.41 eV.[33] The effective masses of PbS holes (m_h^*) and electrons (m_e^*) is ~ 0.1m (m representing the free electron mass), with a mean exciton Bohr radius of electron-hole pairs of ~ 18 nm due to the coulomb binding energy of this system. As a result, PbS size dependent optoelectronic properties emerge when PbS NC diameters are

~9 nm or smaller as a result of strong exciton confinement.[31] Due to the relatively large PbS NC diameter at which exciton confinement begins enables tuning of the PbS bandgap over a wide range, between 0.6 and 1.6 eV, by means of NC size reduction equating to a spectral range from between 200 nm to 2,400 nm, providing optical absorption from the near-infrared (NIR) through visible to UV.[34] The large potential absorption/emission spectral range, over frequencies of significant interest to research and industry, along with relatively high molar absorption coefficients (~ 10^6 M^{-1} cm^{-1} at 400 nm),[35] has spurred great interest in PbS NCs for use in a wide variety of applications, but especially photovoltaic devices.[36]

Synthesis techniques for PbX NC have been widely studied over the past two decades, resulting in a variety of high-quality synthesis methods, with a consistently achievable size dispersity of less than 5%,[2, 34, 37, 38] and with well-defined (111) and (100) facets.[39] Due to their nanometer size scale, the large surface to volume ratio of semiconducting NCs is known to significantly impact their electronic structure, since the ratio of the number of surface atoms to the total number of atoms of the NC is large.[16, 31] Thus, NC surface ligand functionalization has been a topic of significant importance as they are required in the initial NC synthesis and growth processes, and later in the passivation of dangling bonds, resulting in trap states, of surface atoms.[14, 31] Due to their large band gaps, lengths in excess of 1.5 nm, and insulating nature; organic ligands hinder conduction and electron transport leading to poor charge carrier conductivity in NC superlattice arrays and with electrical contacts.[3, 40] In addition, organic ligands used in PbX NC syntheses often inadequately passivate the NC surface, allowing surface trap states to proliferate.[20] As a result, passivating ligand research for PbX NCs has been focused on improvements in NC

synthesis techniques,[7, 8] on smaller and shorter ligands including atomic ions,[14] with emphases on the passivation of surface trap states, energy level alignment with electrical contacts,[41] and overall improved NC performance.[24]

1.3 Basic Theory of Quantum Tunneling and Scanning Tunneling Microscopy/Spectroscopy

Scanning tunneling microscopy/spectroscopy (STM/S) are a set of related, atomic scale, electronic measurement techniques which rely on the concept of quantum mechanical tunneling as their basis of operation.[42, 43] Through STM/S we are able to interrogate the physical and chemical structures, as well as electronic properties, of individual molecules and nanoparticles. By coupling this complementary information of form and function, we are able to gain unparalleled access into material properties at the atomic scale.

What is quantum mechanical tunneling? In the classical mechanical understanding of a particle, with energy *E*, and confined in a potential well with potential barriers on either side of potential $U(z)$ (i.e. particle in a box), the probability of the particle crossing into the potential barrier region, when $E < U(z)$, is zero. In essence, the particle is unable to exist in, or even to penetrate, the potential barrier region. An often-used analogy is of a ball bouncing around inside a room with high walls and no doors; assuming the ball is not bouncing high enough to pass over the walls, the ball cannot pass through the walls and is therefore confined to remain inside the room. Thus, the particle cannot travel through the potential barrier and is confined to the potential well. However, quantum mechanical tunneling is the theory which describes an electron (or other particle governed by quantum

mechanics) in a potential well (i.e. atomic state) having the non-zero probability of penetrating a potential barrier separating its parent atom from an adjoining atom, and burrowing into an atomic state of the adjoining atom, by virtue of its wave-like properties. The probability of an electron tunneling into a state of an adjoining atom, through the intervening potential barrier, results from the fulfillment of the Schrodinger equation by an appropriate wave function description $\psi(z)$ (electron motion) of the electron. See Chen,[42] or Griffiths,[43] among others, for a full mathematical treatment of quantum tunneling.

By utilizing the quantum mechanical property of the electron, and due to the fact that electrons are charge carriers, by applying a bias voltage (i.e. electric field) across the potential barrier region, a flow of electrons can be induced to tunnel between atoms separated by the vacuum barrier region. In STM, the basic experimental setup consists of a conducting substrate (usually metal, or graphite), on which samples are prepared (e.g. sub-monolayers of molecules or nanoparticles), opposite an atomically sharp metal tip, usually tungsten, platinum iridium alloy, or silver.[42] Thus, by bringing the atomically sharp metal tip in close proximity (< 1 nm) to a sample surface, containing molecules or nanocrystals of interest, and by applying a bias voltage between the tip and the sample surface, electrons can be induced to tunnel between the tip and the sample through the intervening vacuum barrier (potential barrier) producing a tunneling current.

Bardeen's theory of tunneling,[44] Giaever's tunneling junction experiments with metal-insulator-metal junctions,[45] and the Tersoff-Haman model of tunneling for the scanning tunneling microscope (STM),[46, 47] among many others, have provided the foundation for the use and interpretation of quantum mechanical tunneling measurements as applied by scanning tunneling microscopy/spectroscopy (STM/S). Bardeen showed that the tunneling

current *I* between two electrodes, in this case a conducting tip and a conducting sample substrate, is proportional to the density of states (DOS) of both the tip and the sample.[44] Thus, measurement of the tunneling current (*I*) with respect to the voltage applied (i.e. bias voltage *V*), can be used to produce an *I/V* curve, which can be plotted and information inferred regarding the electronic states of the sample. Given certain assumptions and constraints, the most important of which regard the shape of the tip in the tunneling junction and the specific wavefunction of the tunneling electrons,[46, 47] the change in the tunneling current (*dI*), with respect to a change in tunneling junction bias voltage (*dV*), produces a curve of the differential conductance (*dI/dV*), which gives information regarding the local density of states (LDOS) of the sample, provided the LDOS of the tip is flat over the energy range measured.[42] Thus, by careful preparation of the tip and sample surface, and through the use of the measurement technique known as STS, as described above, for a discrete location on a sample surface, electronic states of semiconducting molecules and nano-particles on a conducting substrate can be measured and important information inferred about their primary bandgap, especially regarding sub-bandgap, trap, or surface states.

1.4 Scanning Tunneling Microscopy/Spectroscopy in Practice

In our investigations of semiconducting molecules and nanoparticles, the Nazin group uses the unique and unparalleled measurement techniques afforded by our research groups home-built Scanning Tunneling Microscope (STM).[48] The Nazin group's STM provides the means by which the electronic properties of individual semiconducting molecules and nanoparticles can be interrogated, at cryogenic temperatures, and with atomic scale precision. By utilizing the scanning tunneling spectroscopy (STS) functionality of our

STM, in conjunction with the STM topographic measurement capability, the spatially resolved local density of states (LDOS) for individual molecules and nanoparticles can be observed. From the information gathered during these investigations, we can correlate the spatially resolved electronic LDOS for molecules and nanoparticles with the molecular geometries and physical surface structures of these materials on the atomic scale. (final sentence connecting these measurements with goals above?)

The Nazin group STM features a rigid pan-style,[49] utilizing a tube-style fine scanning piezo,[50] produced in cooperation with RHK Technology,[48] which operates in ultra-high vacuum, ~ 5.0 x 10^{-11} Torr, equivalent to the vacuum of inter-planetary space. It is the first STM design known to integrate a closed-cycle cryostat for continuous sample cooling, utilizing a dual stage helium cryostat based on the Gifford-McMahon refrigeration cycle,[51] allowing for extended STM/S studies at temperatures < 20 K, for up to several months, without significant loss of helium refrigerant. The CCC is connected to the STM via a cold-finger and cold volume, which is thermally connected to the STM, but vibrationally isolated, in order to provide the necessary cooling while preventing mechanical noise from the cryostat from interfering with the vibrational isolation of the STM scanner-head. A temperature stability of ±1 milli-kelvin can be maintained for weeks through the use of a proportional-integral-derivative (PID) temperature controller, allowing for a minimum of thermal drift. The rigidness of the pan-style scanner head, in conjunction with the vibrational isolation, cryogenic capability, and thermal stability, have enabled a measurable STM tip lateral drift rate over a sample surface of 1.8 $\frac{\text{Å}}{hr}$, which is critical for atomic scale measurements.

As described in the previous section, STM utilizes the quantum tunneling effect and the

application of a bias voltage to produce a measurable current between a conductive tip,[42] silver in this case,[52, 53] and sample surface. During the initial course approach phase, the tip is brought into electrical contact with the sample surface along the z-axis by using a course approach piezo motor while applying a bias voltage of several volts, depending on sample material, and measuring for a tunneling current of several hundred nanoamps, known as the course approach "set-point". Once electrical contact is established between the tip and the sample at the course approach "set-point", via quantum mechanical tunneling, a fine approach piezo (scanning piezo) is used during actual STM measurements for atomic scale positioning.[42] When the tip is in electrical contact with the surface a scanning "set-point" (bias voltage/tunneling current) is chosen based on the bandgap of the material to be probed, and the stability of the tip on the surface. In our experiments, the scanning "set-point" ranged from a bias of anywhere between millivolts to several volts, and tens to hundreds of nanoamps tunneling current, depending on the sample's electronic properties such as the primary bandgap, the surface environment, and tip stability. The height of the tip over the sample surface (z-axis) is maintained via feedback loop, where a drop in measured tunneling current, for a given scanning "set-point", would cause the scanning piezo to drive the tip forward (z-axis) towards the sample surface, and an increase in measured tunneling current would have the opposite effect. Thus, the conducting metal tip will maintain a constant height, dependent on the "set-point", and electronic properties of the tip and the sample, over a given point of the sample surface. Fine tip motion along x-y axes are controlled by the scanning piezo as well, and drive the tip in x and y directions providing for a raster motion of the tip over the sample surface, allowing discrete areas of the sample surface to be probed with nanoscale precision.

The Nazin group scanning tunneling microscope, and indeed all modern STMs, incorporate two basic modes of operation for data collection independently referred to as *Constant Current* (topography) and *Constant Height* (differential conductance – *dI/dV*) modes.[42, 54] *Constant Current* mode utilizes the functionality of the scanning piezo motor in conjunction with the feedback loop to maintain the "set-point" current, for a given bias, as the tip is caused to move across the sample surface in x and y directions, in a raster motion. The combined motions of the scanning piezo motor along the x, y, and z axes has the effect of building up an atomic scale topographical map of a given area on the sample surface. In this mode features a fraction of a nanometer, such as sample surface step edges, and, in the case of Au (111) surfaces, surface reconstruction,[55] can be observed and used for alignment and scaling at cryogenic temperatures. Additionally, adsorbed molecules and nanoparticles are detected based on observations of apparent height changes, lateral size, shape, orientation and geometry, and in the case of nanocrystals, material dependent crystallographic information.

Constant Height or Differential Conductance (*dI/dV*) mode, is used to measure the local density of states (LDOS) of a sample, based on tunneling conductance measurements for a single location on the sample surface. Differential conductance (*dI/dV*) measurements are conducted with the tip height "frozen" over the sample by inhibiting the feedback loop from changing the tip-sample distance with changes in tunneling current, and a ramp of the bias voltage is performed over a specified voltage range, with a defined voltage increment. Given that the tip-sample distance does not change, as the ramp of the bias voltage is performed, and depending on the electronic properties of the material being measured, the measured tunneling current will change as a function of applied voltage. This change in

current, as a function of change in voltage, is a measure of the differential conductance (*dI/dV*) of the sample, and is equivalent to the LDOS of the material,[42] assuming the tip is "ohmic", meaning that the LDOS of the tip is "flat" or un-changing over the applied bias range. In our STS measurements of semiconducting organic molecules and nanoparticles, the Nazin group STM uses the Lock-in technique to produce a differential conductance (*dI/dV*) curve.[42] Using many such LDOS measurements (curves) over a regularly spaced spatial grid spanning a few to tens of nanometers of the sample surface, the Nazin group has been able to produce spatially resolved DOS maps of the primary bandgap region for semiconducting organic molecules and nanoparticles.[25-28, 56, 57]

1.5 Dissertation Summary

Utilizing the above described surface measurement capabilities and techniques of the Nazin STM, the following research seeks to further our understanding of the surface electronic environment of PbS NCs resulting from surface structure and reconstruction, which is a key determinant of the optoelectronic properties of this system. To accomplish this goal, myself, in collaboration with other research members of the Nazin group, conducted STM/S experiments of PbS nanocrystals. Chapter II is based our publication,[25] co-authored by Dmitry A. Kislitsyn, Christian F. Gervasi, Thomas Allen, Peter K. B. Palomaki, Jason D. Hackley, Ryuichiro Maruyama, and Gorge V. Nazin. In this study of the surface electronic environment of naked PbS nanocrystals on an Au(111) substrate, where capping ligands were removed by gentle thermal annealing, surface-localized conduction band-edge states were observed. Through analysis of the topographic measurements of the individual PbS nanocrystals, crystallographic information observed

indicated that the (111) surface was found to predominate. Using the STM/S capabilities of the Nazin STM, the spatial-resolved orientation of the observed conduction band-edge states was correlated with crystallographic information for the individual PbS nanocrystal surfaces. Due to the fact that PbS nanocrystals are known to have Pb-rich surfaces,[34, 58] that Pb reconstructed PbSe nanocrystal surfaces have been observed,[22] and Pb atomic orbitals are the predominate contributors to PbS conduction band-edge states,[21] we attributed the observed highly localized conduction band-edge states to the electronic coupling of atomic orbitals for individual, undercoordinated, Pb atoms on the nanocrystal (111) surfaces.

In continuation of my work on the electronic properties of PbS nanocrystal surfaces, the research presented in the journal article described in Chapter III, co-authored by Christian F. Gervasi, Dmitry A. Kislitsyn, Thomas Allen, Jason D. Hackley, Ryuichiro Maruyama, and Gorge V. Nazin, seeks to further elucidate our understanding of the electronic states produced by different local nanocrystal surface environments and stoichiometries. STM measurements in this study suggest that PbS (111) facets predominate amongst the ligand free PbS nanocrystal surfaces observed, which, due to their polar nature, are known to reconstruct to lower their surface energy.[22] Furthermore, STS measurements of the PbS (111) facets observed in this study show a variety of localized sub-bandgap states at both conduction and valance band-edges, as well as the observation of Fermi-level crossing trap states. The conduction and valence band-edge states are attributed to alternately Pb-rich and S-rich local environments of the nanocrystal surface, while the Fermi-level crossing trap states are attributed to significantly off-stoichiometric local surface environments. Thus, the variability in electronic trap states observed for PbS (111) surfaces, depending on location, suggests that the local surface

conditions of PbS (111) facets are highly determinative of the surface electronic environment, and the optoelectronic properties of PbS nanocrystals.

To elucidate the STM/S experimental observations for specific sub-bandgap states observed in PbS nanocrystals described in chapters II and III myself, in collaboration with Hank I. Seeley and Gorge V. Nazin, undertook the as yet un-published theoretical and computational research described in Chapter IV. Using ab-initio density functional theory (DFT), our theoretical exploration described in this chapter focused on conduction band-edge states observed in our experimental STM/S studies of un-passivated PbS nanocrystals,[25, 26] which were attributed to surface Pb reconstruction of (111) crystal facets. Band diagrams produced from the ab-initio DFT calculations conducted on relaxed and un-relaxed 2 x 1 (111) Pb reconstructed surface model slabs indicate a splitting of the degeneracy of the four-fold degenerate L-points of the PbS fcc band structure for bands at specific symmetry preferred L-points over other L-points, which are the location of the primary bandgap responsible for the optoelectronic properties in PbS. In addition, atomic orbitals of the Pb atom surface reconstruction rows are shown to over-contribute to conduction band edge states, as compared to Pb atoms of the bulk. Indeed, cross-sections of electron density for the 2 x 1 (111) Pb reconstruct slab model indicated the formation of Tamm surface states localized on Pb atoms of the surface reconstruction rows, and associated with split off states at the conduction band-edge for bands at symmetry preferred L-points. The observed splitting, difference in dispersion character, and over-contribution of surface Pb atom atomic orbitals, along with associated Tamm surface states, for conduction band-edge states for L-point's of the PbS band structure are attributed to the effects of the overarching symmetry of the 2 x 1 (111) Pb surface reconstruction rows.

Thus, we attribute the reduction in apparent bandgap and appearance of conduction band-edge Tamm surface states in PbS nanocrystals to surface reconstruction of Pb-rich, under-passivated, (111) PbS facets.

CHAPTER II

SPATIAL MAPPING OF SUB-BANDGAP STATES INDUCED BY LOCAL NON-STOICHIOMETRY IN INDIVIDUAL LEAD-SULFIDE NANOCRYSTALS

This Chapter by Dmitry A. Kislitsyn, Christian F. Gervasi, Thomas Allen, Peter K.B. Palomaki, Jason D. Hackley, Ryuichiro Maruyama, and George V. Nazin was previously published under the same title in J. Phys. Chem. Lett. 5, 3701–3707 (2014).

2.1. Introduction

Recently, thin films composed of lead chalcogenide colloidal semiconducting nanocrystals (NCs) have emerged as a promising class of photovoltaic materials that allow great flexibility in controlling their properties by means of tailored synthesis, processing and film deposition.[1-2] Further, quantum confinement effects in NCs can be exploited to control their photoexcitation dynamics in order to achieve multiplication of photo-generated carriers[3-7] and/or hot-electron extraction,[8] which may enable solar cells with efficiencies in excess of the Shockley–Queisser limit.[9] While substantial progress has been made towards improving the efficiency of NC-based photovoltaic devices, with recent reports of efficiencies above 8%,[10-11] the microscopic picture of the fundamental physical processes of photo-generation and charge transport in NC films remains incomplete. One of the important outstanding questions is the impact of the NC surface chemistry on the

electronic properties of NCs. Imperfections in surface passivation or stoichiometry are thought to cause sub-bandgap states, which can have a significant impact on electron–hole recombination.[12] While evidence for such surface states was found in recent photoluminescence studies of as-synthesized lead chalcogenide NCs,[13-14] fabrication of functional photovoltaic devices may introduce further surface imperfections as it often involves a sequence of synthetic and processing steps including surface ligand exchange[15-16] and (in some studies) thermal annealing[17-18] that can both affect the nanocrystal surface chemistry. Indeed, sub-bandgap states have been identified in processed NC films using a variety of techniques, including photoluminescence;[14] a combination of current-based deep level transient spectroscopy, thermal admittance and Fourier transform photocurrent spectroscopies;[19] Scanning Tunneling Spectroscopy (STS);[20] and photocurrent measurements in NC-based field-effect transistor devices.[21] Despite the insights provided by such studies, they do not provide direct information about the local chemical and spatial structures of surface states. This information is critically important for addressing the remaining uncertainties regarding the nature of such surface states, especially given the diversity of atomic sites present on NC surfaces arising from variations in ligand coverage and the presence of different crystallographic facets.

2.2. Experimental Methods

Experiments were carried out in a home-built ultra-high vacuum (UHV) cryogenic STM system incorporating a STM scanner from RHK Technology. An Au(111)/mica substrate was prepared *in situ* by using multiple sputter/anneal cycles. Thiol-terminated PbS NCs (synthesis of PbS NCs is described in the Supporting Information) were deposited

on the Au(111) substrate in the load-lock section of the vacuum system using an in-vacuum solenoid pulse valve. The deposition parameters were chosen so as to obtain sub-monolayer NC coverage. The Au(111) substrate with deposited PbS NCs was then annealed overnight in ultra-high vacuum at progressively higher temperatures, with the final temperature of ~170°C. This annealing temperature was chosen to achieve removal of residual unstable species remaining after the initial annealing steps. Figure S1 shows representative STM images of several NCs on a Au(111) surface.

All imaging and spectroscopic measurements were carried out at a temperature of 15 K using electrochemically etched silver tips. All STS spectra were recorded using the lock-in technique at ~600 Hz, and bias modulations varying from 10 mV (individual spectra, and one-dimensional spatial scans) to 50 mV (two-dimensional DOS maps). PbS NCs deposited on Au(111) surfaces were annealed in ultra-high vacuum at 170 °C to remove surface ligands (see Experimental Details). Ligand-free NCs were targeted because they are unaffected by the uncertainties associated with different possible ligand shell configurations, and therefore serve as a useful model amenable to theoretical simulations. NCs in devices are also often stripped of ligands to increase inter-particle electronic coupling. In total, we studied 16 individual PbS NCs. The NCs were annealed at progressively higher temperatures until well-defined and reproducible NC topographies consistent with complete removal of ligands were obtained (Figure S1). The apparent heights of thus prepared NCs are typically 1-2 nm, while their lateral dimensions are 2-5 nm with width/height ratios being typically 2:1 to 3:1, which suggests that the NC shapes change significantly upon annealing. Importantly, annealed ligand-free NCs display topographic features, such as crystal facet steps and edges, showing visible angles

consistent with different crystallographic directions (Figure S1). STS spectra of individual NCs were obtained by measuring the differential tunneling conductance dI/dV as a function of the applied bias voltage (see Experimental Details).[22] The recorded dI/dV signal serves as a measure of the local density of states (DOS).

2.3. Experimental Findings

In this chapter I discuss the spatial mapping of sub-bandgap states in individual PbS NCs using a combination of Scanning Tunneling Microscopy (STM) and Scanning Tunneling Spectroscopy (STS). STS spectra of annealed NCs show progressions of occupied and unoccupied states separated by apparent band gaps of different magnitudes (Figure 2.1). All spectra in Figure 1 show similar progressions of states H_1 (highest occupied state), $E_{1,1}$ (lowest unoccupied state), $E_{1,2}$ and E_2 (both unoccupied states), with individual state energies varying for different NCs. A common feature of all spectra in Figure 1 is that states $E_{1,1}$ and $E_{1,2}$ are separated by ~0.2 V in all cases. Identifying the nature of states $E_{1,1}$ and $E_{1,2}$ is important because the lowest-lying unoccupied states are primarily responsible for the photophysical and electron transport properties of NC-based materials.[21] We note that overtones $E_{1,2}$ are unlikely to be caused by vibrational excitation of NCs[23] due to their relatively large energetic spacing, inconsistent with the vibrational energy scale of PbS.[24] This energetic spacing also appears too large to be explained by electronic splitting (caused by the NC anisotropy) of the different L-valleys in the Brillouin zone.[25] Similar spectral features observed in STS studies of electrochemically-grown PbS NCs were attributed to particle-in-a-box-like states.[26] According to this interpretation, state $E_{1,1}$ should correspond to the ground state, state E_2 should correspond to the excited

state varying along the Z-direction, and $E_{1,2}$ is attributable to excited states varying in the XY plane. Spatial mapping of NC DOS shows that the nature of $E_{1,n}$ states in the present case is more complex, as described below.

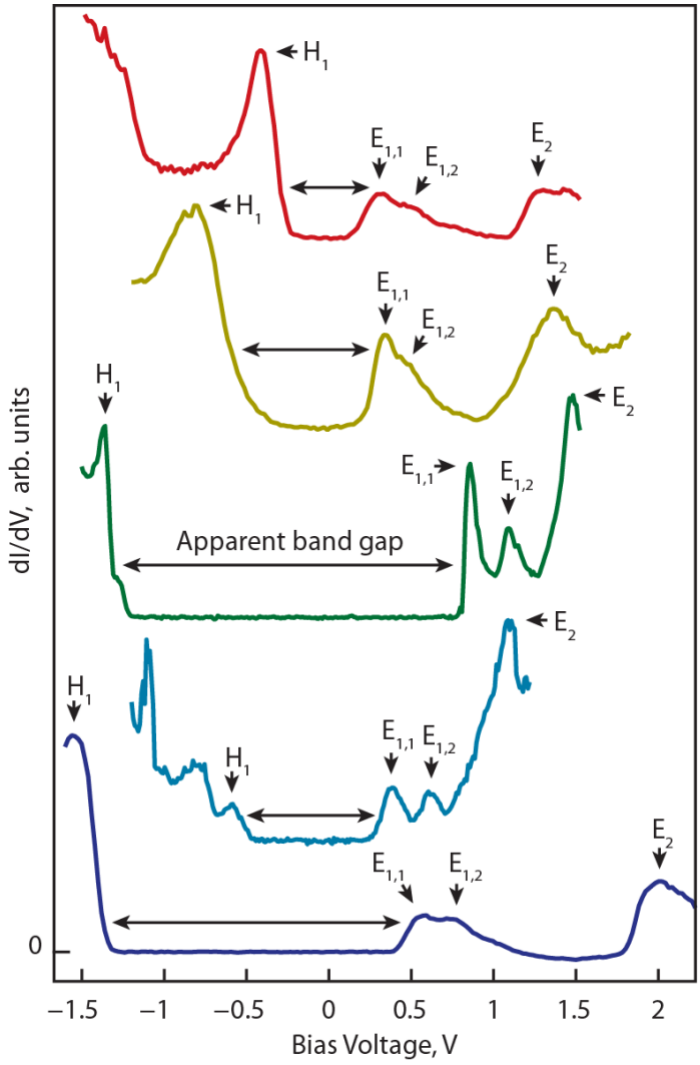

Figure 2.1. Representative dI/dV spectra for five PbS NCs (Set point voltages and currents range from 1.2 V to 2.5 V, and 10 pA to 30 pA for the spectra shown). The bias voltage effectively serves as the energy scale (see, however, discussion associated with Figure S2 for a more complete description of the relationship between the bias voltage and energy). Occupied and unoccupied states are indicated by arrows and marked with an 'H' and 'E' for holes and electrons respectively. The apparent band gaps for each of the NCs are marked with double sided arrows.

To understand the nature of the $E_{1,n}$ bands, we have carried out DOS mapping for several NCs. Representative data for one such NC (referred to as NC_1 in the following) are presented below. STM topography of NC_1 shows a series of steps angled at 120° degrees with respect to each other (Figure 2.2a,b). This observation suggests that these directions

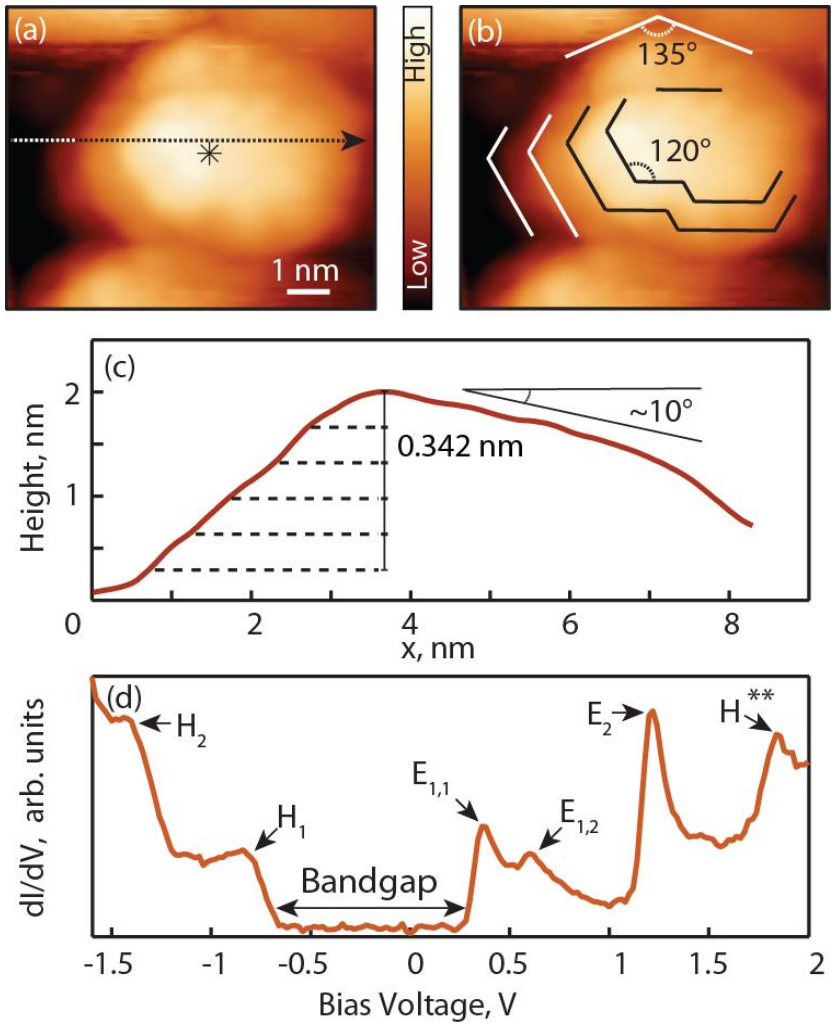

Figure 2.2. STM/STS characterization of a representative nanocrystal NC_1. (a) STM topography image of NC_1 [set point 1.0 V, 1.0 pA]. (b) Topographical features attributable to step edges oriented along specific crystallographic directions. The majority of features indicate 120° angles, which suggests that the top facet of NC_1 corresponds to a {111} plane. (c) A cross-section of the topography [path indicated by the arrow in (a)] showing that the top facet of NC_1 is at a small angle with respect to the Au(111) surface. Individual steps are marked with dashed lines, with the step height (0.342 nm) corresponding to the distance between the sulfur {111} planes. (d) A representative STS spectrum [set point 2.0 V, 15 pA] measured at the location marked by the star in (a). Prominent occupied and unoccupied states are marked with an 'H' and 'E' respectively.

correspond to the <110> crystallographic directions, while the top surface of NC_1 should correspond to the (111) crystallographic orientation, based on the stability of these facets established in TEM studies of restructuring of PbS NCs under similar temperatures in vacuum.[27-28] A cross-section of the topography for NC_1 (Figure 2.2c) shows that the top facet, oriented at ~10° with respect to the Au(111) surface, is relatively flat with corrugation at the angstrom-scale, consistent with complete removal of ligands.

A STS spectrum measured on top of NC_1 (Figure 2.2d) shows an electronic DOS with a ~0.8 eV bandgap formed by states $E_{1,1}$ and H_1. Additional states E_2 (1.3 eV) and H_2 (-1.4 eV) are found at higher voltages. The lowest unoccupied state $E_{1,1}$ shows a side-peak ($E_{1,2}$), which is observed in most annealed NCs (Figure 2.1). STS spectra measured at different locations on NC_1 show considerable variation in state energies and character. To visualize these variations, we recorded a spatial "cross-section" of the electronic DOS along a linear path across NC_1 (Figure 2.3a). The resulting DOS cross-section (Figure 2.3b) shows quasi-periodic oscillations in intensity for the electronic DOS of states $E_{1,n}$. The spatial variations of all states $E_{1,n}$ (Figure 2.3b) are nearly identical suggesting similar origins for the main peak and its sidebands. The spatial modulation of states $E_{1,n}$ occurs with an average period of ~0.9 nm, a large number as compared to the typical inter-atomic distances along the PbS(111) surface, which means that this modulation is not caused by the elemental contrast between Pb and S lattice sites that could be expected on a defect-free PbS surface.[29] In accordance with this assessment, the highest occupied state H_1, which is expected to be comprised of sulfur 3p atomic orbitals,[30] is not visibly modulated. The only identifiable variation of the H_1 state is a minor change in H_1 energy (from -0.8 V to -0.7 V and back to -0.8 V) as the scan progresses along the path in Figure 2.3a from P_1 to P_5. The trajectory

of the H_1 energy variation roughly follows the NC topography (high topographic locations correspond to the lower (in absolute value of applied voltage) onsets of resonant tunneling through H_1), which is explained by the variation of the voltage drop inside the NC.[33] A smaller variation in the tunneling onset energy is found for the unoccupied states, which is attributable to the different work-functions of the tip and sample, as explained further in the Supporting Information. Insight into the nature of states $E_{1,n}$ can be gained from a detailed analysis of their spatial behavior, as discussed in the following.

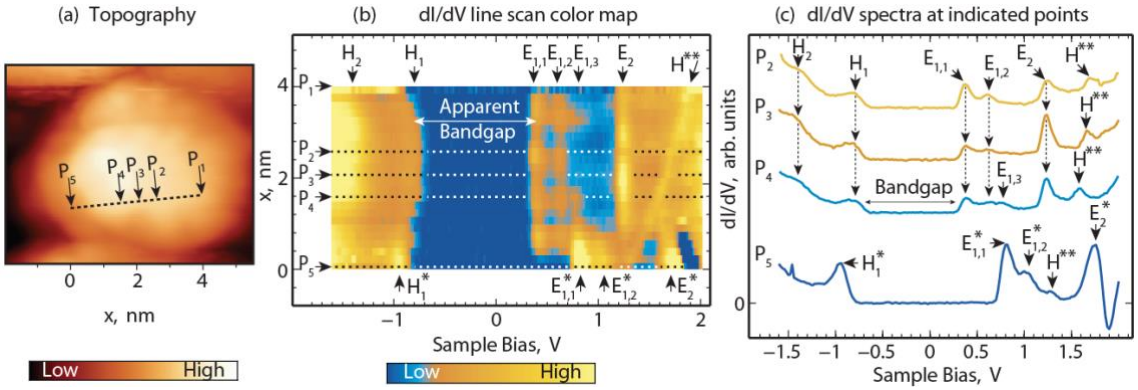

Figure 2.3. Spatial STS mapping across nanocrystal NC_1. (a) Topographic image [set point 1.0 V, 1 pA] showing the path of mapping (points P_1 through P_5). (b) Density of states [set point 2.0 V, 10 pA] as a function of bias voltage and position x along the path shown in (a). (c) Individual STS spectra from (b) measured at points P_2 through P_5. Occupied and unoccupied states are marked 'H' and 'E' respectively in both (b) and (c). Spectral feature H^{**} corresponds to "reverse" tunneling[31-32] through a localized occupied state outside of the mapping path.

To characterize the spatial behavior of the NC_1 electronic structure, we recorded STS spectra on a two-dimensional grid of (32 by 32) points covering the spatial range shown by the yellow rectangle in Figure 2.4a. In the overall bias voltage range sampled in these spectra, several spatial DOS patterns associated with distinct electronic states shown in Figure 2.3 are identified (Figure 2.4). These patterns show that the distributions of individual electronic states across NC_1 are highly inhomogeneous. States $E_{1,n}$ are primarily

concentrated in the left and bottom parts of NC_1 (locations 1-9 in Figure 2.4b, 0.35 V) in the vicinity of the steps observed in the STM topography (Figure 2.4a). The DOS intensity corresponding to these states forms stripe-like features running through locations 1-9 in Figure 2.4b. These four stripes correspond to the four DOS peaks observed along the x-coordinate for the $E_{1,1}$ states in Figure 2.3b. All states $E_{1,n}$ have very similar two-dimensional spatial distributions of their DOS, as can be seen in Figure 4b, consistent with the one-dimensional scan of Figure 2.3b. Figure 2.4b shows that the "stripes" are localized in the vicinity of the NC_1 step edges (highlighted in the bottom maps of Figure 2.4b). In contrast, unoccupied state E_2 is delocalized throughout NC_1, and is primarily concentrated in the upper right part of NC_1 (locations 10-15 in Figure 2.4b, 1.15 V) where no clear topographic steps exist.

Similar distinction between localized states at the onset of tunneling and delocalized states at higher voltages is found for occupied states: the highest energy state $H_1^{\dagger}$ appearing at -0.58 V (Figure 2.4c), is localized (analogously to states $E_{1,n}$) near the step edges, while states H_1 (-0.7 V) and H_2 (-1.4 V) show relatively uniform distributions. The latter are, in fact, even more homogenous than they appear: their apparent DOS in locations 13-15 is suppressed due to the effect of variable voltage drop across the NC described in the discussion of Figure 2.3b.

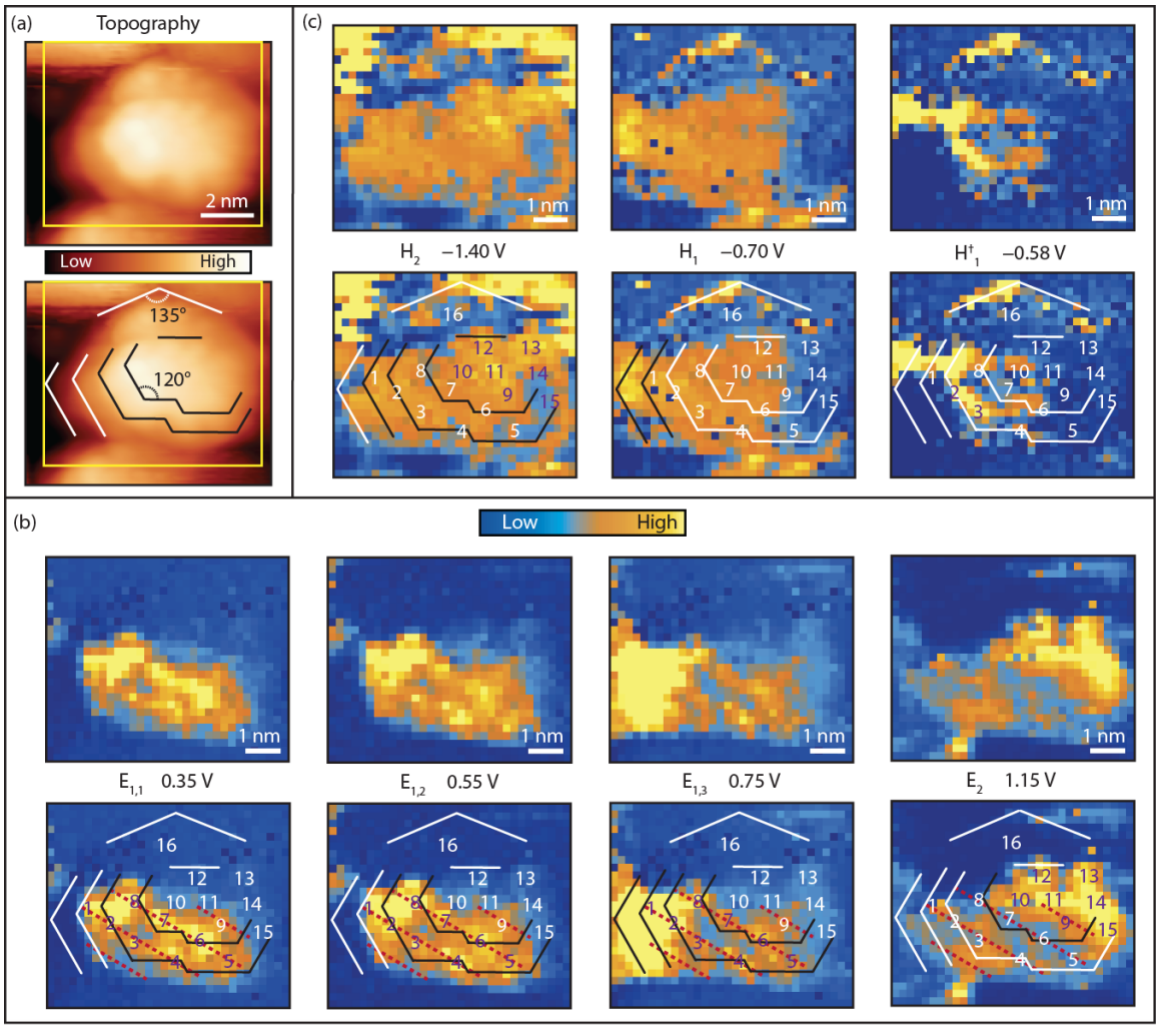

Figure 2.4. (a) Topographic images of NC_1 [set point 1.0 V, 1 pA]. Bottom image is marked to indicate step edges with 120° angles oriented along <110> directions, the same set of marks is used in the bottom images of (b) and (c) for reference. (b) DOS maps for unoccupied states of NC_1 [set point 2.0 V, 15 pA] measured at the indicated bias voltages. Parallel dashed red lines indicate the apparent orientation of stripe-like features associated with states $E_{1,n}$. (c) DOS maps for occupied states of NC_1 [set point 2.0 V, 15 pA] measured at the indicated bias voltages. High intensity signals in the top left and top right of the H_2 map in (c) are attributed to spectral features of nearby NCs. The spatial extent of maps in (b) and (c) corresponds to the yellow rectangle shown in (a). Numbered markers in the bottom images of (b) and (c) [identical for both sets of maps] indicate locations of high DOS intensity for states $E_{1,n}$ (1-9) and E_2 (10-15). Location 16 marks a region with a localized higher energy state [~1.9 V, map not shown], likely corresponding to a smaller NC (with a different crystallographic orientation) that is in the process of merging with NC_1.

Theoretical calculations show that unoccupied states in PbS are formed predominantly by Pb-derived atomic 6p orbitals, whereas occupied states are formed predominantly by S-derived atomic 3p orbitals.[30] According to these predictions, the DOS of states $E_{1,n}$ and $E_{2,}$ for un-passivated NCs, is carried by surface Pb-atoms, while the DOS of states $H_1^{\dagger}$, H_1 and H_2 is carried by surface S-atoms. The S- and Pb-character of occupied and unoccupied states correspondingly holds true even in the presence of under-coordinated Pb- or S-atoms, which form localized states split-off from the conduction- and valence-bands.[34] Because Pb- and S-atoms located at step edges lack nearest neighbors, they are in under-coordinated environments compared to other surface atoms, and therefore may form sub-band gap states.[35] Localization of states $E_{1,n}$ and $H_1^{\dagger}$ near the step edges, where atomic coordination is disrupted, suggests that these states correspond to sub-bandgap trap states, while the spatially delocalized states E_2, H_1 and H_2 are identified as quantum-confined states derived from the conduction (E_2) and valence (H_1 and H_2) bands. Consistent with the identification of states $E_{1,n}$ and $H_1^{\dagger}$ as states primarily localized on Pb- or S-atoms respectively, DOS maps for these states (Figure 2.3b,c) show complementary intensities in most of locations 1-15. The differences in the spatial distributions of states $H_1^{\dagger}$ and $E_{1,n}$ are attributable to the different spatial distributions of the under-coordinated Pb- and S-atoms, which is likely a result of the different quantities of Pb versus S atoms, as can be expected based on the fact that as-synthesized PbS NCs typically have Pb-rich surfaces.[36-37] Our spectroscopic data corroborates this expectation: the splitting of non-stoichiometric trap states from the main quantum-confined states has been predicted to be larger for NCs with greater non-stoichiometry,[34] and can thus be used as a measure of the degree of local non-stoichiometry. Specifically, on the energy scale, state $H_1^{\dagger}$ appears only 0.12 eV higher than

the onset of band H_1 in Figures 2.3b,c, which is comparable with calculations for states localized at S-atoms within step edges on the stoichiometric PbS(100) surface.[35] In contrast, the energy difference E_2 - $E_{1,1}$ is relatively large: ~0.8 eV. The same trends are observed in the spectra of most other NCs (Figure 1) suggesting that the number of under-coordinated Pb atoms is indeed higher than that of under-coordinated S-atoms in the studied NCs. These trends, and their consistency with the theoretical predictions[34] further reinforce our assignment of states $E_{1,n}$ and $H_1^{\dagger}$ as defect states.

Additional support for assignment of states $E_{1,n}$ as trap states is provided by the analysis of their energies in other studied NCs. Inspection of STS spectra of such NCs (Figure 1) shows that energy splitting E_2 - $E_{1,1}$ varies among different NCs, but does not show a correlation with their apparent bandgaps $E_{1,1}$ - H_1 (Figure S3). This is contrary to what would be expected if all states H_1, $E_{1,1}$ and E_2 had quantum-confined nature – in this case, according to STS results obtained on PbS NCs with similar aspect ratios,[26] state E_2 would be attributable to a higher-order particle-in-a-box-like state quantized in the Z-direction, which would mean that both energy differences E_2 - $E_{1,1}$ and $E_{1,1}$ - H_1 would scale with the NC thicknesses, resulting in a linear correlation between them. Since it has been established above that states H_1 and E_2 are delocalized and are of quantum-confined nature, state $E_{1,1}$ must be of different origin.

The origin of states $E_{1,n}$ may be alternatively explained by using the physical picture developed in several recent STS studies of ordered chain-like atomic structures,[38-40] where the linear-combination-of-atomic-orbitals (LCAO) model was applied to describe the observed extended electronic states formed through coupling of orbitals associated with individual adatoms. According to this physical picture, in the present case $E_{1,n}$ bands may

correspond to LCAO-like states formed through coupling of the orbitals associated with individual under-coordinated Pb atoms, with individual $E_{1,n}$ states roughly corresponding to different linear combinations of such orbitals. The model explains the presence of multiple states in STS spectra, as well as the similarity of their spatial DOS maps. The latter may only be different in their (spatial) nodal structures, which could not be resolved in our measurements.

While the precise atomic structure of the NC surface could not be determined from the collected STS data, the obtained maps of $E_{1,n}$ states suggest that the NC surface is reconstructed analogously to the reconstructions of the PbS(111) surfaces predicted by recent density functional theory calculations.[41] This study concluded that PbS(111) surfaces tend to reconstruct forming sub-monolayer stripe-like patterns of Pb adatoms. Indeed, our $E_{1,n}$ maps show stripes oriented at ~30° with respect to the step edges. Since the latter are aligned along the <110> crystallographic directions, the $E_{1,n}$ stripes are likely aligned with one of the <211> directions, consistent with self-assembly of surface Pb atoms in patterns defined by surface crystallographic directions, as would be expected on a reconstructed surface. Existence of well-defined patterns of non-stoichiometric Pb adatoms is also consistent with the observation of the well-defined progressions of STS features corresponding to $E_{1,n}$ states. Indeed, such STS features can be expected to be smeared out into featureless bands for less ordered NC surfaces, as was found for NCs annealed at lower temperatures (data not shown).

2.4. Conclusions

Our results suggest that self-assembly of non-stoichiometric adatoms on PbS NC surfaces may result in formation of extended LCAO-like sub-bandgap states, which have important implications for the more general case of imperfectly passivated ligand-covered NCs. Even when the density of dangling bonds per NC is small, the tendency of under-coordinated adatoms to co-localize near structural imperfections, as observed in our work, may lead to stronger electronic coupling of dangling bonds resulting in larger modifications of the sub-bandgap electronic structure than that expected for isolated dangling bonds. The atomic-scale spatial structure of these sub-bandgap states should have a strong impact on the photophysical properties of such NCs, and will be a subject of our future studies.

2.5. Acknowledgements

This work was supported in part by the SONY Corporation. PbS NCs were supplied by Voxtel Nano. The STM instrument used in this work was constructed with support from the U.S. National Science Foundation under Grant DMR-0960211.

2.6. Bridge to Chapter III

In this chapter we used STM/S to explore the surface and electronic structure of annealed, ligand free, PbS NCs. Comparison of the observed NC topographic and spatially resolved DOS maps revealed a connection between local NC surface structures and a manifold of localized electronic states observed at the NC conduction band-edge. In Chapter III, we broaden our STS exploration of PbS NCs to discuss a variety of observed electronic states across the bandgap region and attempt to connect these spatially resolved DOS features with observed crystallographic information of the measured NCs.

CHAPTER III
DIVERSITY OF SUB-BANDGAP STATES IN LEAD-SULFIDE NANOCRYSTALS: REAL-SPACE SPECTROSCOPY AND MAPPING AT THE ATOMIC-SCALE

This chapter by Christian F. Gervasi, Dmitry A. Kislitsyn, Thomas L. Allen, Jason D. Hackley, Ryuichiro Maruyama, and George V. Nazin was previously published under the same title in *Nanoscale* **2015**, 7 (46), 19732–19742

3.1. Introduction

Tuneable thin-film structures formed from lead-chalcogenide (PbX, where X=S, Se or Te) nanocrystals (NCs) are a promising class of semiconducting materials with a combination of unique functionalities that makes them highly attractive for a new generation of optoelectronic applications.[1-4] Some of these functionalities are made possible by the ultra-small size of NCs, with such examples as greatly increased efficiencies for exciton-multiplication,[5-10] and enhanced extraction of unrelaxed hot charge-carriers.[11] Another important functionality of NCs is the tunability of their properties via synthetic means, which allows one to systematically control the electronic bandgap by tuning the NC size. Additional means of control, to improve the injection and extraction of charge carriers in PbX NC thin films, have been implemented through post-synthesis techniques[12] involving ligand exchange.[13-15] Thus processed PbSe NC thin films show significantly reduced inter-particle

spacings and dramatically increased conductivities.[16-18] Less commonly, thermal annealing of the NC films is used,[15, 16, 19, 20] which can result in extensive rearrangements of ligand shells as well as (at higher temperatures) sintering[21] and even fusion[22, 23] of NCs. These processing steps, necessary for achieving optimal charge transport properties in NC films, simultaneously present significant challenges because they tend to radically alter the surface chemistry of NCs, with the potential to create surface imperfections that can result in the appearance of sub-bandgap trap states, which, in turn, have a strong impact on charge-carrier dynamics, recombination, and extraction from NC films.[24-26]

Indeed, recent breakthroughs in increasing the efficiency of PbX NC-based photovoltaic devices were made possible, to a great extent, by developments in surface passivation techniques that enabled a significant reduction in the density of surface trap states,[27, 28] with some of the reported efficiencies exceeding ~8%.[29, 30] Some of the promising approaches have employed passivation with 3-mercaptopropionic acid,[31] atomic passivation with halogen ions and SCN^-,[25, 32] and inorganic ligands,[33] metal halide and chalcogenide salts,[18, 34] amorphous alumina,[18] and alkyl selenide ligands.[35] Conceptually, complete elimination of trap states requires consideration of the "passivating effect" of individual surface ligands, and careful balancing of the number of ligands with the NC core stoichiometry, a difficult task in practice. In particular, theoretical calculations show that in the limiting case of ligand-free stoichiometric NCs, mid-gap states do not exist,[36, 37] but in non-stoichiometric Pb-rich (Pb-poor) NCs sub-bandgap states are found near the conduction (valence) bands.[36, 38] A similar picture holds for ligand-passivated NCs:

attachment of ligands effectively changes NC stoichiometry, such that an appropriate number of ligands can effectively compensate for the non-stoichiometry of the NC core, and eliminate the sub-bandgap states.[38] The importance of NC stoichiometry in defining the NC electronic structure is corroborated by recent experimental studies where the trap state densities were found to be sensitive to controlled variations in NC stoichiometry achieved either through post-synthesis ligand exchange,[35] direct thermal deposition,[39] solution-based colloidal atomic layer deposition,[40] and successive ionic layer adsorption and reaction (SILAR).[41]

Optimization of the "effective" NC stoichiometry is complicated by the varied chemistry of facets associated with different crystallographic directions (typically {111}, {100} and, to a lesser extent, {110}[42]).[35] A stark manifestation of this variability is the fact that unlike stable {110} and {100} surfaces,[43, 44] (un-passivated) polar {111} surfaces are unstable and are predicted to undergo reconstruction resulting in formation of an ordered sub-monolayer of Pb atoms.[45] Evidence for surface reconstruction is provided by Rutherford backscattering experiments on PbSe thin films, where a sub-monolayer (~40%) of Pb atoms, consistent with surface reconstruction, was found.[46] Additional evidence was provided by TEM imaging of PbSe NC {111} facets showing ribbon-like Pb structures attributed to surface reconstruction.[45]

While considerable advances in controlling the properties of PbX NC films have been made, and several theoretical studies showing the importance of surface trap states are available,[25, 38, 47] the role of surface trap states in the physical picture of charge-carrier photo-generation and dynamics remains to be fully addressed.

Experimental studies of surface trap states have been carried out using a variety of techniques. Photoluminescence studies showed the existence of trap states in as-synthesized ligand-passivated PbX NCs,[48, 49] even before NC film formation. Photoluminescence measurements of ligand-exchanged PbX NC films demonstrated the presence of trap states[31, 50] that could be manipulated with NC size and surface treatment.[31, 49] Trap states in ligand-exchanged PbX NCs were also found in studies utilizing deep-level transient and Fourier-transform photocurrent spectroscopies,[51] and in spectroscopic measurements of photocurrent in PbS field-effect transistor devices.[52] Even though these studies have provided rich insights into the spectroscopic properties of surface trap states, they lacked the spatial resolution to visualize the relationship between the local structure of NC surfaces and properties of such states. The capability to probe this relationship is critically important for the development of a microscopic picture of surface trap states because of the wide diversity of local atomic-scale surface structures associated with variations in ligand-shell morphologies, the presence of different crystallographic facets, NC shape variations, and the effect of surface reconstruction.

A direct spectroscopic approach for real-space investigations of surface states in individual NCs is afforded by a combination of Scanning Tunneling Microscopy (STM) and Scanning Tunneling Spectroscopy (STS), which have been used to probe the electronic states in ligand-exchanged PbS NC films.[53, 54] Realization of this technique in a high-stability cryogenic STM system[55] enables detailed atomic-scale mapping of electronic states in individual NCs. STS-based mapping of the local density of states (DOS) was recently used to study the spatial localization and spectral properties of sub-bandgap states

in NCs arising due to local off-stoichiometry.[56] Here we apply this experimental approach to obtain *atomic-scale* DOS maps of individual ligand-free PbS NCs. Ligand-free NCs represent a well-defined model PbX system, unaffected by the uncontrolled variances of the ligand shell morphology, which makes this system more open to theoretical simulations.[44, 57, 58] STS maps show that the majority of studied NC surfaces underwent reconstruction accompanied by formation of ordered atomic patterns commensurate with the crystallographic structures of the NC surfaces. While these results are in accordance with density-functional theory calculations of polar PbS surfaces, where similar modes of surface reconstruction were predicted,[45] the current manuscript reports, for the first time, results demonstrating the connection between the atomic-scale NC surface morphology and atomic-scale variations in the electronic DOS. Importantly, we find that NC surface reconstruction results in formation of surface-bound sub-bandgap electronic states, with spectral and spatial properties sensitive to the local stoichiometry of NC surfaces. In addition, we find that highly off-stoichiometric NC regions show qualitatively different defect states with energies deep inside the NC bandgaps. By employing results of calculations for off-stoichiometric PbX NCs,[38] we infer the presence of off-stoichiometric areas from local DOS spectra, and use DOS maps to analyze the local spatial variations in stoichiometry.

3.2. Experimental Methods

A Au(111) substrate surface was prepared, under ultra-high vacuum conditions (~10^{-11} Torr), by several cycles of sputtering/annealing, using Ne gas, and annealed at ~400°C. Pentanethiol-terminated PbS NCs were synthesized as described previously,[56] suspended

in pentane, and deposited onto the Au(111) surface using a solenoid pulse-valve. During deposition, the Au(111) substrate was held inside the load-lock section of the vacuum system, with the pressure not exceeding 10^{-6} Torr during deposition. Several successive bursts of the solenoid valve were used to obtain a sub-monolayer of PbS NCs on the Au(111) surface. The Au(111) substrate with deposited NCs was annealed in ultra-high vacuum conditions at increasingly higher temperatures until well-defined reproducible STM imaging of individual NCs was achieved, with a final annealing temperature of ~170°C.

Experiments were conducted using a home-built ultra-high-vacuum STM incorporating a Pan-type scanner provided by RHK Technology.[55] All STS spectra were recorded using a lock-in amplifier operating at a modulation frequency of ~600 Hz, and bias voltage modulation varying from ~10 mV (for individual spectra and one-dimensional spatial DOS maps) to ~50 mV (for two-dimensional DOS maps). All STM images and STS spectra were obtained at a temperature of ~15 K with electrochemically etched Ag tips.

3.3. Experimental Results

3.3.1. Sample Preparation

PbS NCs with pentane-thiol ligand shells were deposited on Au(111) surfaces and annealed at progressively higher temperatures until ligands were removed. The removal of ligands was monitored with STM imaging, which, at the initial stages of annealing, typically showed fuzzy patterns consistent with dynamic reorientation of ligands present on the NC surface (Figures 3.1a-c). At the final stages of annealing, the majority of NCs showed reproducible topographic patterns suggesting the absence of ligand reorientation

(Figures 3.1d-f). In addition, STM images of fully-annealed NCs showed disc-like width-to-height aspect ratios of 2:1 to 3:1 suggesting that significant reconstruction of the overall shapes of NCs occurred during the annealing process. The disc-like shapes of annealed NCs are consistent with similar shapes of PbS and PbSe NCs grown by electrodeposition on Au(111).[59, 60]

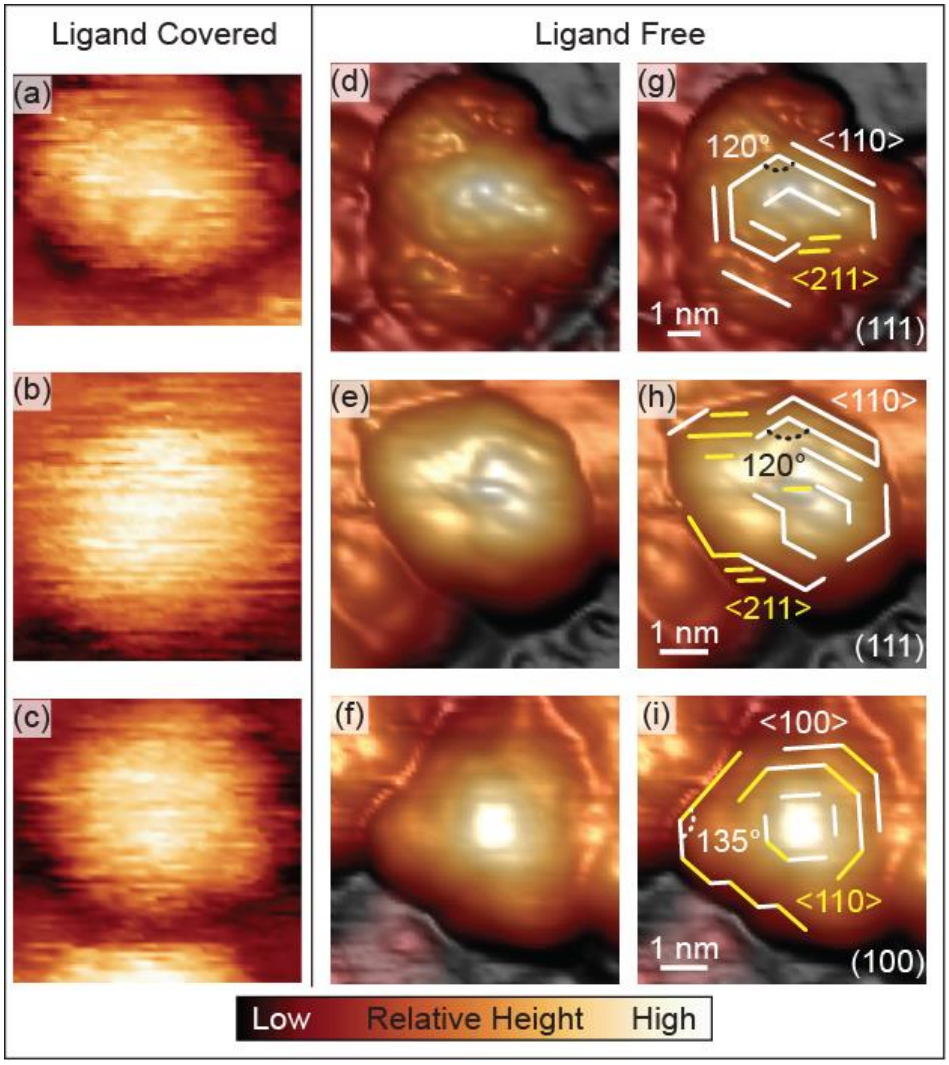

Figure 3.1. STM topographies of ligand-covered (a)-(c) and ligand-free (d)-(f) PbS NCs. Figures (g)-(i) highlight topographical features observed in (d)-(f). The crystallographic directions and NC boundaries are identified with the aid of STS DOS mapping. All STM topographies measured with setpoint 2.0 V bias, 1-2 pA tunneling current.

The predominance of disc-like shapes in a polar material like PbS, is attributable to the reduced electrostatic NC energy (due to screening by the gold surface) enabled by this geometry. Importantly, images of fully-annealed NCs often showed surface features aligned at specific angles attributable to well-defined crystallographic directions in PbS NCs (Figures 3.1g-i). The majority of fully-annealed NCs showed topographic features (e.g. NC boundaries and topographic steps) oriented along three main spatial directions (specific to each NC) forming 120-degree angles with respect to each other (Figures 3.1g and h), even though other orientations have also been observed (Figure 3.1i). The existence of such directional order suggests that the top-most NC surfaces (in most cases) roughly correspond to {111} crystallographic surfaces, consistent with results of TEM studies of PbS NCs terminated with Au clusters,[61] where the polar nature of the {111} facets was reported to lead to preferential formation of Au/PbS{111} interfaces. Results described in the following summarize our studies of 10 fully-annealed individual PbS NCs.

3.3.2. DOS Spectroscopy of NCs

Energy-dependent DOS spectra (STS spectra) of individual PbS NCs were recorded by measuring the differential tunnelling conductance, dI/dV, as a function of the bias voltage (see Methods for details of the measurements).[62] DOS spectra for all fully-annealed NCs show progressions of peaks associated with occupied (negative bias) and unoccupied (positive bias) electronic states (Figure 3.2a). Indeed, while Figure 3.2a shows considerable variations in the apparent band gaps ($E_{1,1}$ - H_1 energy difference) for different NCs, the DOS spectra, overall, appear quite similar and reminiscent of those calculated for stoichiometric ligand-free PbX NCs,[44, 57, 58] where the electronic states can be described as

quantum-confined particle-in-a-box (PIAB) states originating from the conduction and valence bands. The lowest-energy PIAB states are predicted to show s- and p- overall orbital symmetries, with their atomic-scale behaviour determined by the corresponding Bloch wavefunctions.[57] A similar picture of PIAB-like electronic states has been used to describe STS spectra for a variety of NCs composed of different semiconductor materials.[63] Then, taking into account the disk-like aspect ratio of studied NCs, the unoccupied states in Figure 3.2a could be assigned in the following way: the doublet of closely spaced peaks $E_{1,1}$ and $E_{1,2}$, may be attributed to electronic states quantized in the XY plane (with $E_{1,1}$ being the ground state), whereas the E_2 state may be attributed to a single-node state quantized in the Z-direction.[59] By using the PIAB-like picture of electronic states in Figure 3.2a, the variations in the apparent bandgap ($E_{1,1}$ - H_1 energy difference) could then potentially be explained by variations in NC dimensions, which would modulate the energies of the PIAB states via quantum-size effects.[64]

Figure 3.2. (a) DOS spectra for six representative PbS NCs (individual spectra shifted for clarity). Occupied (unoccupied) states denoted by H_n (E_n) respectively. All dI/dV curves measured with set-point 1.6-2.6 V bias, 15-30 pA tunneling current. Histogram (bottom) of energetic locations and distributions for discernible states $E_{1,1}$, E_2, and H_1 for 13 NCs, bin size 0.2 eV (b) Bandgaps vs. height for measured NCs overlaid on data for two limiting cases: spherical NCs and 2D PbS quantum wells. Open symbols correspond to the $E_{1,1}$ - H_1 energy differences, whereas closed symbols correspond to values obtained from PIAB orbitals differences of many measured DOS spectra in Figure 2a are considerably lower than those (as determined from DOS mapping). The curve for spherical PbS NCs, and gray shaded region corresponding to 2D PbS quantum wells, were obtained from Moreels et al.[65] and Lee et al.,[66] respectively.

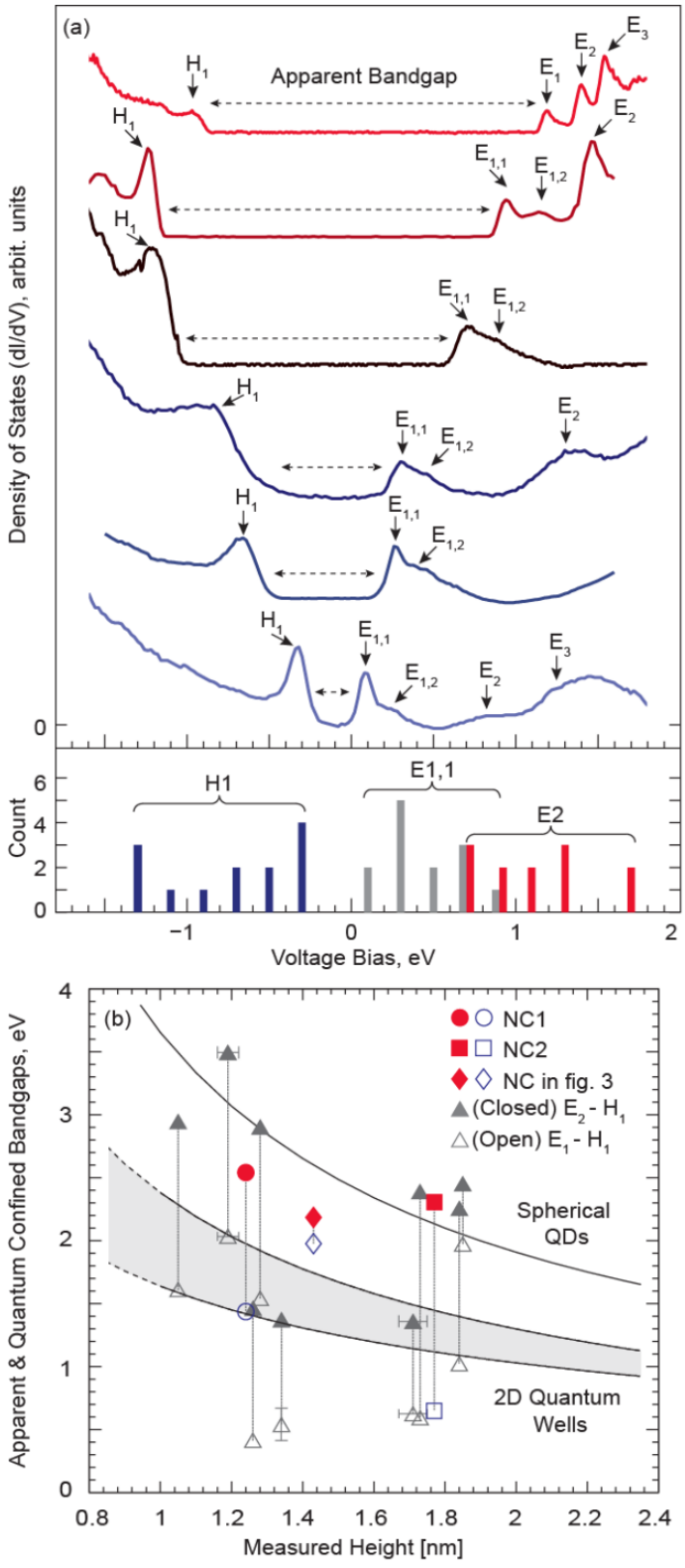
(a)
Apparent Bandgap
H1
E1
E2
E3
E1,1
E1,2
Density of States (dI/dV), arbit. units
Count
H1
E1,1
E2
Voltage Bias, eV
(b)
NC1
NC2
NC in fig. 3
(Closed) E2 - H1
(Open) E1 - H1
Spherical QDs
2D Quantum Wells
Apparent & Quantum Confined Bandgaps, eV
Measured Height [nm]

The PIAB-like picture of electronic states in Figure 3.2a is challenged, however, by the fact that the spacing between peaks $E_{1,1}$ and $E_{1,2}$ does not change appreciably from one NC to another, being consistently in the range of ~0.2 eV despite significant variations in the NC lateral sizes. Further, the apparent bandgaps ($E_{1,1}$ - H_1) energy expected based on the physical dimensions of the corresponding NCs. Indeed, many of the apparent bandgaps are lower than what would be expected for two-dimensional PbS films of thicknesses matching the observed NC heights (Figure 3.2b),[67] which is the absolute minimum expected for NCs with large spatial dimensions in the XY plane. On the other hand, energy differences calculated from E_2 - H_1 (and in some cases E_2 - H_2) tend to fall in the range expected for bandgaps of disc-like PbS NCs (Figure 3.2b). Together, these observations suggest that $E_{1,1}$ states in Figure 3.2a do not have PIAB-like character, and may potentially be associated with sub-bandgap states. Theoretical calculations predict that sub-bandgap states are often more strongly localized than PIAB-like states derived from the conduction and valence bands,[38, 47] which suggests that to establish the nature of electronic states observed in Figure 3.2a, it would be useful to obtain information regarding their spatial behaviour. To this end, we carried out spatial mapping of DOS spectra for several NCs, as described below.

3.3.3. Surface-Reconstruction observed in DOS maps: Results

We first present DOS maps for NCs that showed DOS delocalized over the NC surfaces. For example, Figure 3.3 shows a “cross-sectional” DOS mapping for a NC without apparent spectral or spatial features attributable to sub-bandgap states. Indeed, the apparent bandgap of this NC falls within the range expected for disc-like NCs (Figure 3.2a,

diamond-shaped data-point), unlike the majority of studied NCs. The DOS map (Figure 3.3b) is composed of a progression of DOS spectra measured across the NC, as shown in Figure 3.3a. In Figure 3.3b, occupied state H_1 and all unoccupied states E_n are visible throughout the scan (even though they also show some variations in their intensities), which suggests that they may correspond to delocalized PIAB-like states.

While delocalized states analogous to those of Figure 3.3b were observed for many other NCs, their maps were often different from that of Figure 3.3b in that they showed quasi-periodic spatial modulations of their DOS intensities. An example of a "cross-sectional" DOS map for one such NC (referred to as NC1 in the following) is shown in Figure 3.4. The DOS spectra measured at different locations on the NC1 surface show a similar grouping of occupied and unoccupied states with intensities modulated depending on the measurement location (Figures 3.4b and c). In particular, distinct modulations are observed for states H_1, $E_{1,1}$ and $E_{1,2}$ (Figure 3.4b). These modulations occur on a spatial scale far exceeding the unit cell of PbS (0.59 nm), suggesting that they are not a product of elemental contrast originating from the PbS lattice. The magnitudes of $E_{1,1}$ - H_1 and E_2 - H_1 bandgaps for NC1 (Figure 3.2a, open and closed circle data-points) suggest the presence of sub-bandgap states.

To further investigate the spatial behaviour of electronic states in NC1, we recorded DOS spectra across a two-dimensional grid of points covering (roughly) the spatial extent of NC1. 2D-spatial maps of electronic states are obtained from this DOS dataset by taking values of the DOS at select bias voltages. Such 2D-maps for the most prominent occupied and unoccupied states are shown in Figure 3.5 and in supplementary Figures S1 and S2. The 2D-spatial maps in Figure 3.5 show that individual states in NC1 have very different

characters, except in the $E_{1,n}$ states (Figures 3.5c, and S1c-e), as well as states H_1 and $H^{\dagger}$(Figures 3.5d,e; S2a,b), which exhibit similar features and spatial localizations respectively. All 2D DOS maps in Figure 3.5 show highly inhomogeneous spatial distributions with stripe-like "hot spots" oriented parallel to the <110> crystallographic features observed in the STM topography of NC1 (Figure 3.1g).

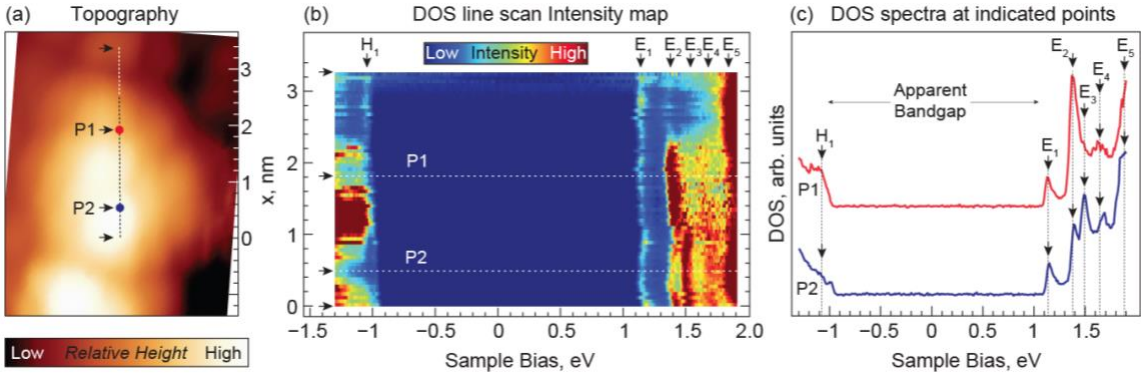

Figure 3.3. (a) STM topographic image of a PbS NC. (b) DOS "cross-section" mapping along the path of the dotted line in (a). (c) Individual DOS spectra measured at locations marked in (a). STS measurements in (b) and (c) were taken with a set-point of 1.9 V bias and 30 pA tunneling current. Variations in the energies of electronic states across the NC roughly follow the NC topography, which is a result of the locations-specific variation of the bias voltage drop inside the NC.[56]

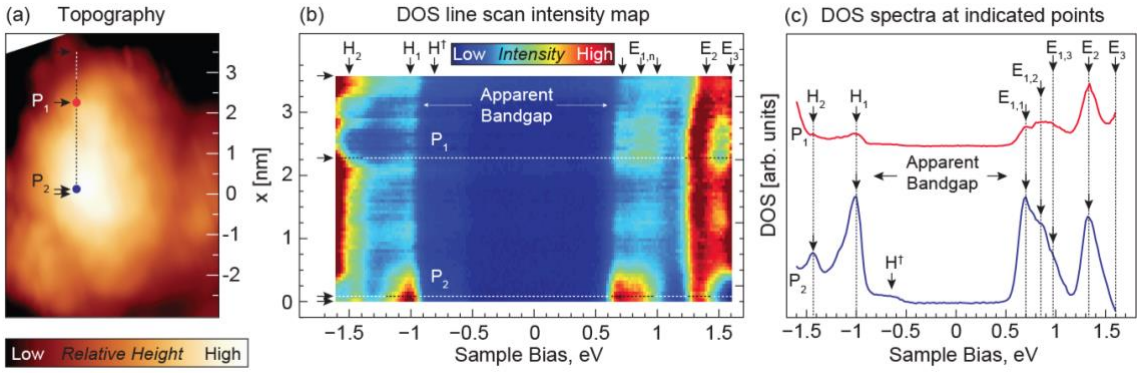

Figure 3.4. (a) STM topographic image of NC1. (b) DOS mapping of NC1 along the path of the dotted line in (a). (c) Individual DOS spectra for locations marked in (a). STS measurements in (b) and (c) were taken with set-point 1.6 V, 30 pA tunneling current.

For example, the DOS map of state E_3 (Figure 3.5a) shows two pairs of parallel bright "stripes" (marked by solid black lines in Figure 3.5a). The "stripes" in each pair are separated by distances equal to 0.726 nm, which is a close fit to the distance between atomic rows located in two different {211} planes. In the following this distance is defined as 3α, where α is the distance between two neighbouring {211} planes, as shown in the model in Figures 6a and b. The two pairs of bright stripes in Figure 3.5a are separated by a distance of 0.968 nm = 4α, which corresponds to the geometry shown in the model in Figure 3.6b, where, in contrast to the model in Figure 3.6a, one of the atomic rows is located in a different (lower) {111} atomic plane. This geometry is consistent with the topography of NC1 (Figure 3.1d), which shows atomic steps separating the regions with the two pairs of DOS stripes seen in Figure 3.5a. The DOS map of state E_2 (Figure 3.5b) shows somewhat less-developed structural order, but features aligned along the same set of black lines are visible.

In contrast, DOS maps of $E_{1,n}$ states (Figures 3.5c, and S1c-e) show a different set of bight DOS "stripes" (marked with black lines), which are however, separated by the same distance of 0.726 nm = 3α as found in Figure 3.5a. In addition, all of the DOS "stripes" in Figures 3.5c, and S1c-e are either parallel to, or are oriented at exactly 60° with respect to the DOS "stripes" from Figure 3.5a, which is consistent with the mutual orientation of two different sets of {211} planes, as shown in the model in Figure 3.6a. This, together with the spacing of DOS "stripes" in maps of $E_{1,n}$ states, suggests that the latter have a similar relationship with the PbS crystallographic structure as features found in the maps of states E_3 and E_2. Stripe-like features similar to those found in maps of $E_{1,n}$ states, are also observed for states $H^{\dagger}$ and H_1, (black lines in Figures 3.5d and e). The DOS map of state

H_2 (Figure S2c) shows somewhat less-developed order, with several features orthogonal to the bright {211} plane features observed throughout (especially in Figures 3.5a,b) suggesting that they lie in {110} planes of NC1. This assignment is supported by the fact that these features are separated by distances of ~0.838 nm = 4β, where β is a distance between two neighbouring {110} planes, as shown in Figures 3.6c and d.

The spatial order observed in the DOS maps of NC1 allows us to draw several conclusions. First, the fact that the orientations of bright DOS features in Figures 3.5, S1 and S2 are in registry with the crystallographic directions and lattice spacings expected for a (111) surface, supports the conclusion (originally based on features observed in STM imaging – Figure 3.1g) that one of the {111} crystallographic planes of NC1 is parallel to the Au(111) surface. By associating the DOS features with specific crystallographic directions, we are also able to identify orientations of topographic features in Figure 3.1g as corresponding to different <110> directions. Further, the consistency of the spacing observed for these bright DOS features in all maps of Figure 3.5, S1 and S2 with the crystal structure of PbS suggests that these features are indeed associated with an atomic geometry analogous to that seen in the model of reconstructed PbS {111} surfaces displayed in Figure 3.6, even though the actual morphology of NC1 is more complex.

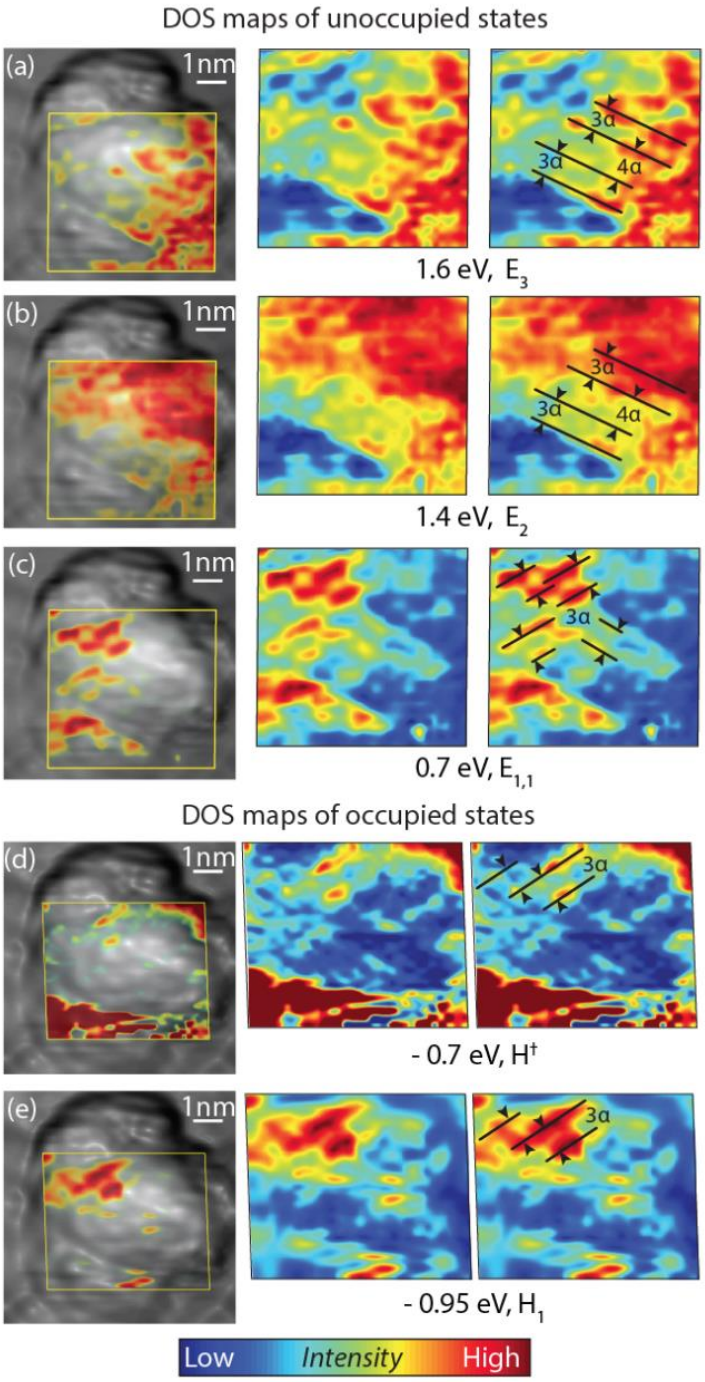

Figure 3.5. 2D DOS maps of unoccupied (a-c) and occupied (d, e) states for NC1. DOS state representations show (from left to right) combination topography/DOS map overlay (yellow outline indicates area of DOS mapping), DOS map only, and DOS map with black lines showing DOS features that are in registry with NC1 crystallographic features from Figure 1g. Parameter α is distance between two neighboring {211} planes, as shown in the model in Figures 6a and b. STS measurements taken with set-point 1.6 V bias, 30 pA tunneling current. STM topography image measured with set-point 2.0 V bias, 2 pA tunneling current.

3.3.4. Surface-Reconstruction: Discussion

The distances between the stripe-like features in Figures 3.5, S1 and S2 are larger than the minimal inter-atomic distances expected for the identified crystallographic directions. As the idealized model in Figure 3.6 illustrates, this may result from a geometry where rows of atoms are missing on the PbS surface. Such surface morphology is consistent with the predicted reconstruction of the PbS(111) surface.[45] Indeed, the polar nature of PbS dictates that termination of a NC with a {111} facet composed of only one element is electrostatically unfavourable. Instead, reconstruction of the PbS(111) surface is predicted, where, in the ideal case, a {111} facet is stabilized by an additional ordered half-monolayer composed of the complementary element.[45] While different configurations of the additional half-monolayer are possible, one of the configurations that is predicted to give the lowest overall energy has a structure with atoms missing in every alternate {211} plane, as shown in the model in Figure 3.6a. This structure results in rows of atoms oriented and spaced in a manner identical to the arrangement of bright rows in the DOS maps of NC1, which strongly suggests that the observed NC1 DOS features are caused by surface reconstruction.

To establish the composition of the reconstructed layer as well as the nature of electronic states in Figures 3.5, S1 and S2, we compare these results to theoretical predictions. Electronic structure calculations for unpassivated PbS NCs of different shapes show that in PbS, unoccupied states are primarily formed from atomic 6p-orbitals of lead, while occupied states are primarily formed from atomic 3p-orbitals of sulfur.[44] This distinction is maintained regardless of the NC shape and stoichiometry,[38] which is important for the case of NC1, since the model surface reconstruction shown in Figure

3.6a results in surface adatoms in non-stoichiometric environments. We thus expect that states $E_{1,n}$, E_2 and E_3 must be carried predominantly by surface Pb-atoms, whereas states $H^{\dagger}$, H_1 and H_2 must be carried predominantly by surface S-atoms. Moreover, non-stoichiometric Pb-atoms (or S-atoms), are predicted to form localized sub-bandgap states split-off from the conduction-band (or valence-band for S-atoms).[38] This prediction implies that since $E_{1,n}$ states are the lowest-energy unoccupied states, they must be associated with non-stoichiometric Pb-adatoms. The strong localization of $E_{1,n}$ "hot spots" along the specific crystallographic lines associated with reconstruction features further reinforces this assignment.

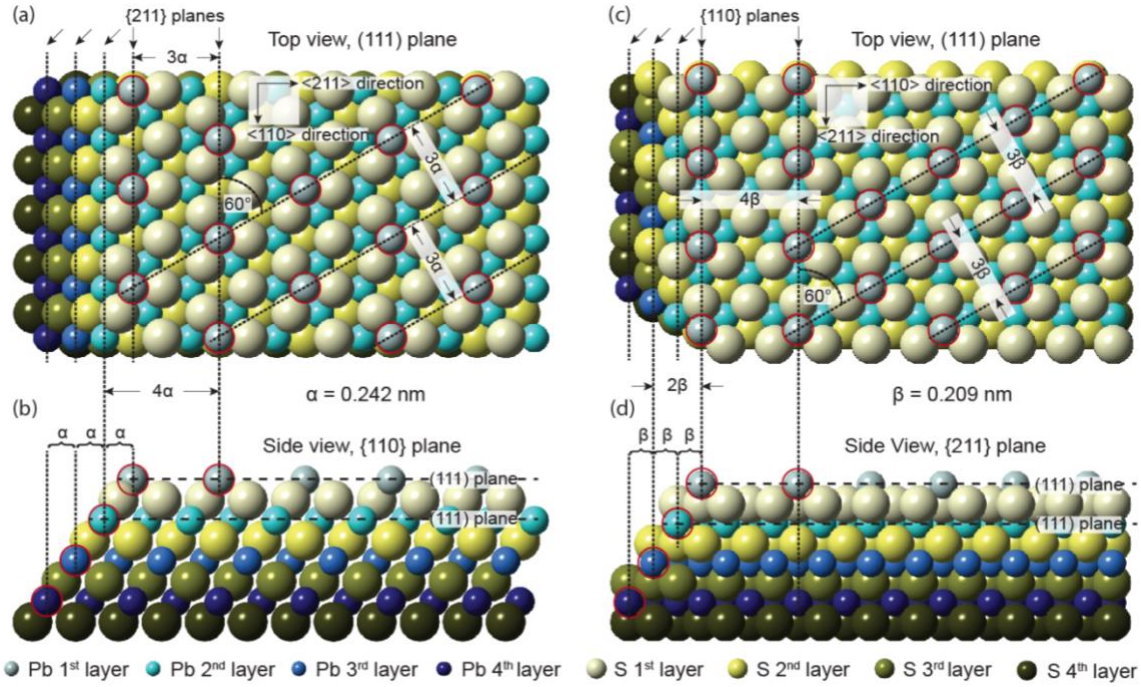

Figure 3.6 Model representations of relevant PbS fcc crystallographic facets with idealized reconstruction features. (a, c) (111)-plane views showing rows of Pb adatoms oriented along <110> and <211> directions respectively, with indicated inter-atomic-row distances in integer multiples of distances α and β respectively. (b, d) (110)-, and (211)-plane side-views of the same features as in (a) and (c) showing vertical atomic steps responsible for appearance of varied distances between the bright DOS "stripes" in Figure 5 and Figure 8.

In contrast, the high degree of delocalization of states E_2 and E_3 identifies them as quantum-confined PIAB states with spatial distributions modulated by the presence of the periodic surface structures formed from Pb-adatoms. Analogously, the spatial localization of states $H^{\dagger}$ and H_1 suggests that they correspond to surface states produced by reconstruction, whereas state H_2 should correspond to a PIAB state. These assignments of the origins of the different NC1 states are supported by the fact that the NC1 bandgap calculated as E_2 - H_2 is in the correct range for a disk-like NC (determined from Figure 3.2b), unlike the apparent bandgap $E_{1,1}$ - H_1, which is at the extreme low end of values corresponding to a 2D PbS thin film.

Identification of states $E_{1,n}$ as states carried by reconstructed Pb-adatoms allows us to address the existence of multiple peaks in the $E_{1,n}$ band, an observation that was common for most studied PbS NCs. Indeed, most of the DOS spectra measured on PbS NCs showed at least two $E_{1,n}$ states, separated in all spectra by roughly 200 mV (Figure 3.2a). This energetic separation is much larger than the typical vibrational energy scale of PbS,[68] which rules out current-induced vibrational excitation of NCs[69] as a potential cause for the appearance of multiple $E_{1,n}$ peaks. Instead, the existence of $E_{1,n}$ bands may be rationalized by considering adatom-adatom electronic coupling that has been shown to lead to formation of "bonding" and "anti-bonding" electronic states.[47] This interaction mechanism suggests a scenario analogous to that described in a number of recent STS studies of atomic structures similar to that exhibited in the model in Figure 3.6a, where ordered rows of atoms adsorbed on surfaces with well-defined crystallographic order were investigated.[70-72] In these studies, formation of extended electronic states was qualitatively described using the

linear-combination-of-atomic-orbitals (LCAO) model. By using this model, $E_{1,n}$ bands may be similarly attributed to LCAO-like electronic states formed from orbitals of under-coordinated Pb adatoms, such that individual $E_{1,n}$ states should correspond to distinctly different linear combinations of atomic orbitals. This physical picture not only explains the presence of multiple $E_{1,n}$ states, but also the close similarities in their 2D DOS maps (Figures 3.5c, S1c-e): because these states are formed from the same atomic orbitals, their linear combinations should only differ in their mutual phases, and should produce the same spatial distributions.

3.3.5. NCs with Edge-Defects

While the delocalized $E_{1,n}$ states caused by surface-reconstruction were found in almost all of the studied NCs, a *qualitatively different* type of sub-bandgap state attributable (as will be shown in the following) to surface defects was also observed in several NCs. DOS spectra showing these defect states for a representative NC (this NC is referred to as NC2 in the following) are shown in Figure 3.7. Unlike $E_{1,n}$ states, these defects exhibited a substantial DOS on the occupied side of the STS spectra (states $H^{\dagger}$, $H_{1,1}$ and $H_{1,2}$ in Figure 3.7), while defect-related DOS features appearing on the unoccupied side were often less pronounced (state $E^{\dagger}$ in Figure 3.7) or absent (see Figure S5 for additional NCs showing similar defect-related states). In contrast to $E_{1,n}$ states, the defect states were tightly localized, as can be seen, for example, from the dramatic differences in DOS spectra measured in neighbouring points P1 and P3 in Figure 3.7.

To visualize the entire spatial extents of these defect-states, we carried out 2D DOS mapping using the experimental approach described above for NC1. Maps of unoccupied states for NC2 (Figures 3.8a-c and S3) show a progression of $E_{1,n}$ and E_2 states analogous

to that of NC1 (Figure 3.5), as well as state $E^{\dagger}$ (Figure 3.8c). For NC2, however, the high-intensity DOS "stripes" of states $E_{1,n}$ and E_2 are oriented at an angle of 30° with respect to the NC2 edges, and exhibit spacings of 0.42 nm = 2β and 0.63 nm = 3β suggesting that these "stripes" are associated with a *different type* of surface reconstruction with atomic self-assembly along <211> directions, as shown by the atomic model in Figures 3.6c and 3.6d.

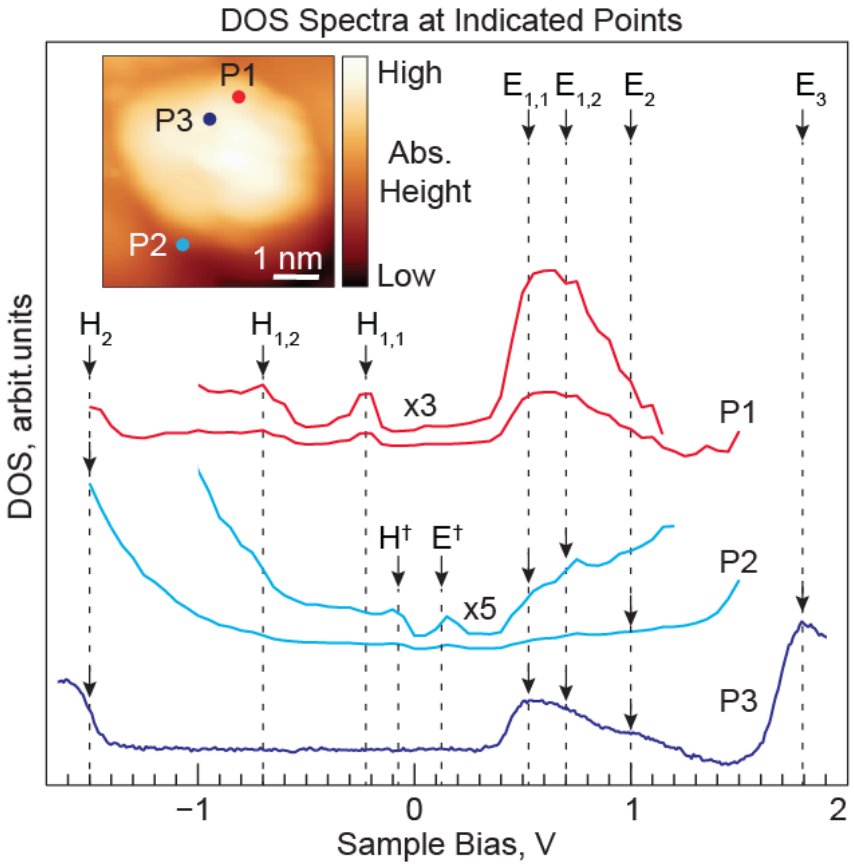

Figure 3.7. DOS spectra for NC2 measured at locations P1-3 shown in the inset STM topography. Sections of spectra P1 and P2 containing relevant states have been magnified by designated amount for clarity. STS measurements were taken with set-points of 1.5-2.2 V bias, 10-20 pA tunnelling current. STM topography image measured with set-point 2.0 V bias, 1 pA tunnelling current.

DOS maps of occupied states $H_{1,n}$ and H_2 (Figures 3.8d,e and S4b-d) show a progression analogous to that of $E_{1,n}$ and E_2, except that DOS "stripes" in maps of $H_{1,n}$ show reconstruction along a <110> crystallographic direction. In addition, the nature of this reconstruction pattern is different from that of $E_{1,n}$ states: comparison of $H_{1,n}$ and $E_{1,n}$ maps for NC2 shows that these states are anti-correlated in intensity on the atomic scale (Figure S6), which suggests that $H_{1,n}$ and $E_{1,n}$ patterns are formed by atoms corresponding to different elements. As with NC1, $E_{1,n}$ states in NC2 should be primarily carried by Pb-atoms, which means that $H_{1,n}$ states should be carried by S-atoms. This conclusion is further strengthened by the results of theoretical calculations, which, in the absence of strong non-stoichiometry, predict that occupied states should be formed mainly from 3-p orbitals of sulphur atoms.[38]

A spatial distribution that is dramatically different from previously considered reconstruction-induced states are found for the lowest-energy unoccupied state $E^{\dagger}$ (Figure 3.8c) and highest occupied state $H^{\dagger}$ (Figure 3.8d), which are both strongly localized near the bottom-left boundary of NC2. States localized near the same part of the NC2 boundary, almost identically to the localization patterns of $E^{\dagger}$ and $H^{\dagger}$, are also identifiable in all maps for the remaining occupied states (Figure 3.8d,e and S4a-d). The very small apparent bandgap ($E^{\dagger}$ - $H^{\dagger}$) associated with these "boundary states", together with the high degree of their spatial localization, suggests their defect-related origin. The spectral characteristics of these states are analogous to those obtained in model DFT simulations of highly off-stoichiometric PbS NCs.[38] As discussed earlier, in these calculations, excess of Pb (S) atoms leads to the appearance of split-off states below (above) the PIAB-like conduction

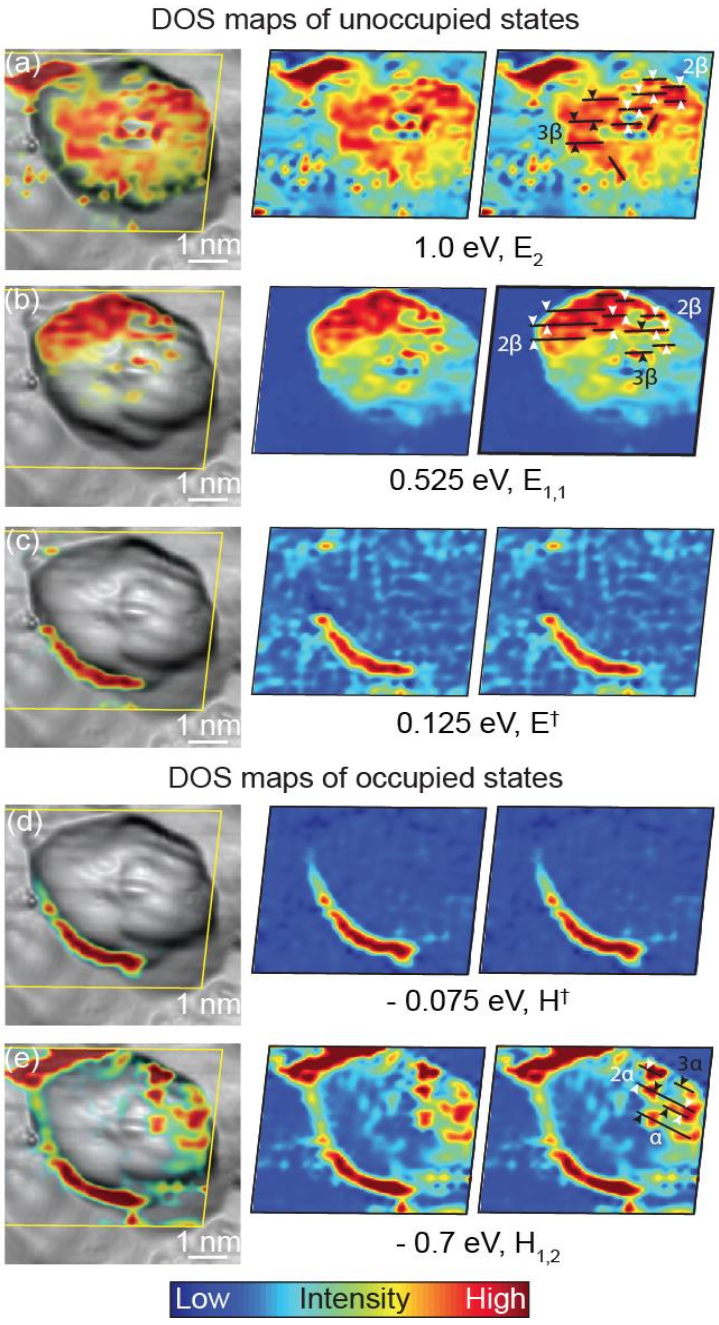

Figure 3.8. Same as Figure 5 for NC2. Parameters α and β are the distances between two neighboring {211} and {110} planes respectively, as shown in the model in Figures 6. STM topography image measured with set-point 2.0 V bias, 1 pA tunneling current. STS maps measured with set-point 1.5 V bias, 20 pA tunneling current.

(valence) band states. In highly off-stoichiometric conditions, the energies of split-off states become sufficiently low (high) for them to appear on the occupied (unoccupied) side of DOS spectra. Thus, because with the exception of state $E^{\dagger}$, no other unoccupied "boundary states" are observed (Figures 3.8a,b), and, in contrast, "boundary states" are observed in maps of all occupied states, we associate the "boundary states" with sulfur-rich areas of NC2.

This assignment is consistent with the presence of extra sulfur atoms in the areas of states $H_{1,n}$, (top-right area of NC2 in Figures 3.8e and S4b,c), which are also localized near the NC2 boundaries: the near-boundary localization of states $E^{\dagger}$, $H^{\dagger}$ and $H_{1,n}$ suggests that they could have been formed in a similar fashion, possibly due to migration of some of the Pb atoms to the Au(111) surface during annealing. Indeed, migration of Pb atoms to the Au substrate appears necessary to explain the existence of sulfur-rich areas, since as-synthesized PbS NCs are known to have Pb-rich surfaces.[65, 73]

3.4. Conclusion

Our results show that reconstruction of polar PbS surfaces can produce a wide variety of sub-bandgap states with spatial structures and energies sensitive to the local stoichiometry. Both unoccupied and occupied trap states can be created in Pb-rich and S-rich areas, correspondingly. Wide bands of trap states crossing over the Fermi level can also exist in areas with sufficient local off-stoichiometry. The fact that the $E_{1,n}$ states were observed in the majority of fully annealed NC DOS suggests that most of these NCs underwent surface reconstruction. Indeed, one can expect this behavior to be common for ligand-free NCs, since their surfaces are likely to terminate with (111) facets, which are prone to reconstruction due to their polar nature.[45] This is consistent with DFT calculations,

which show that unreconstructed (111) facets, are, in fact, unstable, and stability is only obtained for non-polar reconstructed facets.[45] In contrast, other facets corresponding to main crystallographic directions (100) and (110) are stable in their unreconstructed forms.[45]

The presented results are directly applicable to thermally-processed NC solids, where loss of ligands is likely. Similar structure-dependent effects in the local DOS can also be expected for under-stoichiometric surfaces of ligand-passivated PbX NCs, where ligand self-assembly at the PbX-ligand interface may proceed with formation of surface-bound sub-bandgap states, as also suggested by calculations for CdSe NCs.[74, 75] The STS-based characterization approach demonstrated in the present manuscript is applicable to NCs passivated with atomic-ligands,[32] where similar questions of surface adatom self-assembly and resulting electronic structure need to be addressed.

3.5. Acknowledgement

This work was supported in part by the SONY Corporation. PbS NCs were supplied by Voxtel Nano. The STM instrument used in this work was constructed with support from the U.S. National Science Foundation under Grant DMR-0960211. J.D.H. and G.V.N. acknowledge support from the NSF Center for Sustainable Materials Chemistry, grant CHE-1102637. STM images were processed using WSxM Software.[76]

3.6. Bridge to Chapter IV

In this chapter we continued our exploration of the spatially resolved DOS of annealed, naked, PbS NCs, broadening our observations and discussions of localized electronic states

of the bandgap region beyond the previously discussed conduction band-edge manifold of states. We observed and discussed a variety of sub-bandgap states, including valence band-edge and Fermi-level crossing electronic states, and suggested that these states may arise due to surface reconstruction of surface Pb and S atoms, as well as significant off-stoichiometry Pb and S atom regions at the NC surface. In the next chapter, we will use density functional theory (DFT) to explore more concretely the relationship between NC surface structure, specifically surface reconstruction of the fcc polar (111) surface, and the resultant effect on the DOS of PbS.

CHAPTER IV
IMPACT OF SURFACE RECONSTRUCTION ON THE ELECTRONIC STRUCTURE OF LEAD-SULFIDE: AB INITIO DFT CALCULATIONS

The computational work described in this chapter was conducted by myself, and Hank I. Seeley. Hank conducted the preliminary density functional theory calculations, and initiated some of the analytical code used in the analysis of this work. I conducted further density functional theory calculations, wrote additional analytical code, as well as augmenting the original analytical code written by Hank Seeley, and analysed the theoretical data. I am the primary author of the paper that has not yet been submitted for publication (as of December 2021) and upon which this chapter is based, with assistance and guidance from George V. Nazin.

4.1. Introduction

Lead-chalcogenide (PbX, where X=S, Se or Te) semiconducting nanocrystals (NC), and optoelectronic devices based on thin-films constructed from them, are an active area of research[1-4] due to their unique electronic properties. These materials are particularly appealing for use in the next generation of solar-energy converters because of the tunability of their optical properties, efficient multiple exciton generation[5-10], and potential for extraction of unrelaxed hot carriers[11]. Indeed, the power conversion efficiency of photovoltaic devices constructed from PbX NC thin films has increased rapidly over the course of only a few years, with recent device architecture improving external quantum efficiency values from 8% to 13% in a little over five years.[1, 2, 13] This rapid increase in

device performance has been, in part, the result of a better understanding of the role played by the NC's surface structure in determining the electronic properties of these solids.

Advances in NC device architecture has predominantly come in the form of new surface passivating ligands that encapsulate the NCs, and ligand exchange techniques that allow for the post-synthetic modification of NC ligand shells. The careful selection of ligand types in devices has been shown to enhance charge transport,[3, 4] lower the density of charge trapping states,[5, 6] and produce systematic changes to the electronic band-edge energies of NC thin-films.[7, 8] Another common post-synthesis modification technique used to increase the charge transport in NC thin-films, although less commonly used, is thermal annealing.[9-11] Both of these post-synthesis modification techniques, while necessary for achieving optimal charge transport in the NC films, may radically alter the surface structure and ligand coordination of individual NCs, leading to imperfections in surface passivation or local stoichiometry. Imperfections such as these are thought to result in the appearance of sub-bandgap states in PbX NCs, which can have significant deleterious impact on charge transport, recombination, and extraction in thin-films.[14-16] These sub-bandgap states have been observed in processed NC thin-films via techniques such as photoluminescence;[17-19] deep level transient spectroscopy, thermal admittance spectroscopy, and Fourier transform photocurrent spectroscopy;[20] scanning tunneling spectroscopy;[21-23] and photocurrent measurements on NC-based field-effect transistors.[24] Despite our ability to identify these states in bulk NC-based materials, we still lack a fundamental understanding of their microscopic origin, i.e. their dependence on the structure and chemical composition of individual NCs.

One of the most common approaches used for investigating the electronic structures of NCs is ab initio calculations, such as Density Functional Theory (DFT), applied to model NC systems. In the recent past, DFT studies have found a correlation between sub-bandgap states and PbX NCs with local non-stoichiometry, i.e. deviation from a 1:1 ratio of Pb:X atoms, with excess chalcogen or Pb atoms producing either valence or conduction band derived sub-bandgap states, respectively.[25, 26] Based on these calculations, significant sub-bandgap state density is predicted when NC surfaces are dominated by either Pb or S terminated (111) facets, which can be locally non-stoichiometric. However, despite the insights gained through such theoretical investigations, it is difficult to draw conclusions from such results without confirmation from experiment. Determining the precise origin of NC sub-bandgap states has been, up until recently, nearly impossible, and arises from the fact that there are few experimental techniques capable of probing the electronic structure of individual NCs.

The experimental techniques of scanning tunneling microscopy (STM) and spectroscopy (STS) comprise a unique combination of powerful tools capable of probing the physical, chemical and electronic structure of individual NCs on the atomic scale. Using these techniques, we recently reported on the observation of localized sub-bandgap states on ligand-free PbS NCs (Figure 4.1).[22, 23] The topographic map in figure 4.1a shows a ligand-free PbS NC on a Au(111) substrate, from which we were able to identify specific crystallographic directions, based on the relative orientation of NC surface features and boundaries (white lines). Most of the NCs observed had features aligned along one of three spatial directions forming 120-degree angles suggesting that these NCs were aligned with their (111)-type facets oriented parallel to the Au substrate, as described in the previous

chapters. This preferential NC orientation is likely due to the stabilizing interface formed between PbS(111) and Au(111) surfaces, as a result of the polar nature of the PbS(111) surface.[27] Indeed, the stabilization of PbS (111) surfaces by Au has been observed in electrodeposited PbS on Au(111),[28, 29] and is attributed to the electrostatic screening of the polar PbS surface. In addition, the NCs were found to have width-to-height ratios of 2:1 to 3:1 after annealing, indicating that stabilizing NC-substrate interactions were in fact taking place.

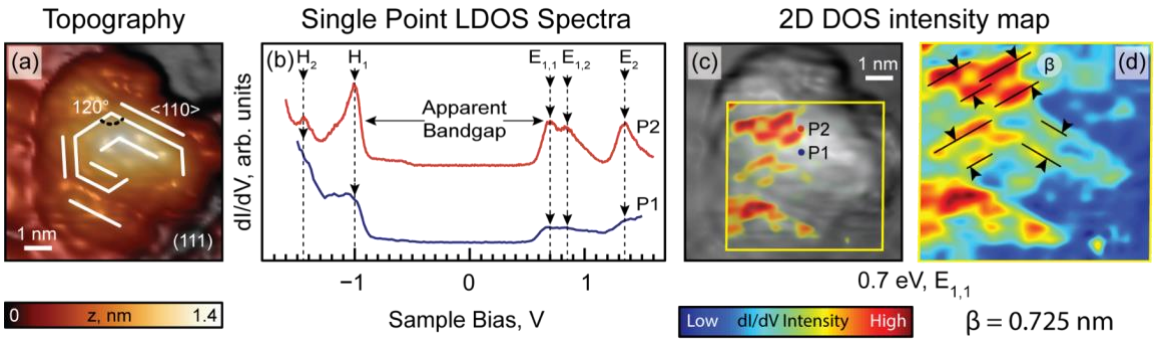

Figure 4.1. Enhanced STM topography of PbS NC with crystallographic features in registry with (111) facet, including features with 120° angles (a). Single point STS showing progression of sub-bandgap states $E_{1,n}$ (b) for points P1 and P2 in (c). Enhanced topography and real space correspondence (c) with single point STS spectra seen in (b) and 2D dI/dV intensity map from (d). Single energy 2D dI/dV intensity map of sub-bandgap state $E_{1,1}$ of PbS NC showing the commensurability of dI/dV intensity features with NC (111) facet topographic features in (a).

Energy- and spatially-dependent DOS data were acquired by conducting differential conductance (dI/dV) STS measurements for individual PbS NCs.[30] Two DOS spectra from a representative NC are shown in figure 4.1b, taken at spatial locations P1 and P2 in figure 4.1c. From these measurements, we found reproducible well-defined peaks, corresponding to occupied (H) or unoccupied (E) electronic states. Significantly, all NCs displayed similar progressions of such states with energetic separations between the $E_{1,1}$ and H_1 states (the

apparent bandgap) of nearly all NCs studied being significantly lower than that expected for PbS NCs of this size. The apparent bandgap of the NC shown in figure 4.1b (~1.7 eV) is near the minimum expected for a PbS quantum well of similar thickness, and significantly smaller than a fully zero-dimensional NC.[31, 32] By contrast, the energy difference measured between the E_2 and H_1 peaks in the STS spectra do fall within the expected energy range for zero dimension PbS NCs. These two observations suggest that the closely spaced $E_{1,n}$ peaks, which were observed in nearly all NCs measured by STS, are likely associated with sub-bandgap states.[22, 23]

To investigate the nature of sub-bandgap states $E_{1,n}$, we recorded thousands of STS spectra encompassing the band-gap region and across a two-dimensional grid covering the spatial extent of the PbS NCs. By compiling the two-dimensional grids of dI/dV spectra for selected bias voltages at the conduction band-edge, we are able to generate energy-dependent, spatially resolved, DOS intensity maps for individual NC states. From the spatial distribution of the $E_{1,1}$ state, at the conduction band edge, of our representative NC (Figure 4.1), we found that the sub-bandgap states are localized in "stripe"-like features on the NC surface. The spatial extent of the "stripe"-like DOS features was compared with atomic features discerned from topographic images of the same NCs and found to align with NC <110> crystal directions and separated by distances of approximately 0.726 nm [stripes are emphasized with black lines in figure 4.1d], thus in keeping with the atomic structure of the (111) facet determined by topographic analysis for the PbS NC surface. The crystallographic orientation and separation of the DOS features, in correlation with the observed topographic features, of the observed NCs are reminiscent of PbSe (111) surface reconstruction features, composed of a half-monolayer of adatoms,[33] with atoms missing

from alternating <110> rows.[34] The reconstructed surface is predicted to result in an energetically stable surface structure – unlike the unstable structures with fully-occupied (111) facets.[34, 35]

In our papers we attribute the formation of sub-bandgap states in the measured NCs to the presence of locally non-stoichiometric, partially terminated, reconstructed (111)Pb surfaces similar to surface structures predicted by recent DFT calculations.[25, 26, 35] This finding is significant, because although the existence of sub-bandgap states in lead chalcogenide NCs is well established,[17-24] and partially terminated (111) surfaces have been experimentally observed,[33, 34] no direct connection between the two has previously been made. In addition, despite the well-known existence of such partially-terminated (111)-type reconstructed surfaces on PbX NCs,[33, 34] their impact on the PbX electronic structure has not been previously reported.

Thus, due to the correlation observed between the topographic, crystallographic, and DOS features of the observed NCs in our,[22, 23] as well as other's research,[26, 33, 34] we proposed that this type of PbX surface reconstruction is responsible for the DOS stripe-like features observed, and furthermore, can be shown to produce sub-bandgap states in PbX NCs. In this chapter, we build on our experimental results by investigating the relationship between surface reconstruction and sub-bandgap states in PbS NCs via ab initio DFT calculations. Specifically, we examine the effect of surface reconstruction of the (111) surface on the PbS electronic structure, and compare it to that of other low energy PbS surfaces, as well as to the bulk PbS electronic structure. The following theoretical results, in conjunction with our previous experimental work, clearly show that such reconstructed

surfaces indeed lead to significant alteration of the PbS electronic structure, and are likely to result in the formation of sub-bandgap states in PbX NCs.

4.2. DFT Theoretical Methods.

Ab initio density functional theory (DFT) calculations were conducted using the Quantum Espresso Software package[36] on idealized model PbS periodic 2-D slab structures with 2 x 1 (111)Pb reconstructed surfaces, similar to model surface reconstruction described by Deringer et al. for DFT simulations of PbS and PbSe surfaces.[35] The absence of Pb or S atoms from the (111) surface along the <110> direction (Figure 4.2a) results in a periodic asymmetry of the PbS lattice, leading to lattice strain,[35] and manifesting as a perturbation to the system. When the perturbation to an otherwise periodic system – i.e. surface reconstruction – is greater in extent than the parent materials Primitive Cell (PC), the PC is no longer an appropriate description of the system and the use of a supercell (SC) to calculate the electronic structure becomes necessary.[12, 37] Idealized slab models rather than finite nanocrystals, which intrinsically contain multiple different crystallographic facets, were used to eliminate the interaction of surface effects from different NC facets and simplify analysis. In addition, the SC slab model approach is widely used for the accurate determination of effects on the physical and electronic structure of semiconductors by surface reconstruction,[34, 35] and a allows for the use of standard basis function methods to solve the Schrödinger equation.[38]

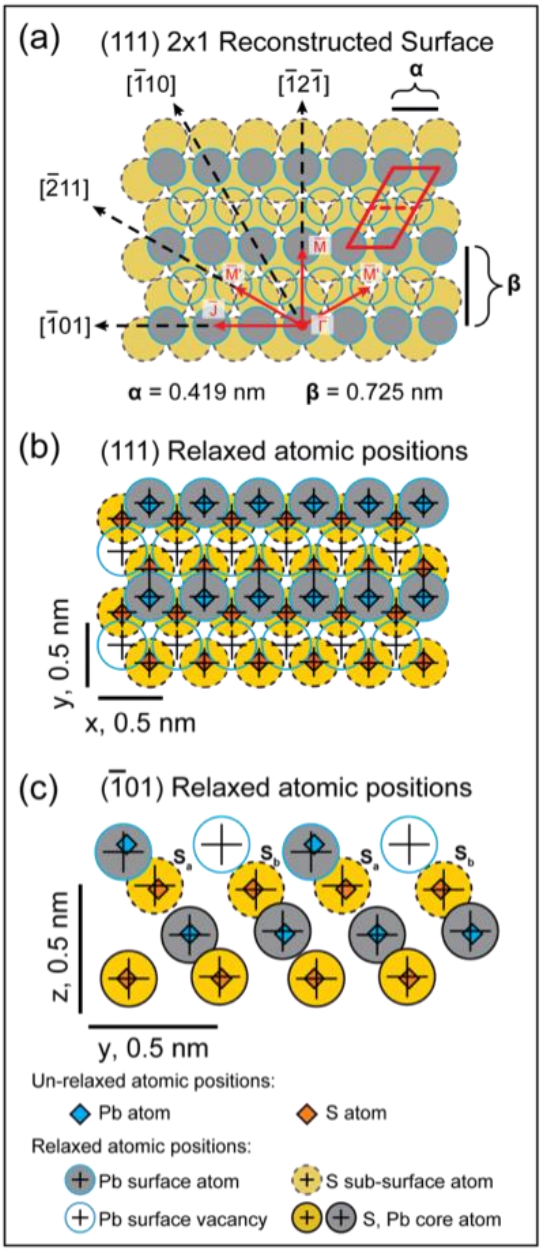

Figure 4.2. Idealized model of a PbS 2x1 reconstructed (111)Pb surface (a), with real space crystallographic directions (black dashed arrows) and corresponding reciprocal space wave-vector directions (red arrows and 1st BZ special point labels). Pb atoms are gray circles with cyan outlines, S atoms are yellow circles with dashed black outlines, Pb surface vacancies transparent with cyan outlines. Subfigure (b) shows a top-down view – (111) facet – of the real space displacement (in x, and y) between unrelaxed and relaxed atomic positions of Idealized model of a PbS 2x1 reconstructed (111)Pb surface seen in (a). Sub-figure (c) is the side view – (101) facet – for the model slab described above, highlighting displacements of slab atoms along the direction normal to the surface facet.

PbX crystals form a face centered cubic (FCC), or "rock salt", crystal structure. The 2 x 1 reconstructed (111) surface SC slab models were constructed using the software package Quantum ATK version 2015.1.[39, 40] Figure 4.2 contains representations of both the un-relaxed (Figure 4.2a), and relaxed (Figure 4.2b,c) 2 x 1 reconstructed (111) surface (Pb variant) structures, and are similar to slab models used by Fang et al.[34] and Deringer et al.[35]

in their treatments of PbX (111) surfaces. The 2 x 1 reconstructed surface is defined here as a half-filled (111) facet with Pb or S vacancies of every other row (inter row distance β = 7.255 Å) extending along the $[\bar{1}10]$ direction. These SC slab models consisted of 12 primitive cells (PC) in a 1 x 2 x 6 (x, y, z) arrangement with 12 S and 12 Pb atoms (to maintain stoichiometry), and a total slab thickness of 2.07 nm. The SC slab models are oriented such that the 2 x 1 reconstructed (111) surface facet is normal to the z-axis. To prevent the formation of a dipole across the 2 x 1 reconstructed (111) slab model, resulting from oppositely terminated Pb and S top and bottom surfaces for (111)Pb and (111)S reconstruction variants, both surfaces were terminated with either Pb or S atoms respectively, with $[\bar{1}01]$ reconstruction rows alternately populated (Figure 4.2a).

The surface energy and electronic structure of the various PbS slab models was calculated using the Perdew-Burke-Ernzerhof (PBE) generalized gradient approximation (GGA)[41] exchange-correlation functional in a plane-wave basis, as utilized in the PWscf package (Quantum Espresso).[42] The cut-off energy for the plane-wave expansion of the wave functions was set to 544.2 eV, core electrons were described by the projector-augmented-wave (PAW) method,[43, 44] and the pseudo potentials used treat Pb 5d orbitals as outer shell (valence) orbitals for this calculation. Spin-orbit coupling was included in all electronic structure calculation because of its previously determined importance in PbX systems.[26, 42, 45] Initially, the Brillouin zone (BZ) of the reconstructed PbS slabs was sampled using a 9x9x1 Monkhorst-Pack k grid, unless otherwise stated.[46] Prior to calculating electronic properties, all slab systems were relaxed until the force on each atom was less than 0.03 eV/angstrom, and the change in energy between two self-consistent steps was less than 1.4 meV. In addition, the bulk-like atoms (at the center of the slab

models) were held at the fixed bulk coordinates during the relaxation step, as calculated for a primitive cell under the applied DFT method.

4.3. Theoretical Modeling Results and Discussion

4.3.1. Slab relaxation calculation; surface energy and Löwdin population analysis.

In our DFT modeling of PbS surfaces, we investigated several different crystallographic facets including the (100), and the 2 x 1 reconstructed (111) surface, these surfaces having been shown to be among the most energetically stable for PbX systems.[35] We calculated the surface energy for two basic types of the 2 x 1 reconstructed (111) surface corresponding to the Pb- and S-terminated variants of the same structure; referred to hereafter as 2 x 1 (111)Pb and (111)S, respectively. Note that only the reconstructed (111)Pb variant of the reconstructions is shown in Figure 4.2a, since the structure of 2 x 1 (111)S is identical prior to relaxation but with the positions of Pb and S atoms interchanged. All slab models were constructed with similar thicknesses (from 2.07 to 2.36 nm, as measured from the centers of surface atoms) so as to disentangle the effects of surface reconstruction from the effects of quantum confinement. We find that the 2 x 1 (111)Pb surface is relatively stable with a surface energy (γ) of 1.83 eV/nm^2—the second lowest energy of all surfaces considered here—and is consistent with previous theoretical results for reconstructed PbX surfaces.[34, 35] In contrast, the 2 x 1 (111)S surface was found to be less stable ($\gamma = 2.27$ eV/nm^2), which further supports the identification of PbS NC surfaces observed in our experiment in the main as belonging to the 2 x 1 (111)Pb type. Indeed, this is consistent with states comprised of mostly Pb atomic orbital character,[26, 47] since the sub-bandgap states observed in our experiment were located above the Fermi level close to the

conduction band-edge, and in is keeping with experimental and theoretical predictions for Pb-rich NC surfaces.[26, 34, 48]

In our analysis of the relaxation of the 2 x 1 (111)Pb SC slab structure significant atomic displacements from bulk atomic positions were observed for individual SC slab atoms, especially at the surface, in agreement with previous reported findings.[35] Pb atoms at the surface relaxed inward towards the center of the slab (Figure 4.2c) by ~0.3 Angstrom, and laterally towards Pb vacancy row. Sulfur atoms of the subsurface (111) facet displayed bimodal relaxation behavior with S_a atoms displaced upward orthogonal to the slab surface facet and towards nearest surface Pb atoms, while S_b atoms were displaced laterally towards the nearest Pb surface reconstruction rows with negligible movement in the normal direction to the slab surface (Figure 4.2b,c). Subsequent Pb and S (111) facets of the SC slab show similar repeating patterns of bimodal relaxation behavior, though to a significantly reduced degree, with correlation of atomic displacement observed along alternating $(0\bar{1}0)$ facets of the SC slab. The atomic displacements observed for Pb surface atoms and sub-surface S atoms makes sense given that atoms on (111) surface facets for an fcc lattice lack three nearest neighbors, and reconstruction leads to missing Pb atoms along every other row in the $[\bar{1}10]$ direction, inhibiting normal charge transfer and bonding for surface Pb atoms and subsurface S atoms as compared to the bulk. Note: the displacement of atoms on and near the bottom surface of the slab mirror the displacements of the atoms on the top surface.

Löwdin population analysis, as implemented by the Quantum Espresso code,[36] was conducted for both relaxed and unrelaxed 2 x 1 (111)Pb SC slabs to observe and understand changes in electron density for atoms on and near the SC slab surface. The compound

semiconductor PbS is traditionally classified as an ionic lattice, with charge transfer from metal Pb atoms to non-metal S atoms, producing Pb^{2+} cations and S^{2-} anions. However, electronegativity differences between Pb and S would suggest that the interaction is not strictly ionic, but rather has significant covalent character. In compound semiconductors such as PbS, where the character of the bonding environment is somewhere between ionic and covalent, the lack of neighboring cations at the surface, and resultant surface reconstruction, has the effect of reducing the Madelung potential, lowering the energy of an electron in the surface cations and producing states split off from the conduction band edge.[49] As seen in Tables 4.1 and 4.2 the Pb and S atoms of the SC slab do not achieve the charge separation of the purely ionic condition, nor should this be expected, and indicates instead only partial charge transfer from Pb to S atoms of the SC slab.[34, 35]

In Table 4.1, for the unrelaxed SC slab, Löwdin population analysis indicates charge separation at the surface, with Pb surface atoms carrying more charge density than Pb atoms of the slab interior, likely a direct result of reduced coordination and bonding at the surface for these atoms (loss of three S nearest neighbors). Sub-surface sulfur atoms S_a and S_b for the unrelaxed slab also show differences in electron density, when compared to each other as well as with slab interior S atoms, resulting from differing coordination environments at the surface, and the loss Pb atom nearest neighbors at the surface.

Table 4.1. Löwdin Charge Analysis for Un-relaxed 2 x 1 (111)Pb SC Slab

Atom #	Atom type	Total Charge	s orbital	p orbital	d orbital
1	Pb	13.5392	1.9274	1.6156	9.9962
2	S	6.4070	1.8201	4.5869	0.0000
3	S	6.4686	1.8424	4.6262	0.0000
4	Pb	13.4705	1.9133	1.5614	9.9959
5	Pb	13.5339	1.9499	1.5869	9.9971
6	S	6.4276	1.7970	4.6306	0.0000
7	S	6.4371	1.8015	4.6356	0.0000
8	Pb	13.5241	1.9372	1.5903	9.9966
9	Pb	13.5086	1.9300	1.5821	9.9965
10	S	6.4353	1.7989	4.6364	0.0000
11	S	6.4340	1.7979	4.6361	0.0000
12	Pb	13.5160	1.9342	1.5853	9.9966
13	Pb	13.5159	1.9342	1.5852	9.9966
14	S	6.4367	1.7991	4.6377	0.0000
15	S	6.4354	1.7980	4.6374	0.0000
16	Pb	13.5252	1.9373	1.5913	9.9966
17	Pb	13.5096	1.9301	1.5830	9.9965
18	S	6.4377	1.8016	4.6361	0.0000
19	S	6.4279	1.7970	4.6309	0.0000
20	Pb	13.4701	1.9133	1.5610	9.9959
21	Pb	13.5339	1.9498	1.5871	9.9971
22	S	6.4067	1.8200	4.5867	0.0000
23	S	6.4669	1.8424	4.6246	0.0000
24	Pb	13.5389	1.9274	1.6154	9.9962

Table 4.2. Löwdin Charge Analysis for Relaxed 2 x 1 (111)Pb SC Slab

Atom #	Atom type	Total Charge	s orbital	p orbital	d orbital
1	Pb	13.5161	1.8821	1.6420	9.9920
2	S	6.4271	1.8000	4.6271	0.0000
3	S	6.4364	1.8006	4.6358	0.0000
4	Pb	13.4829	1.9244	1.5625	9.9959
5	Pb	13.5348	1.9460	1.5922	9.9966
6	S	6.4281	1.7941	4.6340	0.0000
7	S	6.4403	1.7987	4.6416	0.0000
8	Pb	13.5259	1.9358	1.5937	9.9964
9	Pb	13.5043	1.9355	1.5722	9.9966
10	S	6.4400	1.8011	4.6389	0.0000
11	S	6.4286	1.7959	4.6326	0.0000
12	Pb	13.5152	1.9353	1.5833	9.9966
13	Pb	13.5150	1.9353	1.5830	9.9966
14	S	6.4411	1.8010	4.6400	0.0000
15	S	6.4292	1.7959	4.6333	0.0000
16	Pb	13.5268	1.9360	1.5944	9.9964
17	Pb	13.5056	1.9356	1.5734	9.9966
18	S	6.4419	1.7990	4.6429	0.0000
19	S	6.4295	1.7944	4.6351	0.0000
20	Pb	13.4835	1.9245	1.5632	9.9959
21	Pb	13.5351	1.9460	1.5925	9.9966
22	S	6.4273	1.8000	4.6273	0.0000
23	S	6.4364	1.8004	4.6360	0.0000
24	Pb	13.5158	1.8823	1.6415	9.9921

Upon relaxation (Table 4.2) the total charge of Pb surface atoms decreases. In addition, the difference in partial charges for sub-surface S_a and S_b atoms is substantially reduced, indicating increased interaction and coupling, allowing for improved distribution of electron density at the surface. In addition, partial charge distribution increases for valence p atomic orbitals, at the expense of **s** atomic orbitals, on both surface Pb and subsurface S atoms, suggestive of enhanced coupling at the (111)Pb SC slab surface through increased p-orbital overlap. Thus, significant charge separation at the surface in the unrelaxed SC

slab can be said to drive relaxation and displacement of surface atoms for the purpose of improved coupling and charge distribution for atoms in the (111)Pb SC slab surface region.

4.3.2. Electronic structure

4.3.2.1. Super-cell Brillouin Zone (SBZ) band diagram dispersion

Having verified that the formation of the 2 x 1 (111)Pb surface is energetically favorable, and that reconstruction followed by relaxation causes changes to the surface electronic environment as observed in the Löwdin population analysis between the un-relaxed vs. relaxed slabs, we now turn our attention to effects of reconstruction and relaxation on the PbS electronic structure. As a result of the SC model being much larger than the PbS PC, the resultant SBZ is much smaller than the corresponding PBZ, due to the inverse size relationship between real and reciprocal space (*k*-space) vectors. This condition obliges us to accept the inherent folding of the Primitive cell Brillouin Zone (PBZ) along prescribed symmetry directions into a corresponding Supercell Brillouin Zone (SBZ), resulting in the convolution of PBZ electronic bands to form SBZ electronic bands. In addition, the finite thickness of the SC slab model – between 2 to 2.5 nm – essentially collapses all SBZ wave-vectors (*K*) in the x-y plane along the z-axis, effectively producing a two-dimensional band structure where bands along the z-axis demonstrate little if any dispersive character $E(K)$ (i.e. flat band conditions). Thus, for simplicity, we will reference the following descriptions of the SBZ band structure using the Surface SBZ nomenclature, where the reciprocal space (*k*-space) relationships between the 3D- and surface 2D-PBZ, and Surface SBZ can be seen in figure 4.3.

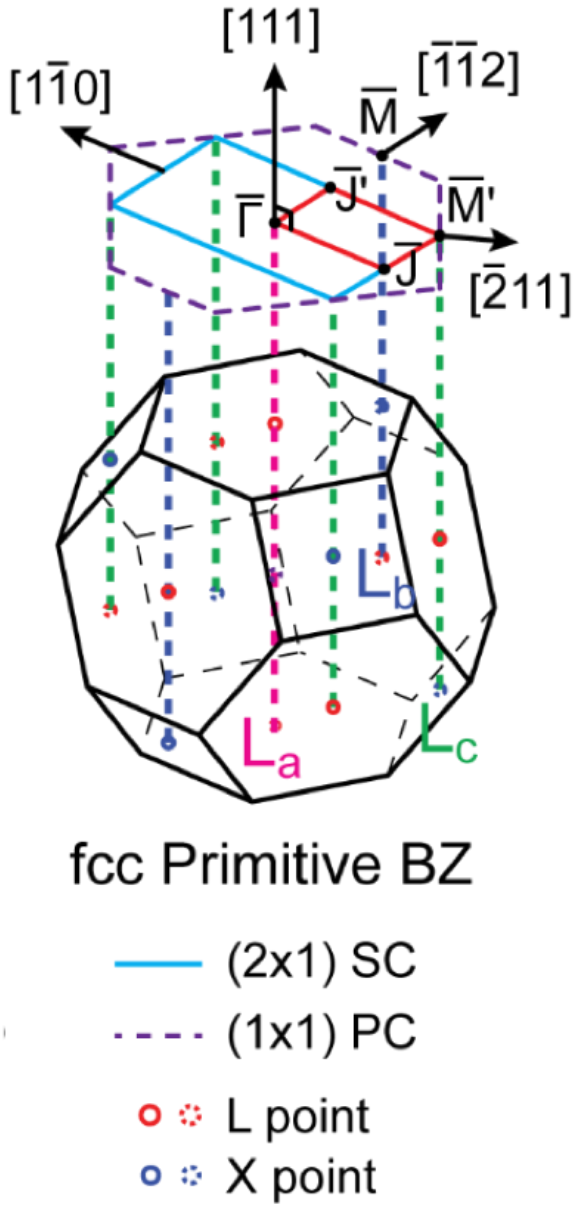

Figure 4.3. Representation of, and reciprocal (k) space relationships between, 3D- and surface 2D-Primitive cell Brillouin Zones (PBZ) and the Super cell Brillouin Zone (SBZ) for the 2 x 1 (111)Pb reconstructed FCC PbS supercell. FCC structure 3D, surface 2D PBZ, and surface SBZ represented in solid black, purple hashmark, and solid cyan lines respectively. Reciprocal space special points labeled for both 3D (L, X special points marked by red, and dark blue circles respectively) and surface 2D (letters with over-bars) representations. The corresponding symmetry point correspondences between different BZ representations indicated with vertical colored (L_a symmetry in pink, L_b symmetry in dark blue, and L_c symmetry in green) hash-marked lines. Corresponding real space crystal directions added for reference.

For the 2 x 1 (111)Pb reconstructed SC slab the $\overline{\Gamma}/\overline{\mathrm{M}}$ and $\overline{\mathrm{M}}'$ symmetry points of the surface SBZ (Figure 4.3) are of prime importance due to their correspondence with the L-points (4-fold degenerate) of the 3D PBZ. The L-points of the 3D PBZ are the special points in the fcc lattice associated with the valence band maximum (VBM) and conduction band minimum (CBM), delineating the bandgap, and define the semiconducting properties, of PbS.[42, 50, 51] In the 2D-PBZ representation, special points labelled $\overline{\mathrm{M}}$ describe all wave-vectors lying along a vertical segment connecting corresponding L- and X-points, including all intervening wave-vectors, of the 3D-PBZ. The 2D-PBZ special point labelled $\overline{\mathrm{M}}$, which includes the $\mathrm{L}_{11\bar{1}}$ symmetry point of the 3D-PBZ and all wave vectors along the L_b segment, is effectively folded into the surface SBZ $\overline{\Gamma}$ point, which includes the L_{111} point of the 3D PBZ, and all wave vectors along the L_a segment producing the special point $\overline{\Gamma}/\overline{\mathrm{M}}$ in the surface SBZ representation. Whereas, the 2-fold degenerate special points labeled $\overline{\mathrm{M}}'$, which separately are composed of the $\mathrm{L}_{1\bar{1}\bar{1}}$ and $\mathrm{L}_{\bar{1}1\bar{1}}$ -points and respective wave-vectors of the 3D-PBZ along the individual L_c segments, of the 2D surface PBZ and 2D-SBZ, remain distinct. Note that $\overline{\mathrm{M}}$ and $\overline{\mathrm{M}}'$ are symmetry equivalent wave-vectors in the non-reconstructed case, and thus degenerate in the 2D surface PBZ representation.

Figures 4.4 through 4.7 show the calculated SBZ band diagrams, with various defined atomic orbital contributions, Pb surface atoms (Figure 4.4), Pb core atoms (Figure 4.5), S subsurface atoms (Figure 4.6), S core atoms (Figure 4.7), for both the unrelaxed and relaxed 2 x 1 (111)Pb reconstructed SC slab models along the specified high symmetry directions (red box in figure 4.3) of the surface SBZ representation. To disentangle the effects of surface reconstruction from structural relaxation SBZ band structures for both unrelaxed (Figures 4.4a – 4.7a) and relaxed (Figures 4.4b – 4.7b) structures are shown.

Somewhat surprisingly, despite the loss of nearest neighbors and reduced coordination (high density of dangling bonds) on the (111)Pb surface, the calculated SBZ band structure for both relaxed and unrelaxed (111)Pb SC structures (Figures 4.4– 4.7) exhibit fairly dispersive $E(\vec{K})$, which would indicate significant mixing of atomic orbitals and thus a relative resilience to the formation of trap states due to electron localization as a result of surface Pb vacancies. We note that, in general, the band dispersion character of both the unrelaxed and relaxed SC structures exhibit many structural similarities, though band energies, especially at SBZ special points, differ markedly. Indeed, for both relaxed and unrelaxed SC slab structures the dispersion character for bands of nominally symmetry equivalent wave vectors $\overline{\Gamma}/\overline{\mathrm{M}}$, and $\overline{\mathrm{M}}'$ are appreciably dissimilar pointing to the highly perturbative effect of 2 x 1 (111)Pb surface reconstruction on the PbS electronic structure. A prime example of this perturbation can be seen in bands C_1 and C_2, the two lowest unoccupied (conduction) bands, for symmetry points $\overline{\Gamma}/\overline{\mathrm{M}}$ and $\overline{\mathrm{M}}'$, which are separated by ~200 meV ($\mathrm{C}_1^{\overline{\Gamma}/\overline{\mathrm{M}}}$ and $\mathrm{C}_2^{\overline{\Gamma}/\overline{\mathrm{M}}}$) and ~ 5 meV ($\mathrm{C}_1^{\overline{\mathrm{M}}'}$ and $\mathrm{C}_2^{\overline{\mathrm{M}}'}$) respectively in the relaxed case, with approximately half the separation at the $\overline{\Gamma}/\overline{\mathrm{M}}$ point in the unrelaxed case. This loss of band degeneracy between bands C_1 and C_2 of the $\overline{\Gamma}/\overline{\mathrm{M}}$ point, as compared to C_1 and C_2 at the $\overline{\mathrm{M}}'$ (in addition to band pairs $\mathrm{C}_3/\mathrm{C}_4$ and $\mathrm{C}_5/\mathrm{C}_6$ higher in the conduction band)[49] is indicative of significant difference in the potential environment at the surface.

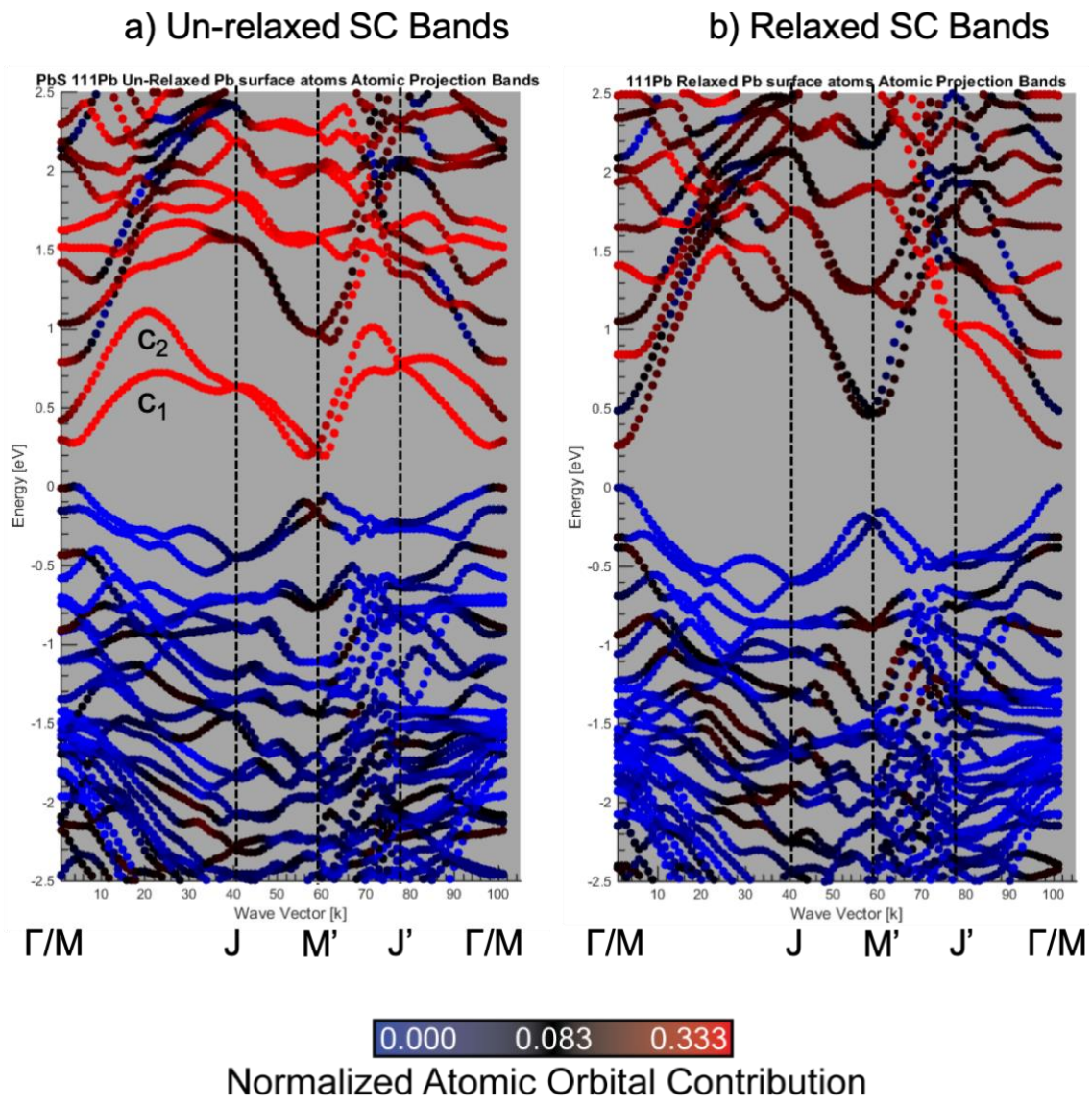

Figure 4.4a. and 4.4b. Surface Pb atom-orbital contribution, dispersion band diagrams for the un-relaxed and relaxed 2 x 1 (111)Pb reconstructed SC, respectively. Red-black-blue colored bands indicate a high-normal-low atomic orbital character contribution for each 2D surface SBZ band for surface Pb atomic orbitals of the SC. Wave-vectors corresponding to special points of the Surface SBZ are indicated with horizontal dashed lines and correspond to wave-vectors along the path of the red box in Figure 4.3.

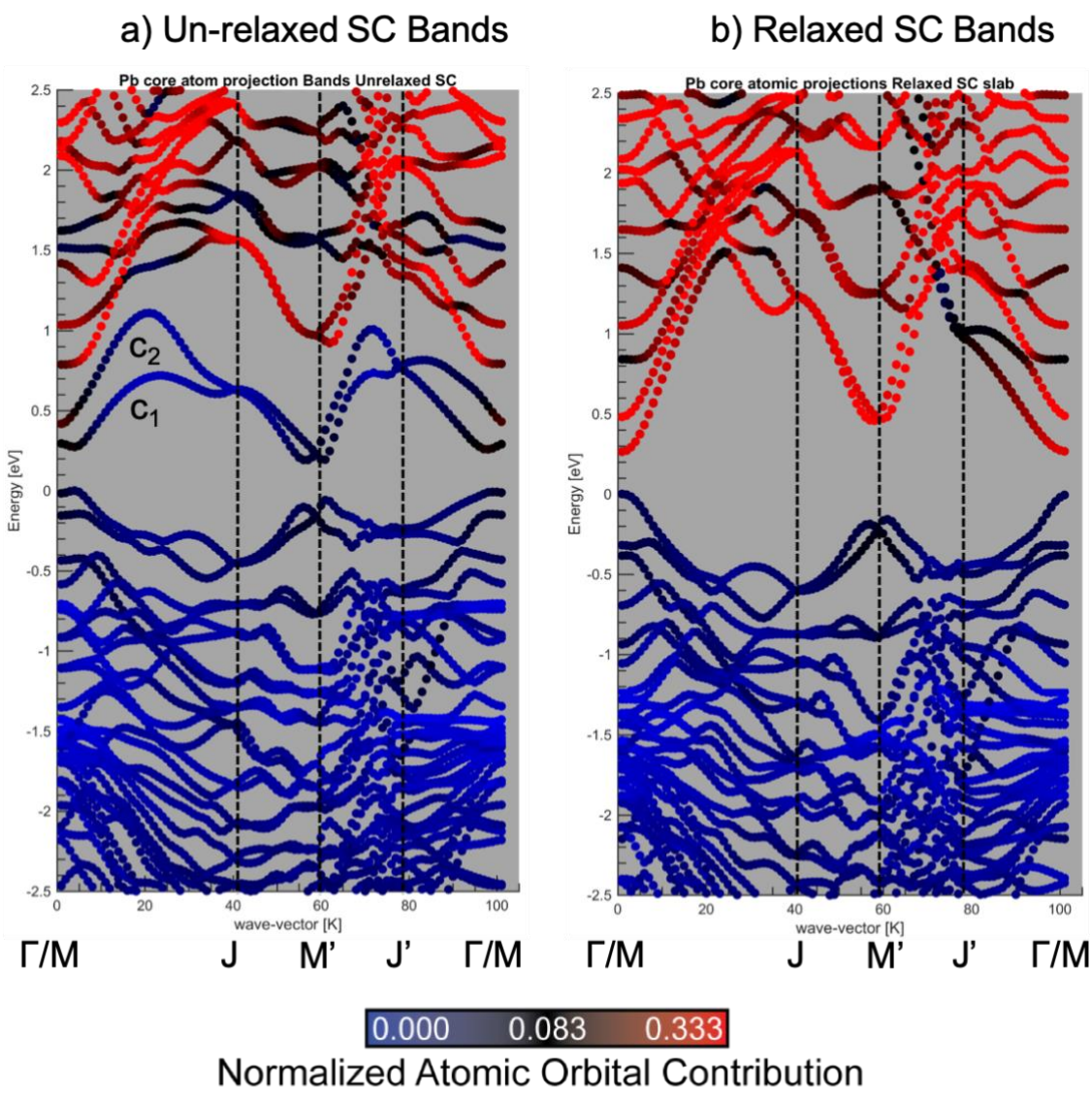

Figure 4.5a and 4.5b Core Pb atom-orbital contribution, dispersion band diagrams for the un-relaxed and relaxed 2 x 1 (111)Pb reconstructed SC, respectively. Red-black-blue colored bands indicate a high-normal-low atomic orbital character contribution for each 2D surface SBZ band for core Pb atomic orbitals of the SC. Wave-vectors corresponding to special points of the Surface SBZ are indicated with horizontal dashed lines and correspond to wave-vectors along the path of the red box in Figure 4.3.

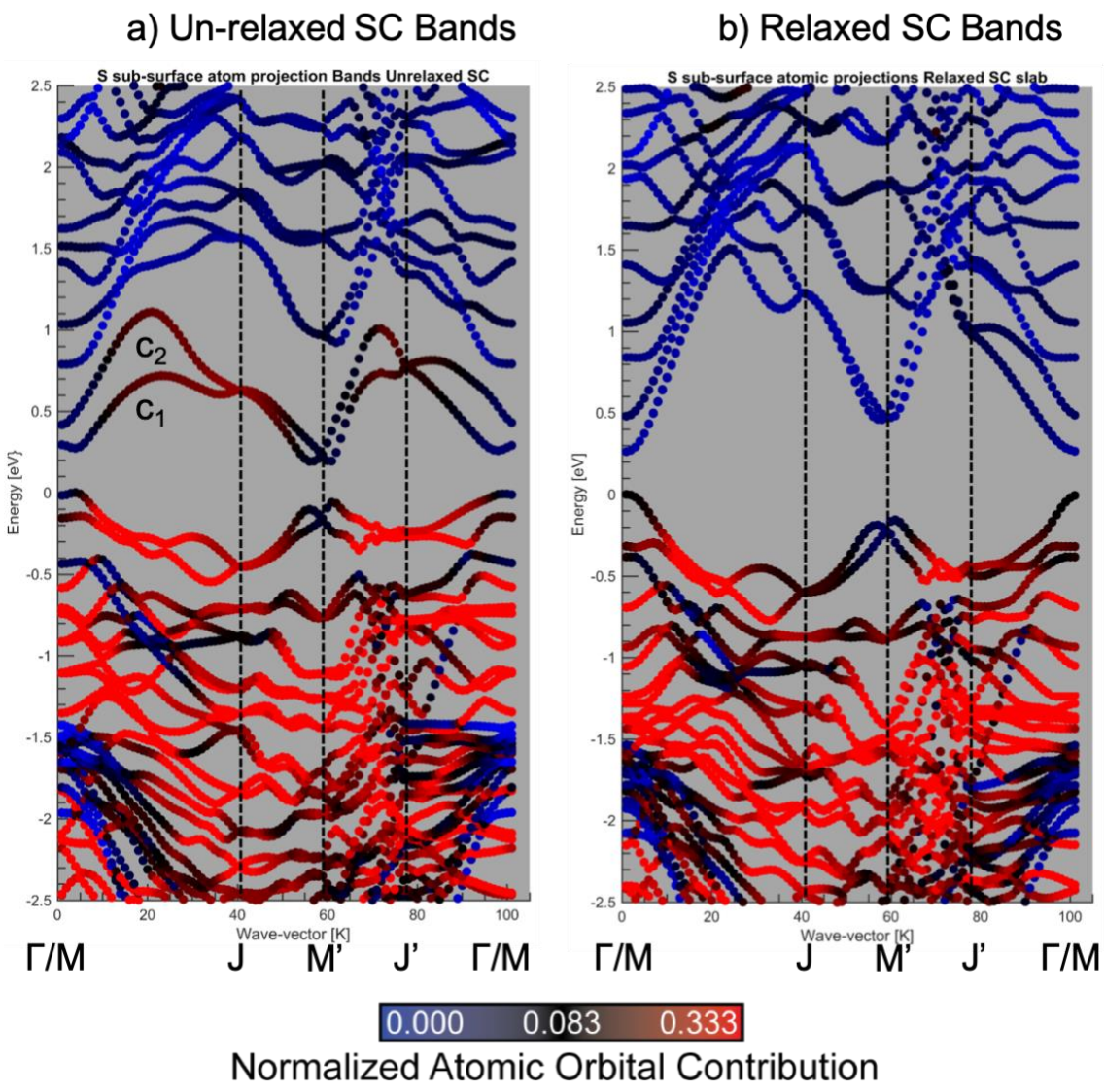

Figure 4.6a and 4.6b Sub-surface S atom-orbital contribution, dispersion band diagrams for the un-relaxed and relaxed 2 x 1 (111)Pb reconstructed SC, respectively. Red-black-blue colored bands indicate a high-normal-low atomic orbital character contribution for each 2D surface SBZ band for subsurface S atomic orbitals of the SC. Wave-vectors corresponding to special points of the Surface SBZ are indicated with horizontal dashed lines and correspond to wave-vectors along the path of the red box in Figure 4.3.

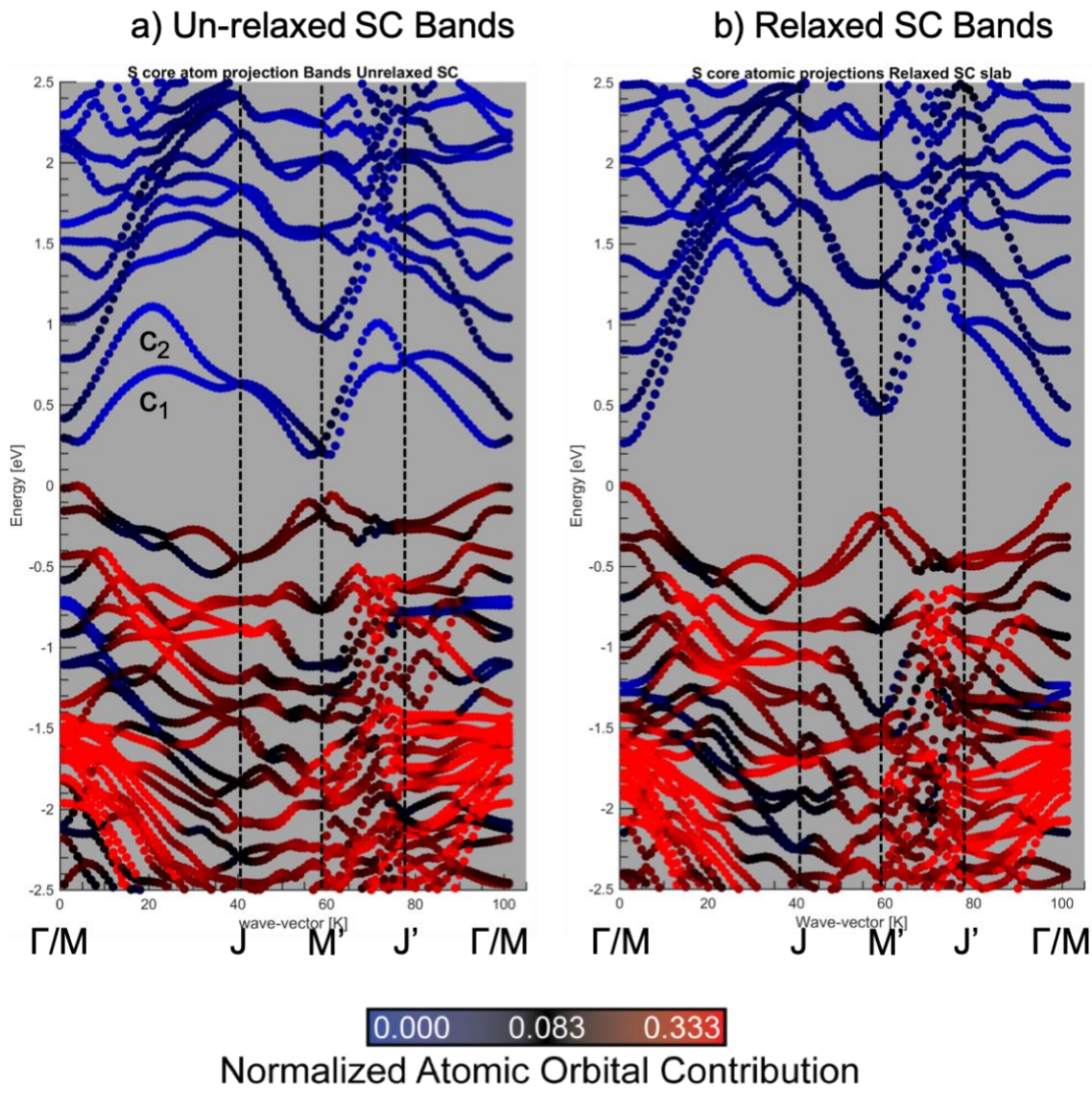

Figure 4.7a and 4.7b Core S atom-orbital contribution, dispersion band diagrams for the un-relaxed and relaxed 2 x 1 (111)Pb reconstructed SC, respectively. Red-black-blue colored bands indicate a high-normal-low atomic orbital character contribution for each 2D surface SBZ band for core S atomic orbitals of the SC. Wave-vectors corresponding to special points of the Surface SBZ are indicated with horizontal dashed lines and correspond to wave-vectors along the path of the red box in Figure 4.3.

Upon relaxation, further perturbative effects on the SC band structure are observed, the most important of which is that the CBM ($C_1^{\overline{\Gamma}/\overline{M}}$) of the relaxed structure is located at the $\overline{\Gamma}/\overline{M}$-point, while $C_1^{\overline{M}'}$ lies ~200 meV higher at the $\overline{M}'$-point, whereas the CBM for the un-relaxed structure is located at the $\overline{M}'$-point. In addition, a comparison of the energy difference between the highest occupied V_1 and lowest unoccupied C_1 bands for the $\overline{\Gamma}/\overline{M}$ and $\overline{M}'$ points of the relaxed structure show significant disparities, with V_1 - C_1 differences of 0.26 eV and 0.68 eV, respectively. Indeed, the highest occupied band of the $\overline{M}'$ symmetry $V_1^{\overline{M}'}$ is significantly depressed in energy as compared to that of the $\overline{\Gamma}/\overline{M}$ symmetry $V_1^{\overline{\Gamma}/\overline{M}}$, a difference of 0.22 eV. An effect of relaxation thus is the lowering in energy of $\overline{\Gamma}/\overline{M}$ CB states over that of the $\overline{M}'$ CB states, as well as all VB states for both symmetry points. These significant differences in band dispersion character, and loss of band degeneracy, between the $\overline{\Gamma}/\overline{M}$ and $\overline{M}'$ points for both the unrelaxed and relaxed SC slab result from the surface atomic anisotropy (i.e. surface reconstruction) of the system, and indicate the perturbed nature of the electronic environment, i.e. potential, at the surface as compared to the slab interior.

Analysis of surface Pb atom d-band states at the $\overline{\Gamma}/\overline{M}$ point (Figure 4.8), for unrelaxed and relaxed structures, further supports the contention that these atoms are in a different electronic environment as compared to atoms of the slab interior. Pb d-orbitals for both relaxed and unrelaxed SC structures are relatively unmixed, apart from other Pb d-orbitals, as compared to significant mixing of S/Pb s and p atomic orbitals of higher bands, and constitute the lowest valance band states, isolated deep in the electronic structure of the PbS (111)Pb SC slab. As a result of loss of nearest neighbors, reconstruction, and

relaxation, the valence states of surface Pb atoms will be significantly more affected by changes in the electronic environment at the SC slab surface, than will their counterparts in the slab interior. In figure 4.8 surface Pb d-states exhibit the lowest energies of all Pb d-states, for both relaxed and unrelaxed cases, by 100 and 600 meV respectively, evidence of their isolation and indicative of the potential difference for surface Pb atoms as compared with that of atoms elsewhere in the SC slab. The difference in energy for surface Pb atom d-states between the unrelaxed and relaxed case results from the relaxation of surface Pb atoms towards sub-surface S atoms (Figure 4.2), the electrons in d-orbitals of the Pb surface atoms overall potential changes as a result of their proximity to sub-surface S atoms, reducing their isolation, increasing electronic interactions, leading to an overall increase in energies of the electrons in these states. Despite the increase in Pb d-orbital energies upon relaxation, the surface Pb atom potential environment remains dissimilar enough, as compared with that of the slab interior Pb d-states. This difference in the electronic environment of the surface, compared to the slab interior, will have important consequences for the band-edge states of the PbS SC slab.

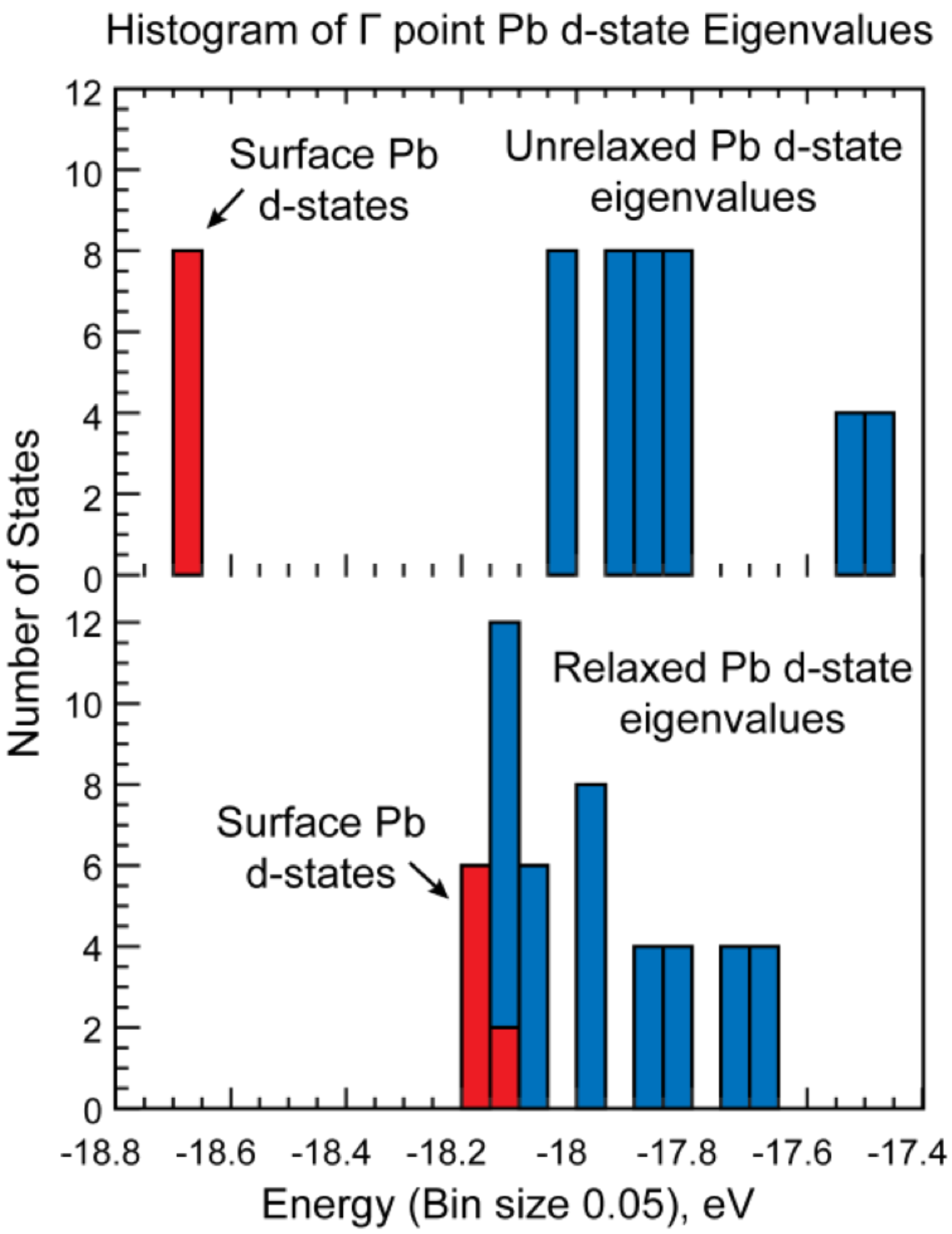

Figure 4.8 Histograms for the gamma point Pb d-state eigenvalues of the un-relaxed (top), relaxed (bottom) 2 x 1 (111)Pb reconstructed PbS SC. Surface(core) Pb d-state eigenvalues are highlighted in red(blue).

4.3.2.2. Atomic orbital projection onto SBZ bands

Given that surface localization is a defining characteristic of sub-band gap states in our experimental STM studies of PbS NCs,[22, 52] ascertaining the spatial distribution of atomic orbital contribution for specific atoms of the SC lattice, i.e. surface Pb atoms, to the band-edge states should provide important insights into the likely origin of sub-bandgap states in PbS NCs. The amount of atomic orbital character associated with each band of the (111)Pb SC slab model was determined by the projection of SC wavefunctions onto atomic wavefunctions using the Quantum Espresso post processing project.x code.[36] Custom MATLAB code (MATLAB version 2016b) was used to extract, process, and display the atomic orbital projection data produced by the QE output, for a given atom or set of atoms of the SC slab, and is visualized in figures 4.4–4.7 through the use of a blue-black-red color gradient scheme applied to the SC bands. The overall atomic orbital contribution from a specific SC slab atom(s) was determined by adding the atomic orbital contribution from the specified atom(s) for a particular state and normalizing by all contributions to the state for all of the atoms in the SC slab. For example, atomic orbital contributions from Pb surface atoms (two atoms, one from the top and bottom surfaces of the SC slab, out of twenty-four total atoms in the SC slab model, twelve Pb and twelve S atoms) totaling more than 0.083 (or $1/12^{th}$) of the total normalized contribution to any particular state are described as over-contributing to that state. Thus, the extent to which any state would be characterized as "localized at the surface" would be supported, in part, by the over-contribution (gray – red highlighting) by surface Pb atoms as derived from atomic orbital projection.

Not surprisingly, our findings indicate that the conduction(valence) band-edge states are primarily derived from Pb(S) atomic orbitals (Figures 4.4–4.7), a finding which is well documented in many DFT studies of PbS and lead chalcogenide salts in general.[26, 47, 50] What is notable here is the sizeable difference in contribution to band-edge states from surface, sub-surface, and slab-interior atoms, and the marked change in atomic orbital contribution upon relaxation of the SC structure. Atomic orbital projections for both unrelaxed and relaxed (111)Pb SC structures (Figure 4.4a and 4.4b) show moderate to high surface Pb atomic-orbital contribution to conduction band-edge states (C_1 and C_2), especially at the $\overline{\Gamma}/\overline{M}$ and $\overline{M}'$ points of the surface SBZ. In general, the decrease in atomic orbital contribution to the conduction band-edge upon relaxation, especially for bands C_1 and C_2 in general, and at the $\overline{M}'$ points specifically, is dramatic and further highlights the electronic isolation of surface Pb atoms prior to relaxation, as seen in Löwdin population analysis (Tables 1 and 2). Concurrently, the overall reduction in surface Pb character for conduction bands C_1 and C_2 upon relaxation, especially at the $\overline{M}'$ points, is offset by an equally striking increase in core Pb character for the same bands (Figure 4.5a and 4.5b). The considerable overall reduction in surface Pb character for conduction bands of the relaxed SC slab is countered by significant increases in surface Pb character for the first three odd numbered conduction band states at the $\overline{\Gamma}/\overline{M}$ point ($C_1^{\overline{\Gamma}/\overline{M}}$, $C_3^{\overline{\Gamma}/\overline{M}}$, $C_5^{\overline{\Gamma}/\overline{M}}$), where the surface Pb contribution remains high ($C_1^{\overline{\Gamma}/\overline{M}}$) or even increases ($C_3^{\overline{\Gamma}/\overline{M}}$, $C_5^{\overline{\Gamma}/\overline{M}}$), in contrast to even numbered band states at the $\overline{\Gamma}/\overline{M}$ point ($C_2^{\overline{\Gamma}/\overline{M}}$, $C_4^{\overline{\Gamma}/\overline{M}}$, $C_6^{\overline{\Gamma}/\overline{M}}$) that lose surface Pb character. In addition, the increased surface Pb atomic orbital character of odd conduction bands at the $\overline{\Gamma}/\overline{M}$ point ($C_1^{\overline{\Gamma}/\overline{M}}$, $C_3^{\overline{\Gamma}/\overline{M}}$, $C_5^{\overline{\Gamma}/\overline{M}}$) for the relaxed SC are lower in energy relative

to even numbered bands ($C_2^{\overline{\Gamma}/\overline{M}}$, $C_4^{\overline{\Gamma}/\overline{M}}$, $C_6^{\overline{\Gamma}/\overline{M}}$) that exhibit increased interior Pb atom contribution at the $\overline{\Gamma}/\overline{M}$ point. This bimodal behavior, with respect to surface Pb character, exhibited by the first six bands at the $\overline{\Gamma}/\overline{M}$ point with odd band surface Pb character increasing more significantly over that of even bands, is striking and will be further elucidated by probability density visualization of these states later in this chapter.

As with dispersion character, the surface Pb atomic orbital contribution to $\overline{M}'$ point states of the conduction band differs considerably with that of the $\overline{\Gamma}/\overline{M}$ point, as might be expected. $\overline{M}'$ point states at the conduction band-edge exhibit considerable surface Pb contribution prior to relaxation. Upon relaxation however, conduction band states of the $\overline{M}'$ point lose considerable surface Pb character (Figure 4.4b), compared to the $\overline{\Gamma}/\overline{M}$ point. In addition, each band pair for bands $C_1^{\overline{M}'}$ through $C_6^{\overline{M}'}$ at the $\overline{M}'$ point exhibit essentially equivalent surface Pb character, in contrast to equivalent band pairs of the $\overline{\Gamma}/\overline{M}$ point, where the first band pair $C_1^{\overline{M}'}$ & $C_2^{\overline{M}'}$ exhibits equivalent contribution from both surface and slab interior Pb atoms while subsequent band pairs $C_3^{\overline{M}'}$ & $C_4^{\overline{M}'}$ and $C_5^{\overline{M}'}$ & $C_6^{\overline{M}'}$ show increasing surface Pb contribution though much less than is observed at the $\overline{\Gamma}/\overline{M}$ point. Thus, disparities in the spatial distribution of atomic orbital contribution reinforce observations of differences in the band dispersion characteristics of the 2D SBZ at the $\overline{\Gamma}/\overline{M}$ and $\overline{M}'$ points, underlining the profound effect of surface reconstruction and surface atomic anisotropy on the electronic structure of the 2 x 1 (111)Pb reconstructed SC slab.

As noted above, and as seen in figures 4.6 and 4.7, S atomic orbital contribution predominates the valence band in general, and at the valence band-edge. Interestingly however, prior to relaxation there is considerable mixing of sub-surface S and surface Pb

atomic orbitals in the frontier bands, with significant Pb(S) contributions to valence(conduction) band-edge bands. Indeed, states $V_1^{\overline{\Gamma}/\overline{M}}$ and $V_3^{\overline{\Gamma}/\overline{M}}$ of the $\overline{\Gamma}/\overline{M}$ point and $V_1^{\overline{M}'}$ & $V_2^{\overline{M}'}$ of the $\overline{M}'$ point have significant surface Pb character contribution as seen in figure 4.4a. In addition, conduction bands C_1 and C_2 for the un-relaxed slab have above average sub-surface S atomic orbital contribution in general (Figure 4.6a), though not at the $\overline{\Gamma}/\overline{M}$ or $\overline{M}'$ points specifically.

Following relaxation, sub-surface S atoms show below average contribution to conduction C_1 and C_2 bands (Figure 4.6b), in contrast to the substantial increase in core Pb contribution previously noted (Figure 4.5b), especially at the $\overline{\Gamma}/\overline{M}$ and $\overline{M}'$ points. In addition, surface Pb atomic orbital contribution to states $V_1^{\overline{\Gamma}/\overline{M}}$, $V_3^{\overline{\Gamma}/\overline{M}}$, $V_1^{\overline{M}'}$ and $V_2^{\overline{M}'}$is considerably diminished (Figure 4.4b), showing substantially below average contribution. Thus, we can say that surface reconstruction for the (111)Pb PbS surface does have a profound effect on the electronic structure of PbS, most especially on the band-edge states of the primary band gap. However, relaxation of the (111)Pb surface would appear to be as important given the significant impact it has on the contribution of atomic orbitals to the frontier states, especially at the $\overline{\Gamma}/\overline{M}$ or $\overline{M}'$ points, defining the fundamental band gap and determining the electronic properties of (111)Pb PbS.

4.3.2.3. Projected Density of States

To further delineate the outsized affect surface Pb atoms have on the conduction band-edge states the average Projected Density of States (PDOS) for surface and core, Pb and S atoms are compared with that of the Total Density of States (TDOS) for the SC slab, as seen in Figure 4.9. As with atomic orbital projection contribution, the PDOS for specified

atoms is normalized with respect to the TDOS. The average surface Pb PDOS (red curve in figure 4.9a) lying above that of the TDOS (black curve figure 4.9a) and average core Pb

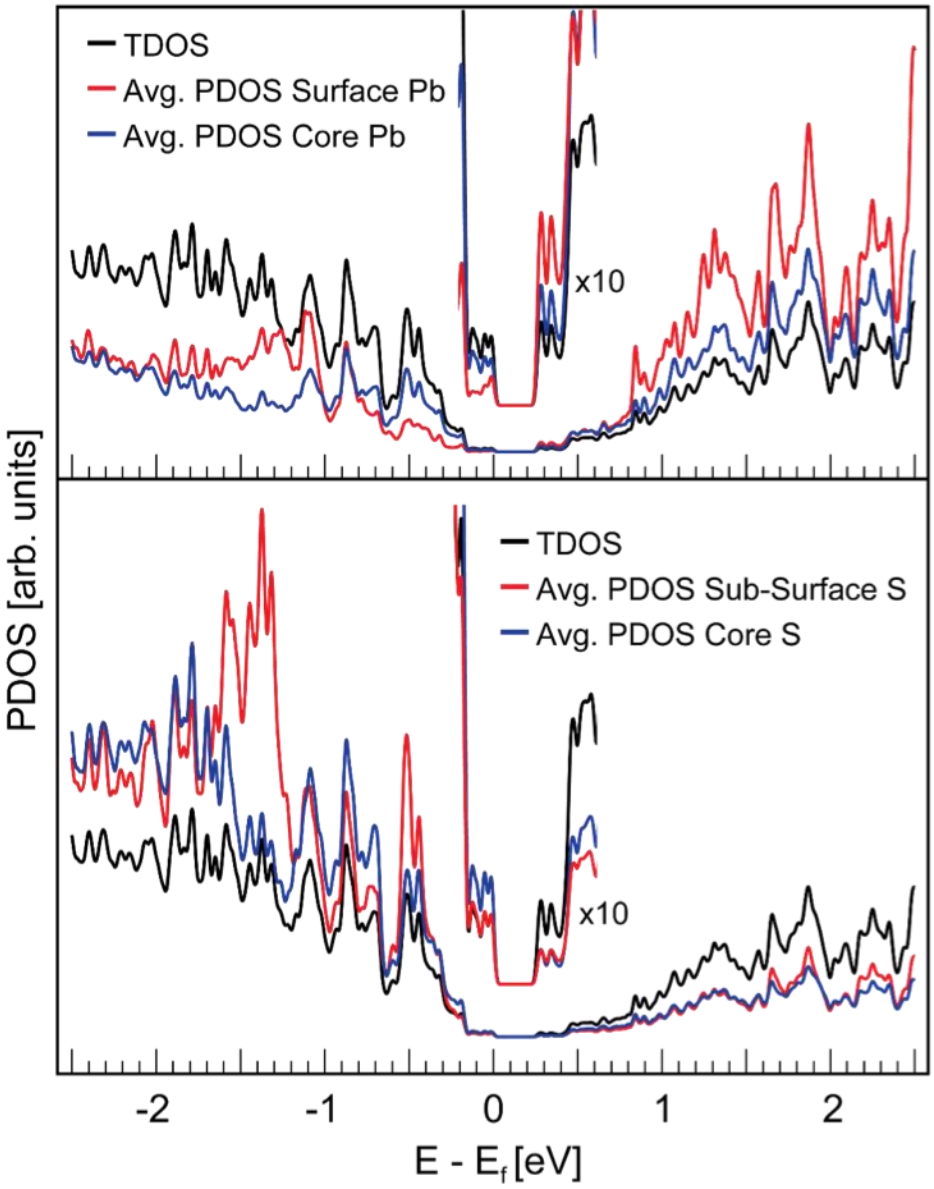

Figure 4.9 Projected Density of States (PDOS) vs. Total Density of States (TDOS) for specified atoms of the 2 x 1 (111)Pb reconstructed SC. Inset PDOS and TDOS curves centered on the band-gap region, for specified atoms, increased by a factor of ten for clarity.

PDOS (blue curve in figure 4.9a) indicates the outsized contribution of Pb surface atoms to the conduction band-edge states. In contrast, the PDOS (red and blue curves figure 4.9b) of sub-surface and core S atom indicate significantly below average contributions to conduction band-edge states, further supporting that these states are surface localized and derived predominately from Pb atoms, especially surface Pb atoms.

4.3.3. Electron probability density cross-sections

In the previous sections we delineated the individual, and collective, effects of surface reconstruction and relaxation with changes observed in the (111)Pb SC slab band structure, with respect to band dispersion, atomic orbital projection character, and surface Pb d-state energies, resulting in a significantly altered electronic environment at the SC slab surface, as compared to the slab interior. In this section we describe the effects of surface reconstruction and relaxation on the spatial distribution of electronic states (electron probability density) of the (111)Pb SC slab, and the correlation of these results with surface states described in the literature, specifically Tamm surface states. Complementary 2D electron probability density $|\Psi(r)|^2$ cross-sections of the un-relaxed and relaxed (111)Pb SC slab structures for states (wave-vectors ($\vec{K}$)) of the $\overline{\Gamma}/\overline{\mathrm{M}}$ ($\Gamma/L_a/L_b$) (Figures 4.10, 4.11, 4.14, 4.15) and $\overline{\mathrm{M}}'$ (L_c) (Figures 4.12, and 4.13) points are shown, along with corresponding S and Pb atoms in their relaxed(unrelaxed) lattice positions. Significantly, though not surprisingly, the electron probability density of the $\overline{\Gamma}/\overline{\mathrm{M}}$ ($\Gamma/L_a/L_b$) and $\overline{\mathrm{M}}'$ (L_c) states differ considerably in their individual geometries and amount of surface localization for both un-relaxed and relaxed conditions. The 2D electron density cross-sections shown in figures 4.10 through 4.13 cutting along $[0\bar{1}0]$ facets, and figures 4.14 and 4.15 cutting

along a $[10\bar{1}]$ facet, of the SC slab were chosen specifically because they highlight not only the surface localized probability density associated with Pb surface atoms but also the direction, orientation, and atomic correspondence, of increased probability density coupling Pb atoms at the surface with Pb atoms of the slab interior. It can be seen from inset crystal diagrams (Figures 4.10–4.13), that $[0\bar{1}0]$ facets cut along the (111)Pb surface reconstruction rows, forming an alternating pattern between surface reconstruction rows on the top and bottom surfaces of the (111)Pb SC slab (This alternating pattern is, at least for these calculations, somewhat artificial, resulting from the idealized slab model preparation method used for this computational analysis, which has been used previously[34]). In contrast, $[10\bar{1}]$ facets slices bisect Pb surface reconstruction rows (Figures 4.14–4.15). Prior to relaxation, all conduction band-edge states, as well as valence states $V_1^{\overline{\Gamma}/\overline{M}}$, $V_3^{\overline{\Gamma}/\overline{M}}$ (Figure 4.10), $V_1^{\overline{M}\prime}$ and $V_2^{\overline{M}\prime}$ (Figure 4.12) exhibit moderate to significant probability density associated with Pb surface atoms, in agreement with atomic projection character data described in the previous section (Figure 4.4a). In general, the probability density for $\overline{\Gamma}/\overline{M}$ ($\Gamma/L_a/L_b$) states displays mostly atomic p-orbital character for both S and Pb atoms oriented roughly orthogonal to the SC slab surface, in keeping with expectations of atomic orbital contributions to band edge states. Interestingly, the increased density observed on surface Pb atoms does not remain localized at the surface, but can be seen to couple with Pb atoms of the slab interior especially for unrelaxed states $V_1^{\overline{\Gamma}/\overline{M}}$, $V_3^{\overline{\Gamma}/\overline{M}}$, and $C_1^{\overline{\Gamma}/\overline{M}}$ through $C_4^{\overline{\Gamma}/\overline{M}}$(Figures 4.10, and 4.14).

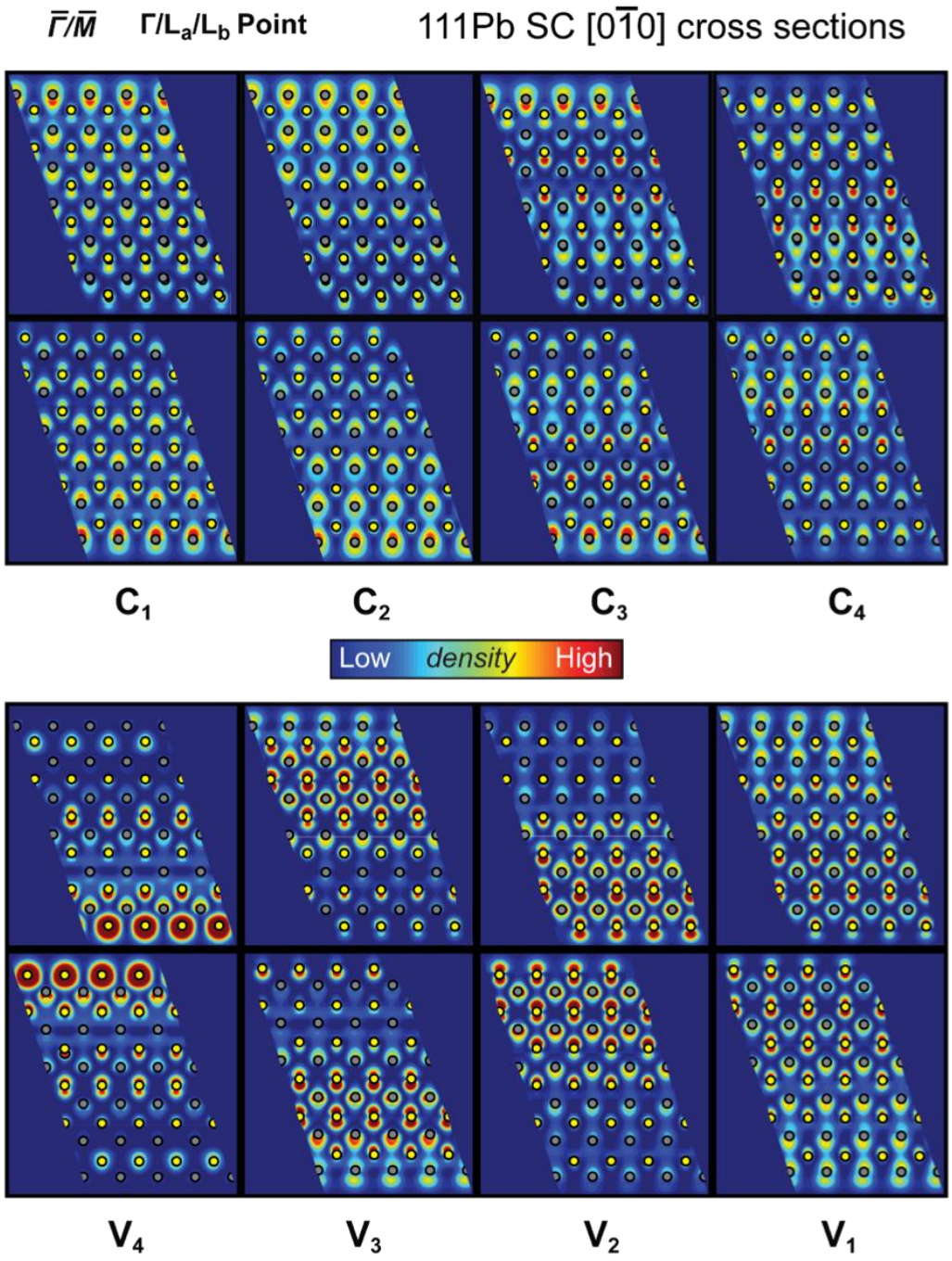

Figure 4.10 Electron density cross-sections of the $\bar{\Gamma}/\bar{M}$ ($\Gamma/L_a/L_b$) point along [0$\bar{1}$0] facets (red/green planes - top/bottom Pb rows inset crystal image at right) for the 2 x 1 (111)Pb reconstructed SC slab before relaxation. Corresponding S (yellow) and Pb (gray) atoms in their unrelaxed lattice positions shown for clarity. Electron density denoted by inset color gradient, with red(blue) indicating high(low) electron density.

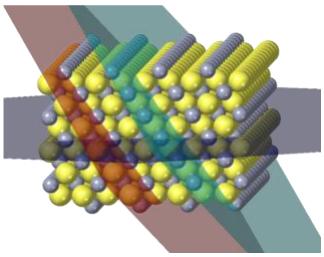

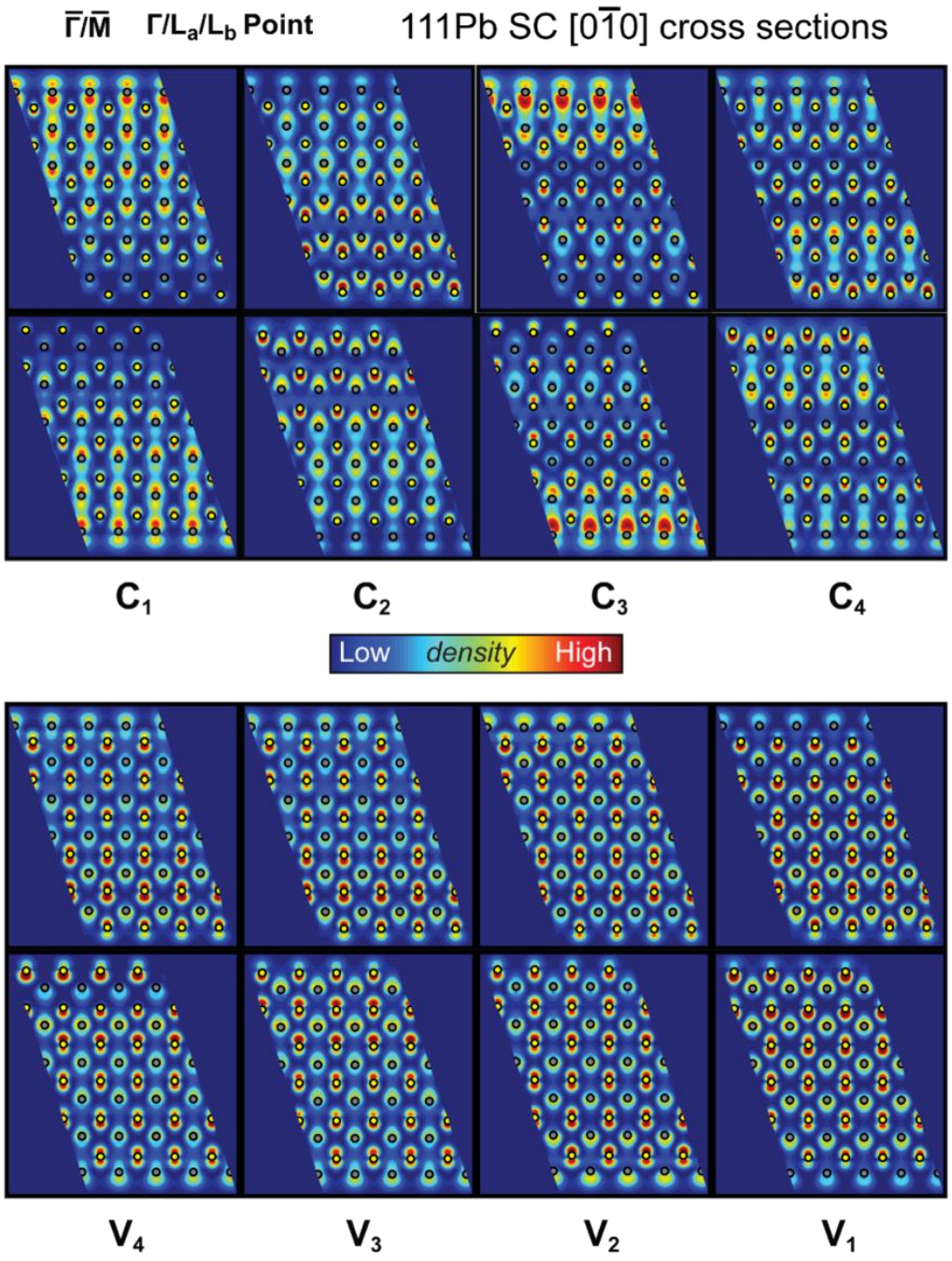

Figure 4.11 Electron density cross-sections of the $\bar{\Gamma}/\bar{M}$ ($\Gamma/L_a/L_b$) point along [$0\bar{1}0$] facets (red/green planes - top/bottom Pb rows inset crystal image at right) for the 2 x 1 (111)Pb reconstructed SC slab after relaxation. Corresponding S (yellow) and Pb (gray) atoms in their relaxed lattice positions are shown for clarity. Electron density denoted by inset color gradient, with red(blue) indicating high(low) electron density.

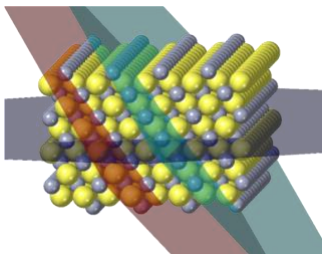

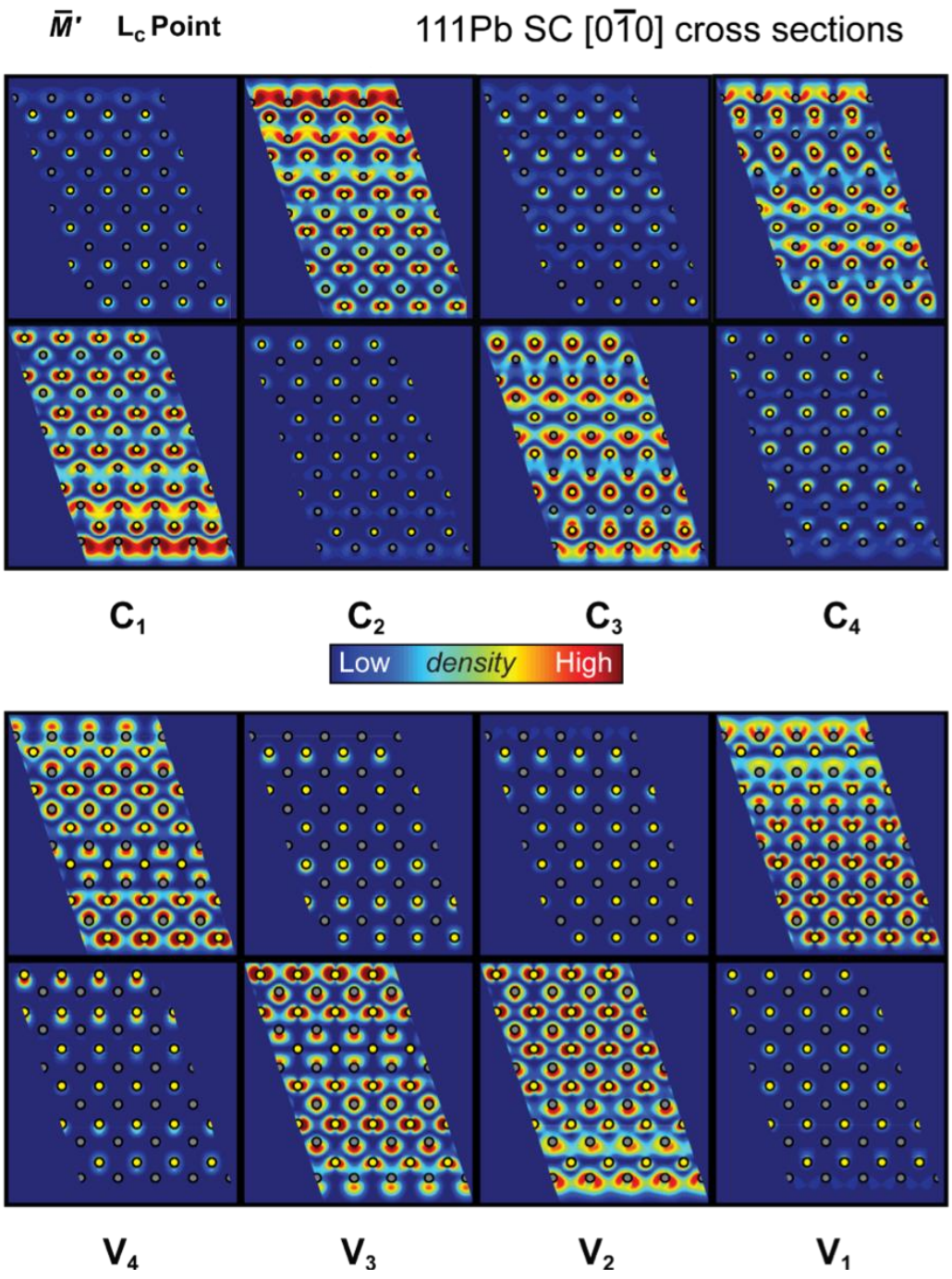

Figure 4.12 Electron density cross-sections of the $\overline{M}'$ (L_c) point along [0$\bar{1}$0] facets (red/green planes - top/bottom Pb rows inset crystal image at right) for the 2 x 1 (111)Pb reconstructed SC slab before relaxation. Corresponding S (yellow) and Pb (gray) atoms in their unrelaxed lattice positions shown for clarity. Electron density denoted by inset color gradient, with red(blue) indicating high(low) electron density.

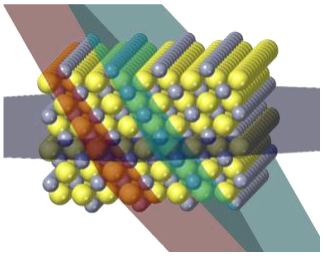

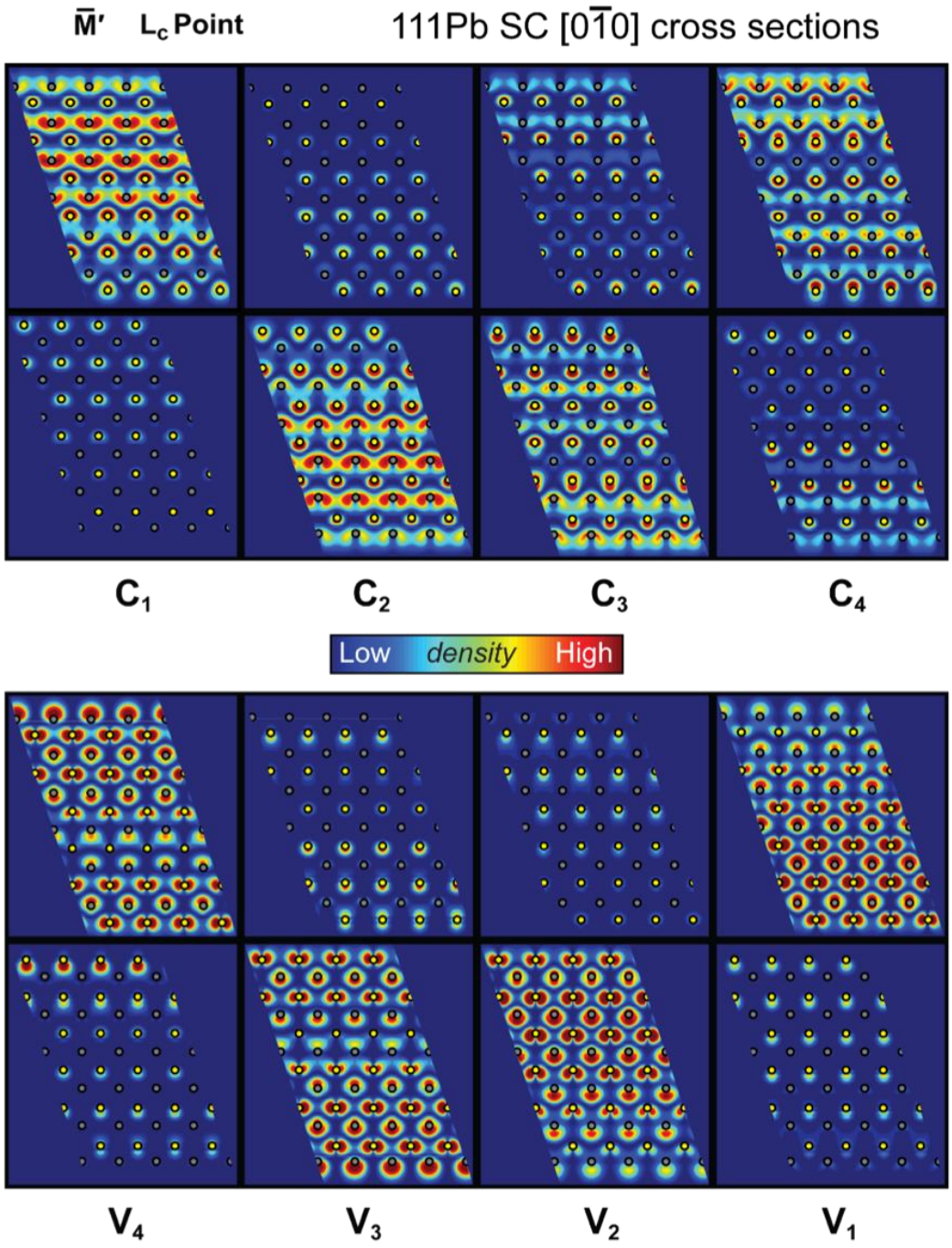

Figure 4.13 Electron density cross-sections of the $\overline{M}'$ (L_c) point along [0$\bar{1}$0] facets (red/green planes - top/bottom Pb rows inset crystal image at right) for the 2 x 1 (111)Pb reconstructed SC slab after relaxation. Corresponding S (yellow) and Pb (gray) atoms in their relaxed lattice positions shown for clarity. Electron density denoted by inset color gradient, with red(blue) indicating high(low) electron density.

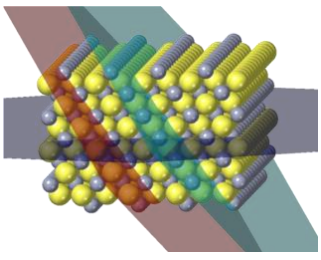

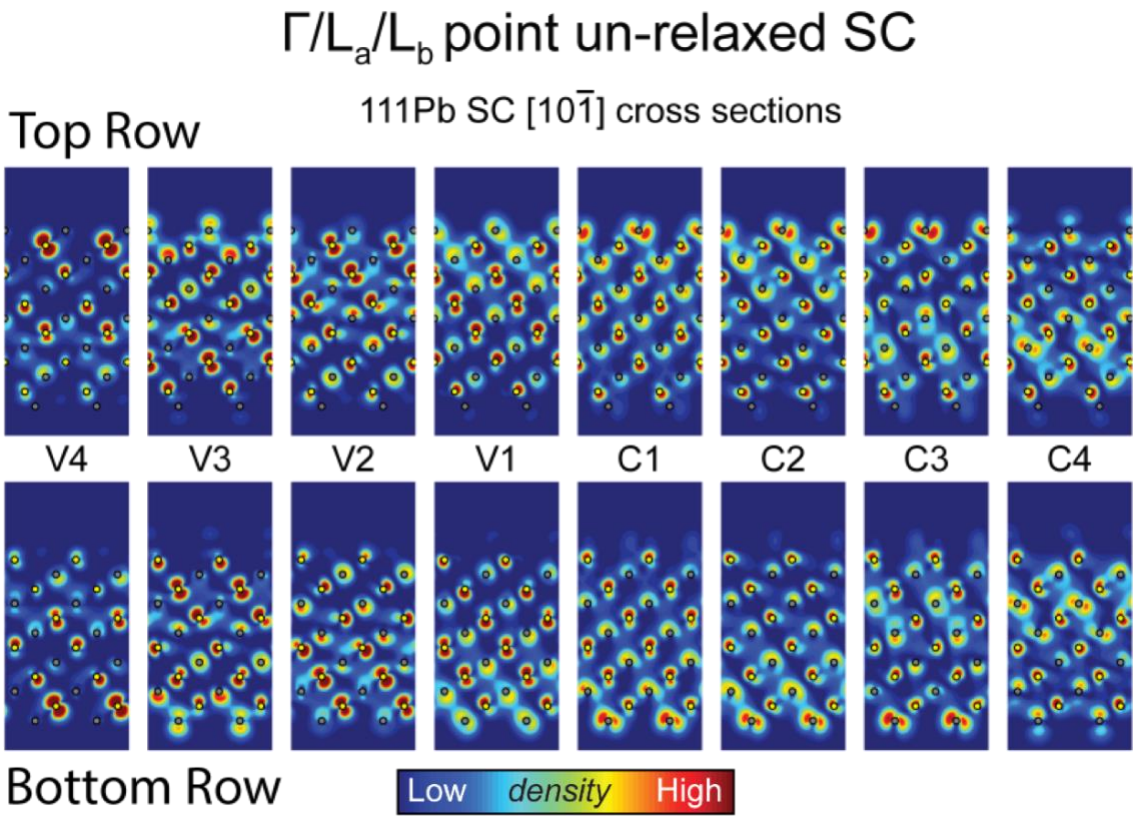

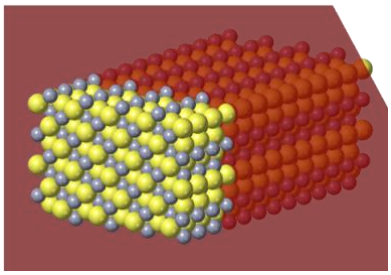

Figure 4.14 Electron density cross-sections of the $\overline{\Gamma}/\overline{M}$ ($\Gamma/L_a/L_b$) point along $[10\bar{1}]$ facets (red plane inset crystal image at right) for the 2 x 1 (111)Pb reconstructed SC slab before relaxation. Corresponding S (yellow) and Pb (gray) atoms in their unrelaxed lattice positions are shown for clarity. Electron density denoted by inset color gradient, with red(blue) indicating high(low) electron density.

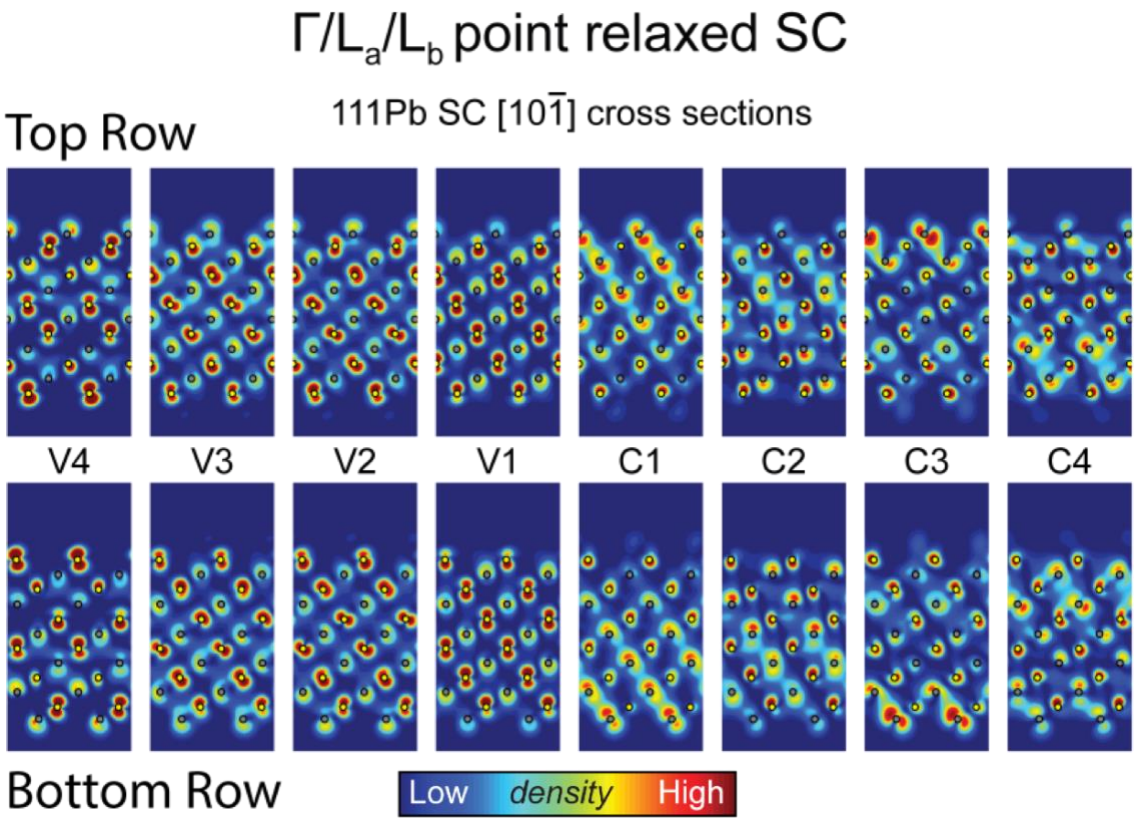

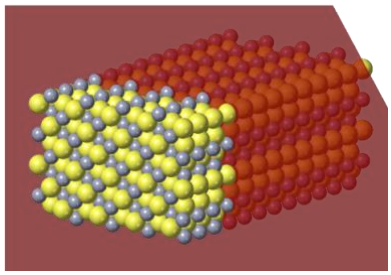

Figure 4.15 Electron density cross-sections of the $\overline{\Gamma}/\overline{M}$ ($\Gamma/L_a/L_b$) point along $[10\bar{1}]$ facets (red plane inset crystal image at right) for the 2 x 1 (111)Pb reconstructed SC slab after relaxation. Corresponding S (yellow) and Pb (gray) atoms in their relaxed lattice positions are shown for clarity. Electron density denoted by inset color gradient, with red(blue) indicating high(low) electron density.

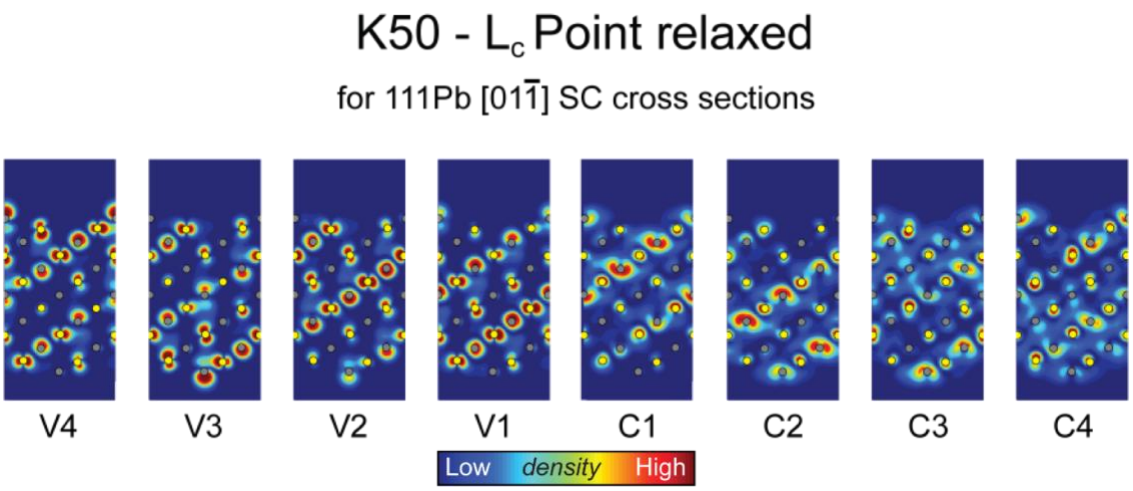

Figure 4.16 Electron density cross-sections of the $\overline{\mathrm{M}}'$ (L_c) point along [01$\bar{1}$] facets (blue plane inset crystal image at right) for the 2 x 1 (111)Pb reconstructed SC slab after relaxation. Corresponding S (yellow) and Pb (gray) atoms in their relaxed lattice positions are shown for clarity. Electron density denoted by inset color gradient, with red(blue) indicating high(low) electron density.

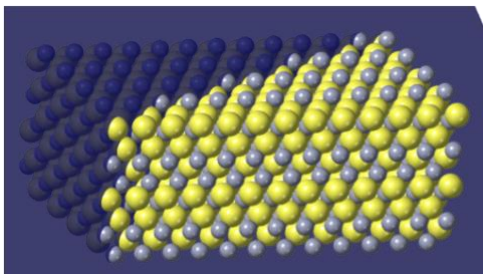

Moreover, the probability density distribution for valence band-edge states of the unrelaxed SC slab structure appears highly inhomogeneous, with density concentrated variously on the upper(lower) half of atoms of the slab in the case of $\mathrm{V}_2^{\overline{\Gamma}/\overline{\mathrm{M}}}$, $\mathrm{V}_3^{\overline{\Gamma}/\overline{\mathrm{M}}}$, and in the case of $\mathrm{V}_4^{\overline{\Gamma}/\overline{\mathrm{M}}}$ specifically on subsurface S_b atoms, and correlates with atomic orbital projection character observations, especially for $\overline{\Gamma}/\overline{\mathrm{M}}$ ($\Gamma/L_a/L_b$) states, with increased surface Pb atomic orbital character (Figure 4.4a, and 4.6a). By contrast, unrelaxed [0$\bar{1}$0] facet probability density slices of $\overline{\mathrm{M}}'$ (L_c) states (Figure 4.12) exhibit markedly different character with most band edge states exhibiting p-orbital like density oriented roughly parallel with the SC slab surfaces, and surface Pb atom density confined to the surface with little to no interaction with slab interior atoms.

Significant changes to the probability density distribution on surface and subsurface atoms for $\overline{\Gamma}/\overline{\mathrm{M}}$ ($\Gamma/L_a/L_b$) and $\overline{\mathrm{M}}'$ (L_c) states are observed following atomic relaxation, leading to increased interaction and reorganization of atomic orbitals. Importantly, the inhomogeneity observed for unrelaxed $\overline{\Gamma}/\overline{\mathrm{M}}$ ($\Gamma/L_a/L_b$) states of the VB is contrasted with increased probability density distribution over all SC slab atoms observed for VB $\overline{\Gamma}/\overline{\mathrm{M}}$ ($\Gamma/L_a/L_b$) states of the relaxed structure (Figures 4.11, and 4.15), indicating increased bonding and stabilization for these states. However, the most striking and consequential changes in probability density are observed in the conduction band-edge states. For CB $\overline{\Gamma}/\overline{\mathrm{M}}$ ($\Gamma/L_a/L_b$) states, a pattern of increased probability density localized near surface Pb atoms and extending along slab interior Pb atoms of $[0\bar{1}0]$ facets (Figure 4.11) is observed in unoccupied states $\mathrm{C}_1^{\overline{\Gamma}/\overline{\mathrm{M}}}$, $\mathrm{C}_3^{\overline{\Gamma}/\overline{\mathrm{M}}}$, with a loss of surface character in states $\mathrm{V}_1^{\overline{\Gamma}/\overline{\mathrm{M}}}$ and $\mathrm{V}_3^{\overline{\Gamma}/\overline{\mathrm{M}}}$. Figures 4.14 and 4.15, representing relaxed and unrelaxed 2D probability density cross-sections for $[10\bar{1}]$ facets, emphasize – qualitatively – the extent of atomic orbital reorganization near the surface, and further substantiate the increased interaction of surface and slab-interior Pb atoms. As can be seen in figures 4.14 and 4.15 there is an obvious re-orientation of probability density, between unrelaxed and relaxed SC structures, near Pb atoms associated with $[0\bar{1}0]$ facets for states $\mathrm{C}_1^{\overline{\Gamma}/\overline{\mathrm{M}}}$, $\mathrm{C}_3^{\overline{\Gamma}/\overline{\mathrm{M}}}$, starting with Pb atoms of the surface reconstruction rows, and continuing into the slab interior. This observed pattern of the probability density along Pb atomic chains of a $[0\bar{1}0]$ facet for states $\mathrm{C}_1^{\overline{\Gamma}/\overline{\mathrm{M}}}$, $\mathrm{C}_3^{\overline{\Gamma}/\overline{\mathrm{M}}}$, with exponential decay into the vacuum at the surface, and attenuation into the slab interior is indicative of a Tamm surface state,[53] where the probability density pattern observed for higher energy state $\mathrm{C}_3^{\overline{\Gamma}/\overline{\mathrm{M}}}$, differs from $\mathrm{C}_1^{\overline{\Gamma}/\overline{\mathrm{M}}}$ by the location of nodes along the Pb atomic

chains. Even numbered states $C_2^{\overline{\Gamma}/\overline{M}}$, $C_4^{\overline{\Gamma}/\overline{M}}$ exhibit similar patterns of probability density along Pb atomic chains of $[0\bar{1}0]$ facets, though with significantly reduced surface intensity.

In contrast to $\overline{\Gamma}/\overline{M}$ ($\Gamma/L_a/L_b$) states, the probability density associated with $\overline{M}'$ (L_c) states differs markedly, varying in surface character, intensity, geometry, and propagation direction, with no indication of the presence of Tamm surface states. Little change in VB cross-sections of $\overline{M}'$ (L_c) states is observed after relaxation, apart from a shift in probability density near surface Pb atoms from states $V_1^{\overline{M}\prime}$ and $V_2^{\overline{M}\prime}$ to states $V_3^{\overline{M}\prime}$ and $V_4^{\overline{M}\prime}$, in keeping with observations in atomic orbital projection data (Figure 4.4b). CB cross-sections of relaxed $\overline{M}'$ (L_c) states (Figure 4.13) exhibit significant electron probability density distribution over SC slab core atoms, with moderate, highly localized, monotonically increasing probability density for increasing $C_n^{\overline{M}\prime}$ states near surface Pb reconstruction rows in agreement with figure 4.4a. The probability density for conduction band $\overline{M}'$ (L_c) states exhibit linearly polarized directional symmetry (hybridized p orbital-like), with Pb atom probability density interaction oriented in the $[\bar{1}01]$ direction, parallel to surface Pb reconstruction rows. Indeed, the electron probability density, both at the surface and in the slab interior, for low-lying conduction band $\overline{M}'$ (L_c) states is exemplified by intra-plane interactions in x-y plane. For $\overline{M}'$ (L_c) CB states there is no indication of significant interaction between Pb atoms of different $[111]$ layers of the SC slab, unlike their $\overline{\Gamma}/\overline{M}$ ($\Gamma/L_a/L_b$) counterparts. Thus, the probability density orientation of the conduction band-edge $\overline{M}'$ (L_c) states (Figure 4.13) appears to diverge from the preferred wave-vector direction associated with the real space z-axis projection of the $\overline{M}'$ (L_c) wave-vector directions, along the $[\bar{2}11]$ and $[\overline{11}2]$ directions, as seen in figure 4.2a. This is verified by

the observation of minimal atomic orbital interaction for a 2D probability density $[01\bar{1}]$ cross section (Figure 4.16) cutting vertically through the SC slab in the $[\bar{2}11]$ direction. I suggest that $\overline{\mathrm{M}}'$ (L_c) states would prefer to propagate along their preferred <112> directions but can't, and that this divergence from the preferred direction of propagation results, in part, from the anisotropy and reduced symmetry of Pb atom reconstruction rows at the surface. Thus, the lowest energy alternative for the $\overline{\mathrm{M}}'$ (L_c) state along the $[\bar{2}11]$ is to mix with the mirror $\overline{\mathrm{M}}'$ (L_c) state along the $[\bar{1}\bar{1}2]$ direction, leading to $\overline{\mathrm{M}}'$ (L_c) state probability density propagation in the $[\bar{1}01]$ direction. Unexpectedly, $\overline{\mathrm{M}}'$ (L_c) state probability density slices for alternating top and bottom row $[0\bar{1}0]$ facets for valence and conduction band-edge states exhibit significantly depressed probability density throughout, suggesting topologically insulating layers of atoms within the PbS SC slab structure, not observed in $\overline{\Gamma}/\overline{\mathrm{M}}$ ($\Gamma/L_a/L_b$) states.

The considerable differences in electron probability density between the $\overline{\Gamma}/\overline{\mathrm{M}}$ ($\Gamma/L_a/L_b$) and $\overline{\mathrm{M}}'$ (L_c) states, comprising the four L-valleys in the PBZ of PbS, exemplifies and reinforces that surface reconstruction and relaxation have a profound effect on the electronic structure of PbS. In the calculated band structure for the 2 x 1 (111)Pb reconstructed SC slab (Figures 4.4–4.7), the difference in dispersion character and loss of degeneracy observed for band-edge states indicates that electrons in $\overline{\Gamma}/\overline{\mathrm{M}}$ ($\Gamma/L_a/L_b$) and $\overline{\mathrm{M}}'$ (L_c) states are experiencing significantly different local electronic environments. Additionally, observations in the atomic orbital projection (Figures 4.10–4.13) along with atomic analysis of the (111)Pb SC slab PDOS (Figure 4.9) suggests the increased surface Pb atom character of $\overline{\Gamma}/\overline{\mathrm{M}}$ ($\Gamma/L_a/L_b$) conduction band-edge states. Moreover, analysis of Pb

atom d-states (Figure 4.8) indicates an important difference in the potential environments between surface and interior Pb atoms of the (111)Pb SC slab. Thus, the observation of Tamm surface states in the 2D probability density cross sections for $\overline{\Gamma}/\overline{M}$ ($\Gamma/L_a/L_b$) states, centered on Pb atoms of the surface reconstruction rows, is not surprising, and even expected, given the existence of a surface, and observations of surface reconstruction in PbS.

Atoms at the surface of a material experience conditions lying somewhere between isolated atoms and atoms in the bulk material; these conditions are heavily influenced by the particular chemical and physical surface atomic structure and associated surface reconstruction, and are known to be intricately entwined with the existence of surface electronic states.[49] Tamm surface states are defined as solutions to the Schrodinger equation, in the Tight Binding approximation, for electrons moving in a finite crystal, with energies lying in the forbidden energy gap (FEG), and having wave-functions localized at the surface.[53] In this theory, surface states arise from crystal surface cleavage, and subsequent reconstruction, e.g. as modeled by the 2 x 1 (111)Pb reconstructed SC slab surface, leading to substantive differences in the bonding and potential environments for surface atoms, in this case Pb surface atoms, as compared to atoms of the interior – bulk – of the SC slab.[49] For the 2 x 1 (111)Pb reconstructed SC slab model described here, the potential difference for Pb atoms at the surface, as compared to the 'bulk', is large enough such that a Tamm N-type surface state emerges – splits off – below the CBM, with localization of the surface state on Pb surface atoms of the 2 x 1 (111)Pb reconstruction rows.[53] Thus, the splitting off of the Tamm surface state from the conduction band edge, and it's connection to surface Pb atoms, indicates the strong influence of surface

reconstruction, and associated surface Pb anisotropy, on the (111)Pb SC slab electronic structure.

4.3.4. Effective Band Structure; Band Unfolding and PC Eigenstate Contribution

4.3.4.1. Band Unfolding Methodology; a brief description

It is clear from the SBZ band structure (Figures 4.4–4.7) and electron probability density cross-sections (Figures 4.10–4.16) that the cleavage of the PbS surface, and consequent surface reconstruction, have a considerable impact on the $\overline{\Gamma}/\overline{\mathrm{M}}$ ($\Gamma/L_a/L_b$) and $\overline{\mathrm{M}}'$ (L_c) states, and the corresponding individual L-points of the PbS PBZ (Figure 4.3), which are responsible for the primary band gap and photophysical properties of PbS systems. Thus, an understanding of the individual L-points contributions to the SBZ band structure would prove useful in connecting the physical structure of the (111)Pb SC slab surface with the observed electronic states. An unavoidable consequence of using a SC model is the inherent convolution of the resultant SBZ band structure $E(\vec{K})$ due to the folding of the parent PBZ bands $E(\vec{k})$ arising from the reciprocal space (*k*-space) relationship between the SC and underlying PC (Figure 4.3).[12, 37] The (111)Pb SC slab, comprising 12 PCs in a 1 x 2 x 6 arrangement (x, y, z), results in a much smaller corresponding SBZ, due to the inverse size relationship between real and reciprocal space representations. The resultant convolution of PC band structure makes a direct comparison of the SBZ bands $E(\vec{K})$ with that of the PBZ $E(\vec{k})$ nearly impossible, obscuring potential changes to PBZ band structure as a result of specific structural perturbations – i.e. surface reconstruction. To address the SBZ band convolution issue, a theoretical methodology has been developed whereby the complicated band structure $E(\vec{K})$ of the SBZ is "unfolded", revealing the band structure

$E(\vec{k})$ of the underlying parent PBZ.[12, 37, 54, 55] Strictly speaking, band unfolding using the following methodology is only equivalent for a SC that is a perfect replica of the associated PC along one or more translational axis.[12] However, for small perturbations to the system (i.e. impurities, surface reconstruction, and lattice defects),[12] an effective band structure (EBS) can be produced from this unfolding procedure, and provides an excellent physically relevant description of the electronic structure of the SC.[12, 56] We have applied this band unfolding procedure to the SBZ bands of the (111)Pb SC slab. The resultant EBS enables the observation and elucidation of changes to the PbS PC band structure for wave-vectors of interest, namely the PBZ L-points, as a result of the (111) Pb surface reconstruction.

The methodology for the unfolding process has been presented in great detail previously,[12, 37, 54-56] and so only the salient details will be described herein. The geometric relationships, and thus the wave vector folding/unfolding relationships, between the SBZ and PBZ are entirely defined by the PC and SC basis vectors $\vec{\boldsymbol{A}}$ and $\vec{\boldsymbol{a}}$ respectively, and the transformation matrix *M*, where $\vec{\boldsymbol{A}} = M \cdot \vec{\boldsymbol{a}}$. The number $N_{\vec{K}}$ of PBZ wave vectors $\vec{k}$ that fold into a single SBZ wave vector $\vec{K}$ is defined by $N_{\vec{K}} = \Omega_{PBZ}/\Omega_{SBZ}$, where Ω_{PBZ} & Ω_{SBZ} are the volumes of the PBZ and SBZ respectively. The unfolding relationship between the SBZ and PBZ wave vectors is then defined as

$$\vec{k}_i = \vec{K} + \vec{G}_i \quad i = 1,2,3,\dots,N_{\vec{K}} \tag{1}$$

where $\vec{G}_i$, are the SC reciprocal lattice vectors. It is important to note that only unique $\vec{K}$, $\vec{G}_i$ combinations unfold to individual $\vec{k}_i$, whereas $N_{\vec{K}}$ different pairs ($\vec{k}_i$, $\vec{G}_i$) fold into a single $\vec{K}$, as seen in equation (2).

$$\vec{K} = \vec{k}_i - \vec{G}_i \tag{2}$$

Using the zone folding relationship between SC and PC wave vectors in equation 1, eigenvectors of the SC and PC representations, $|\vec{K}m\rangle$ and $|\vec{k}_i n\rangle$ respectively, can be related through the expression

$$|\vec{K}m\rangle = \sum_{i=1}^{N_{\vec{K}}} \sum_n f(\vec{k}_i, n; \vec{K}, m)|\vec{k}_i n\rangle \quad (3)$$

describing the folding of PC eigenvectors into those of the SC, where m and n are band indices of the SBZ and PBZ respectively. To produce the EBS for the SC we need to obtain information regarding the probability of PC eigenstate $|\vec{k}_i n\rangle$ contributions to individual SC eigenstates $|\vec{K}m\rangle$, or in other words, the amount of PC Bloch character present in $|\vec{K}m\rangle$. This is accomplished by calculation of the *spectral weight* $P_{\vec{K}m}(\vec{k}_i)$ for each SC wave-vector $\vec{K}$ resulting from the $N_{\vec{K}}$ PC wave-vector components $\vec{k}_i$:

$$P_{\vec{K}m}(\vec{k}_i) = \sum_n |\langle \vec{K}m|\vec{k}_i n\rangle|^2 = \sum_{\vec{g}} |C_{\vec{K}m}(\vec{g} + \vec{k}_i - \vec{K})|^2 \quad (4)$$

where $C_{\vec{K}m}$ are the coefficients of the plane-wave expansion of SC states, and $\vec{g}$ are the reciprocal lattice vectors of the PC. Finally, construction of the EBS is accomplished by defining a spectral function such that,

$$A(k_i, E) = \sum_m P_{\vec{K}m}(\vec{k}_i)\, \delta(E_m(\vec{K}) - E) \quad (5)$$

which defines the amount of PC Block character contribution (spectral character), depending on wave-vector, for each band. Thus, the only information required to accomplish the unfolding of the SC bands are the results of the SC calculations, and the PC and SC basis vectors $\vec{\boldsymbol{A}}$ and $\vec{\boldsymbol{a}}$**,** all other information and relationships are derived from these, and knowledge of the PC eigenvectors is not necessary.[56] The transformation matrix *M* between PC and SC basis vectors is not diagonal, nor does it need to be in the most

general case, as a result of the fact that SC and PC unit vectors are not collinear.[12] Thus, transformations between the $\overline{\Gamma}/\overline{\mathrm{M}}$, and $\overline{\mathrm{M}}'$ wave-vectors of the 2D SBZ and corresponding 3D PBZ wave-vectors L, X, and Γ were determined through geometric relations of the SC and PC lattice vectors $\vec{\boldsymbol{A}}$ and $\vec{\boldsymbol{a}}$, respectively.

4.3.4.2. Band unfolding and the resultant effective band structure

The EBS obtained using the unfolding procedure described above can be seen in figure 4.17, is comprised of wave vectors along the L_a, L_b, and L_c segments (Figure 4.17b) normal to the (111) surface, and connects important high symmetry points (L, X, and Γ) of the PBZ. The EBS shows the dispersion and spectral character (grayscale shaded wave vectors) for bands of the L_a, L_b segments corresponding to the $\overline{\Gamma}/\overline{\mathrm{M}}$ point, and L_c segment corresponding to the $\overline{\mathrm{M}}'$ point of the 2D surface SBZ, and provides further evidence of the effects of surface reconstruction on the PbS electronic structure. Due to quantum confinement resulting from the finite thickness (~2 nm) of the (111)Pb SC slab, the bands of the EBS along each of the L_n segments are mostly flat, except for higher energy unoccupied bands of the L_a and L_b segments. (111)Pb SC bands of the L_a and L_b segments (Figure 4.17) have the same quantized band dispersion $E(\vec{k})$ owing to the fact that they are both derived from the $\overline{\Gamma}/\overline{\mathrm{M}}$ point of the 2D surface SBZ – though their PC spectral character is quite dissimilar. In contrast, the quantized band dispersion and PC spectral character of the L_c segment ($\overline{\mathrm{M}}'$) is markedly different from that of the L_a and L_b segments, in keeping with the findings of the SC band structure in figures 4.4 through 4.7. Generally, overlaid PbS bulk bands (red dotted lines in Figure 4.17) align with increased PC spectral character seen in bands of the different L_n segments, highlighting the effect of quantization on the

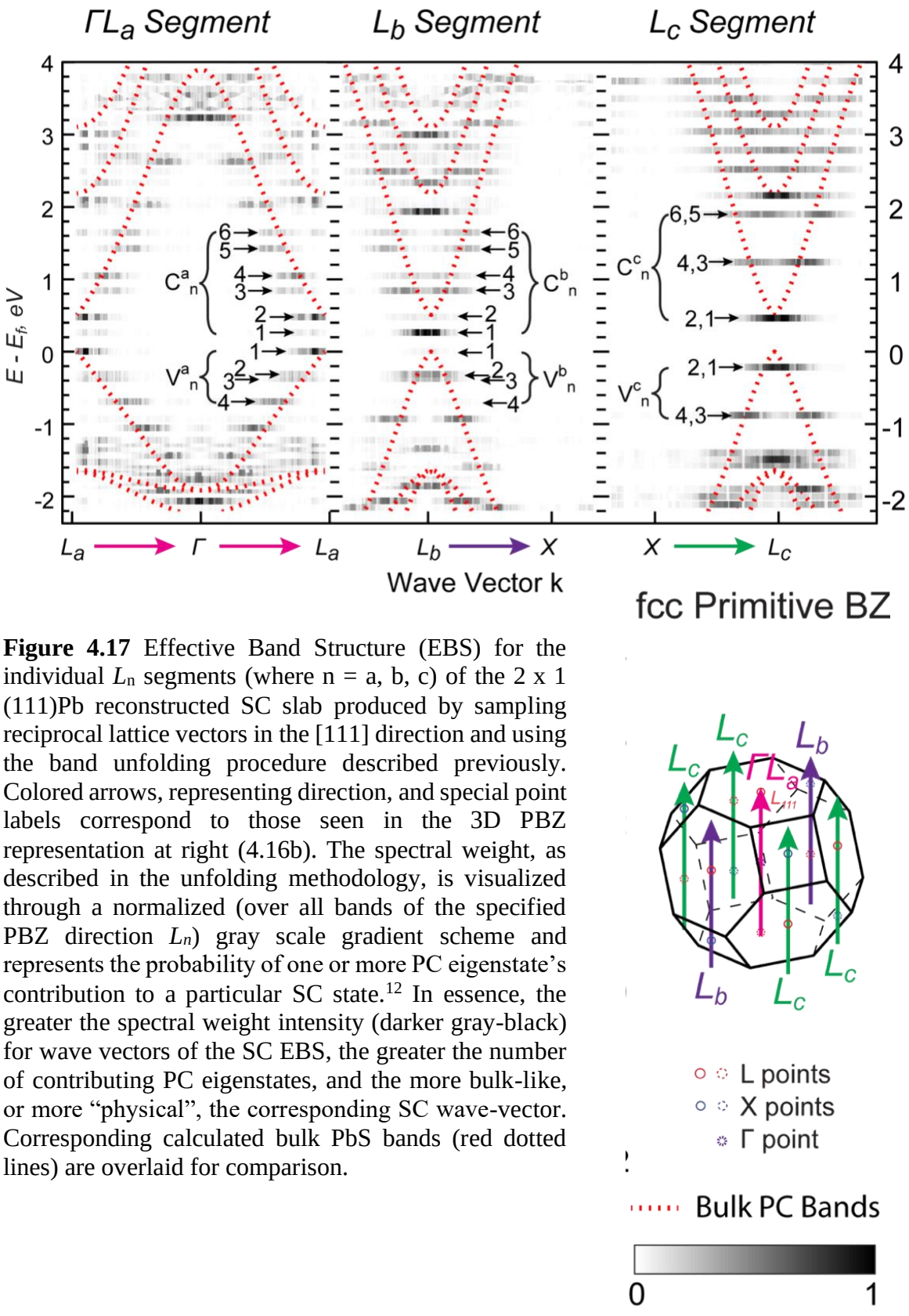

Figure 4.17 Effective Band Structure (EBS) for the individual L_n segments (where n = a, b, c) of the 2 x 1 (111)Pb reconstructed SC slab produced by sampling reciprocal lattice vectors in the [111] direction and using the band unfolding procedure described previously. Colored arrows, representing direction, and special point labels correspond to those seen in the 3D PBZ representation at right (4.16b). The spectral weight, as described in the unfolding methodology, is visualized through a normalized (over all bands of the specified PBZ direction L_n) gray scale gradient scheme and represents the probability of one or more PC eigenstate's contribution to a particular SC state.[12] In essence, the greater the spectral weight intensity (darker gray-black) for wave vectors of the SC EBS, the greater the number of contributing PC eigenstates, and the more bulk-like, or more "physical", the corresponding SC wave-vector. Corresponding calculated bulk PbS bands (red dotted lines) are overlaid for comparison.

bulk bands in the PbS SC slab. Interestingly, the C_1 band, for both the L_a and L_b segments near the L_a and L_b points, lies below the first bulk band (dotted red line), and would indicate the presence of a split-off band from the conduction band edge.

As can be seen in figure 4.17 the highest intensity PC spectral character are observed at the conduction and valence band-edge bands near to the corresponding L_n points for corresponding L_n segments. High PC spectral character is observed for the L_a segment (Figure 4.17) near the L_a point for bands V_1^a and C_2^a, with vanishingly small PC spectral character contribution in the lowest unoccupied band C_1^a. Conversely, the highest PC spectral character contribution of the L_b segment (Figure 4.17) is seen in the C_1^b band near the L_b point, while bands V_1^b and C_2^b exhibit minimal PC spectral contribution – the exact opposite of L_a segment. The fact that the bands corresponding to the VBM and CBM with high PC spectral character, bands V_1^a and C_1^b respectively, are located at different wave vectors of the (111)Pb SC EBS (the L_a and L_b points of the L_a and L_b segments respectively), and thus near different L-points of the PBZ, indicate the emergence of a pseudo-indirect band gap for the (111)Pb SC slab.[12] In contrast, PC eigenstate character is equivalently high for both the V_1^c and V_2^c, as well as the C_1^c, C_2^c band pairs near the L_c point of the L_c segment, though at different energies from the other L_n segments, as noted previously.

The directional orientation of electron density through the (111)Pb SC slab seen in the 2D probability density cross-sections for SBZ states $\overline{\Gamma}/\overline{\mathrm{M}}$ and $\overline{\mathrm{M}}'$ (Figures 4.10–4.16) is further informed through comparison with the EBS spectral character near L_n points of the L_a, L_b, and L_c segments. For example, surface z-axis projections of the atomic orbital alignment for states $\mathrm{C}_1^{\overline{\Gamma}/\overline{\mathrm{M}}}$ (containing a Tamm surface state) shows orientation in the $[\bar{1}2\bar{1}]$

direction (Figures 4.11, and 4.15), orthogonal to 2 x 1 (111)Pb SC reconstruction rows. Concurrently, the EBS state C_1^b , at the L_b point of the L_b segment, exhibits high spectral character indicating a majority contribution for this state is derived from the L-point of the PBZ associated with the surface BZ $\overline{\mathrm{M}}$ point located in the $[\bar{1}2\bar{1}]$ direction. Thus, the $[\bar{1}2\bar{1}]$ direction of atomic orbital alignment z-axis projection matches with the z-axis projection of the $\overline{\Gamma} \rightarrow \overline{\mathrm{M}}$ surface BZ direction (Figure 4.2a), associated with the L_b point of the L_b segment (Figure 4.17) for the unfolded EBS. By contrast, the 2D probability density $[10\bar{1}]$ cross-sections for the states $\mathrm{V}_{!}^{\overline{\Gamma}/\overline{\mathrm{M}}}$ and $\mathrm{C}_2^{\overline{\Gamma}/\overline{\mathrm{M}}}$(Figure 4.15) exhibit majority atomic orbital alignment along the z-axis of (111)Pb SC slab, the [111] direction normal to the SC slab surface, indicating a majority contribution from an altogether different L point of the PBZ, the L_a point of the L_a segment. Indeed, the $\overline{\Gamma}$ point of the surface BZ is associated with the L_a segment of the PBZ, with the PBZ path $\Gamma \rightarrow \mathrm{L_a}$ in the [111] direction, normal to the (111)Pb SC slab surface. However, since the L_a and L_b segments containing the L_a and L_b points are folded into the $\overline{\Gamma}/\overline{\mathrm{M}}$ point of the SBZ, the corresponding unfolded EBS bands may display mixed character where neither L_a or L_b points of the EBS indicate dominant spectral character – states $\mathrm{V}_2^{\overline{\Gamma}/\overline{\mathrm{M}}}$ and $\mathrm{V}_3^{\overline{\Gamma}/\overline{\mathrm{M}}}$ (Figures 4.15, and 4.17) for example. Consequently, atomic orbital alignment of the 2D probability density cross-sections exhibit directional character dependent on the amount of PC spectral character of the associated EBS L_n segment bands, with $\overline{\Gamma}/\overline{\mathrm{M}}$ conduction band states alternating majority contributions of directional character between L_a and L_b segments.

From the above observations it is apparent that the directional anisotropy of the (111)Pb reconstructed surface, apart from elemental considerations, plays an important role in the

alteration of the PbS electronic structure. A primary example of the effect of surface reconstruction anisotropy is on the z-axis projection anisotropic propagation of the associated conduction band-edge Tamm surface states (Figures 4.11, and 4.15) in the $[\bar{1}2\bar{1}]$ direction, orthogonal to the Pb reconstruction row direction. Moreover, $\overline{M}'$ (Figure 4.13) states are not able to propagate along their preferred crystallographic directions – $[\bar{2}11]$ and $[\overline{11}2]$, but instead are forced to propagate parallel to the Pb reconstruction rows along the $[\bar{1}01]$ direction. Finally, the divergent PC spectral character for different L_n points of the (111)Pb SC EBS, corresponding to the different PBZ L points, provides further proof. Thus, it is clear that surface reconstruction, and surface atomic anisotropy, has an enormous effect on the electronic structure of PbS especially at the L points of the PBZ, impacting the optoelectronic properties of PbS quantum wells and nanocrystals with reconstructed (111)Pb surfaces.

4.4 Conclusion

In the absence of ligand passivation, fully-occupied PbS (111)Pb facets are energetically unstable, and likely to undergo reconstruction, similar to the 2 x 1 (111)Pb type reconstruction shown in Figure 4.2a, resulting in half-occupied facets with Pb-rich surfaces.[34, 35] In this chapter, I have shown that 2 x 1 (111)Pb surface reconstruction in PbS is likely to result in the formation of Tamm surface states at the conduction band-edge localized on surface Pb reconstruction row atoms. These states are split off from the conduction band-edge as a result of the differing potential environment of Pb atoms at the PbS (111)Pb reconstructed surface, the (111) Pb surface atoms being three-fold under-coordinated as compared to their sister atoms in the bulk. Due to real and reciprocal space symmetry considerations of the 2 x 1 (111)Pb surface reconstruction, the normally 4-fold

degenerate L points of the PbS PBZ, being the location of the primary band-gap and thus responsible for the optoelectronic properties of PbS, show split characters in the unfolded SBZ EBS. Electronic states at the $\overline{\Gamma}/\overline{\mathrm{M}}$ ($\Gamma/L_a/L_b$) SBZ symmetry point are stabilized as a result of their real/reciprocal space correspondence with the overarching periodicity of the 2 x 1 (111)Pb surface reconstruction rows (the wave-vector for the L_b symmetry runs orthogonal to the real-space representation of the 2 x 1 (111)Pb surface reconstruction rows). In contrast, electronic states of the $\overline{\mathrm{M}}'$ (L_c) SBZ symmetry points do not exhibit the same stabilization as states of the $\overline{\Gamma}/\overline{\mathrm{M}}$ ($\Gamma/L_a/L_b$) symmetry points, as can be observed in their differing dispersion character, and divergent energies of the $\mathrm{C}_n^{\overline{\mathrm{M}}'}$ and $\mathrm{C}_n^{\overline{\Gamma}/\overline{\mathrm{M}}}$ states, resulting from decreased symmetry of the real/reciprocal space correspondence (Figures 4.4–4.7). In addition, the formation of Tamm surface states at the conduction band edge corresponds with increased electronic interaction of surface Pb atoms and Pb atoms of the slab interior resulting in stabilization, and a lowering of energy for these states (Figures 4.11, 4.15, and 4.17) These observations suggest that the formation of reconstructed surfaces for PbS nanocrystal (111) facets, similar to the (111)Pb reconstructed surface modeled here, may result in the appearance of low-energy, conduction band-edge states in PbS nanocrystals, localized on surface Pb adatoms. Thus, a decrease in the apparent bandgap for PbS nanocrystals with (111) facets, resulting from surface reconstruction, and leading to the formation of conduction band-edge Tamm surface states, is in agreement with the experimental observation of surface localized conduction band-edge states, and significantly reduced bandgaps, in naked, annealed PbS NCs.[22, 23]

CHAPTER V
CONCLUSION

Research into the uses of semiconducting NCs, especially for NIR absorbing PbX NCs, has exploded over the past two decades. Superlative NC properties of efficient, frequency-specific, light emission and absorption lend themselves to a myriad of applications in the information technology age such as energy- and space-efficient flat screen displays, solar energy conversion, medical and environmental sensing applications, and cutting-edge laser and communications technologies. Over the past two decades significant improvements to, and maturation of, solution processing procedures, increasingly complex device architectures, and various surface defect mitigation techniques, through improved passivating ligand technologies and core-shell structures, have brought NC quantum dots to the tipping point of commercial viability. However, further research into, and techniques for the mitigation of, surface trap states resulting from under-passivation of surface defects or significant surface off-stoichiometry is required in order to bring NC quantum dot technologies into the mainstream. To that end, this dissertation has striven to explore and elucidate surface defects and their effect on NC electronic structure, especially surface reconstruction of polar (111) surfaces, which have been shown to be the root cause of sub-bandgap states in PbS NCs.

In chapter II, we used the powerful nanoscale investigatory techniques afforded by the Nazin group's home-built scanning tunneling microscope to expose the underlying surface structural causes of conduction band-edge states in annealed, ligand free PbS NCs. Importantly, surface structural information, revealed by topographic scans of the annealed NCs, exhibited crystallographic information such as well-defined step edges and crystal

facets with crystallographic directions. Using the instruments superlative STS capabilities, we were able to record reproducible, spatially resolved, DOS spectra for numerous NCs, which showed a manifold of sub-bandgap electronic states at the conduction band-edge. These conduction band-edge states also show a strong correlation between their spatially resolved DOS features and NC surface structures, specifically step-edges of the PbS polar (111) facets. As a result of their limited extent, and the correlation with NC topographic features, these sub-bandgap electronic states were determined not to be quantum confined states of the PbS NCs, but rather surface localized states. Due to these observations, and because the as prepared PbS NCs are known to be Pb rich at the surface, we asserted that the observed manifold of conduction band-edge states is likely the result of surface add-atoms, specifically Pb atoms, owing to their association with the conduction band-edge.

In chapter III, we expanded our observations of the electronic states of the PbS NC bandgap region in order to improve our understanding of the correlation between local surface structure, and localized sub-bandgap states. The observed DOS features in the PbS NCs included the previously mentioned manifold of conduction band-edge states, as well as states at the valence band-edge, and states crossing the Fermi level. All spatially resolved DOS features in the sub-bandgap region where found to be highly localized on the surfaces and edges of the observed NCs, which is highly suggestive of local conditions, such as surface reconstruction or severe off-stoichiometries contributing to the formation of the observed electronic states. Indeed, the spatially resolved manifold of DOS features at the conduction band-edge were observed to be highly correlated with crystallographic features of the NCs, determined by topographic measurement, specifically on (111) surfaces or at step edges, indicating the surface structural nature of these states. We suggest that, due to

the polar nature of PbS (111) surfaces, that they are prone to reconstruction in order to lower their energy, and that PbS NCs are known to be Pb rich at the surface, the observed conduction band-edge states result from surface reconstruction of Pb-rich polar (111) facets.

Following our STS explorations of the electronic states of PbS NC, especially in the bandgap region, we determined to undertake a theoretical exploration of specific surface reconstruction known to occur on PbS (111) surfaces, for the purpose of corroboration and elucidation of the origin of observed sub-bandgap states at the conduction band edge. We targeted the 2 x 1 (111) surface reconstruction specifically, due to its observed occurrence on the PbS (111) surface, and hinted at by topographic observations made during our exploration of PbS NC surfaces. Through the use of band diagrams and electron density cross-sections produced from DFT simulations we show that 2 x 1 (111)Pb surface reconstruction produces Tamm surface states split off from the conduction band-edge associated with the Pb surface reconstruction row atoms. In addition, due to real/reciprocal space symmetry considerations, the 2 x 1 (111)Pb surface reconstruction causes splitting in the conduction band-edge bands' dispersion character for the normally 4-fold degenerate L-points of the PbS fcc Brillouin zone, the location of the primary bandgap in PbS. Split character at the PbS conduction band-edge reciprocal space L-point symmetries are further supported by the unfolding of the PbS 2 x 1 (111)Pb slab super-cell Brillouin Zone (SBZ) band structure into an effective band structure (EBS). These observations of surface reconstruction induced conduction band-edge Tamm surface states agrees with our STS and topographic observations from previous chapters of surface localized conduction ban-edge states in PbS nanocrystals.

In the above research we have shown through STS measurements of the DOS that sub-bandgap states in naked PbS NCs are widely prevalent, indeed, are the norm, and result from significant surface off-stoichiometry and surface reconstruction of (111) PbS facets. DFT simulations of reconstructed PbS (111) surfaces further showed that conduction band-edge states observed in the DOS of PbS NCs result from Tamm surface states associated with Pb reconstruction row atoms at the PbS surface. We believe that this research has shed new light on the causes of surface trap states in PbS NCs, and once again shown the outsized importance of the NC surface in determining the principal characteristics of the NC band-gap with the profound implications for the optoelectronic properties of devices constructed from PbS NCs.

APPENDIX A

SUPPORTING MATERIAL FOR CHAPTER II

From Dmitry A. Kislitsyn, Christian F. Gervasi, Thomas Allen, Peter K.B. Palomaki, Jason D. Hackley, Ryuichiro Maruyama, and George V. Nazin was previously published under the same title in J. Phys. Chem. Lett. 5, 3701–3707 (2014).

NC Crystallographic Orientation

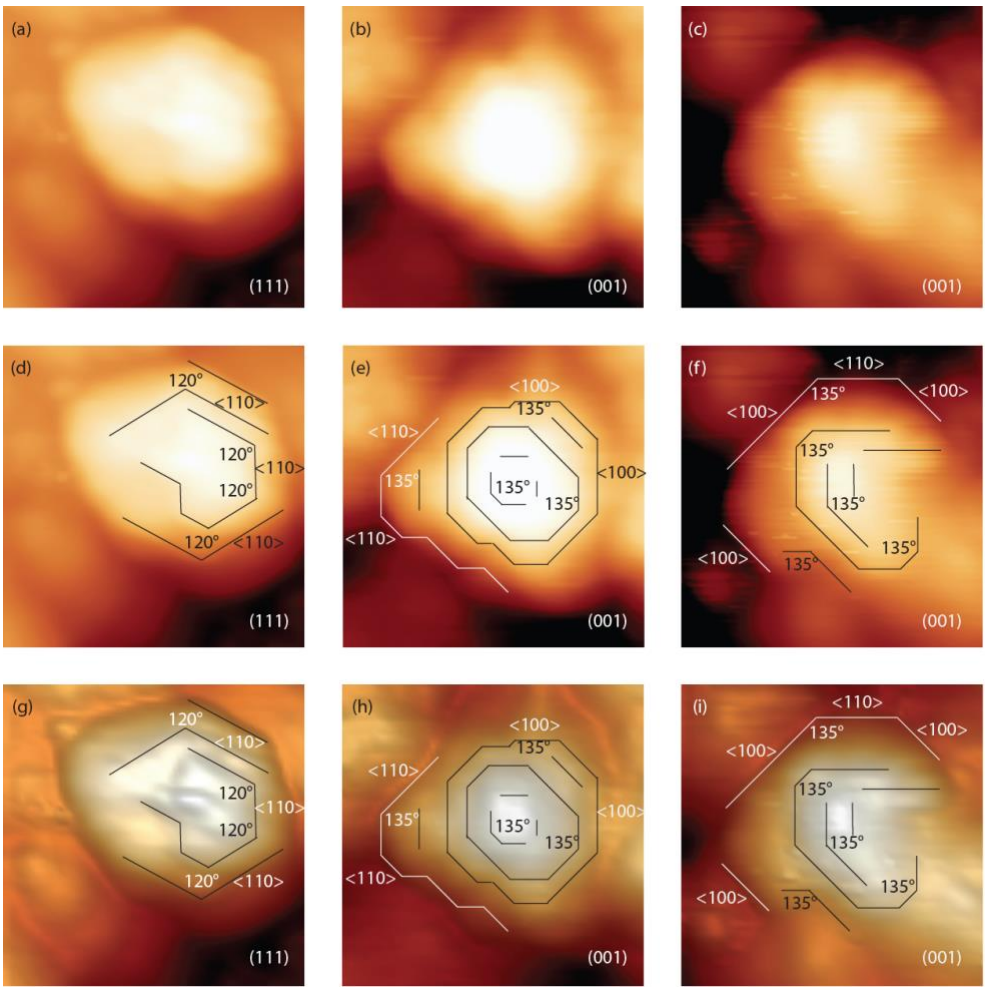

Figure A1. STM topographic images showing crystallographic features for three PbS NCs. (a), (b), (c) Topographies for three representative NCs. (d), (e), (f) NC topographies, [same as in (a), (b), and (c) respectively] with lines and relative angles indicating orientations of crystallographic features for each NC. The observed angles suggest that the top NC facets corresponds to crystal planes (111), (100), and (100) respectively. (g), (h), (i) Enhanced topographic images [for the same NCs] with same crystallographic markings as in (d), (e) and (f).

NC Band Bending

Mismatch of work functions in the tip ϕ_{tip} and substrate ϕ_{Au}, together with the finite voltage drop ΔV inside the NC, lead to a shift of electronic state E_1 by $e\Delta V = \alpha(\, eV_b + \Delta\phi)$, where V_b is the applied bias voltage, $\Delta\phi = \phi_{tip} - \phi_{Au}$, and e is the electron charge. Parameter α thus relates the average potential inside the nanocrystal to the external potentials applied across the tunneling gap. Therefore, states E_1 (unoccupied) and H_1 (occupied) are observed at voltages V_E and V_H that are defined by the following equations:[1-2]

$$eV_E = \frac{E_1 + \alpha\Delta\phi}{1-\alpha}$$

$$eV_H = \frac{H_1 + \alpha\Delta\phi}{1-\alpha}$$

Where E_1 and H_1 are the true energies of states E_1 and H_1 with respect to the substrate Fermi level. Voltages V_E and V_H are determined directly from the STS spectra. Observations of "reverse" tunneling spectral features[1, 3] analogous to H** lead to typical values of α on the scale of a few percent.

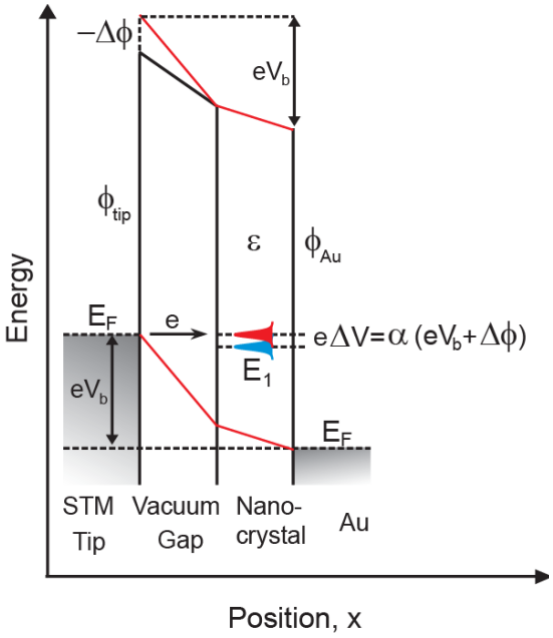

Figure A2. Voltage drop in a biased STM junction with a NC under the STM tip.

The changes in voltages V_E and V_H observed in Figure A3 of the main text are caused by the fact that α depends on the relative distance between the tip apex and the "centers of gravity" of states E_1 and H_1. Factor α is higher at the periphery of NC1, as compared to the

center of NC_1 top facet because in the former case the tip is located closer to the Au surface, which results in a larger electric field inside the NC, leading to higher effective voltage drop inside the NC. Without the $\Delta\phi$ term, this effect would lead to "curving" of V_E and V_H trajectories away from axis V = 0 in Figure 3b, as observed for V_H. In the present case, however, $\Delta\phi$ is nonzero and negative. This reinforces the "curving" trend observed for V_H, but counteracts the "curving" of V_E.

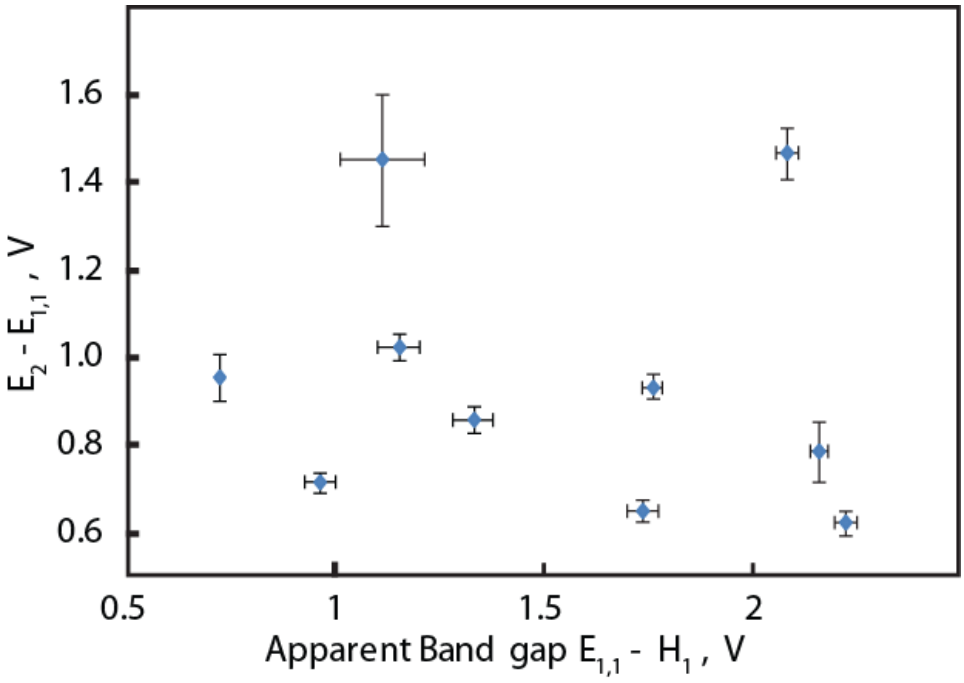

Figure A3. Plot of the energy difference between the E_2 and $E_{1,1}$ states vs. the energy difference between the $E_{1,1}$ and H_1 states for 10 measured NCs. During this experiment, many of the measured NCs did not exhibit clearly-defined H_1 or E_2 states, and thus were not included here.

PbS nanocrystal synthesis

Synthesis of PbS NCs was performed following a modified procedure from Hines and Scholes.[4] Lead oxide (PbO, 99.0%), oleic acid (OA, technical grade 90%), 1-octadecene

(ODE, technical grade 90%, pumped on at 80° C for 8 hours), toluene (99.8%, anhydrous), pentane (anhydrous), methanol (anhydrous), pentanethiol (98%), and pentanedithiol (96%) were purchased from Sigma-Aldrich and used as received unless otherwise stated. Bis(trimethylsilyl)sulfide ($(TMS)_2S$, synthesis grade) was purchased from Gelest.

All syntheses were conducted using standard Schlenk techniques. In a typical synthesis, 4 mL of ODE and 4 mL of OA were combined with 0.30 g of PbO (1.3 mmol). The mixture was heated, with stirring, to 100° C for 30 minutes, then heated to the injection temperature of 105° C for at least 30 minutes, all under vacuum. A sulfur precursor solution containing 0.167 mL (0.8 mmol) of $(TMS)_2S$ in 4 mL of ODE was prepared in a glovebox under nitrogen atmosphere. The sulfur precursor solution was quickly injected into the flask and held at 95° C for 1 minute, then cooled to room temperature in an ice bath. Removal of excess ligand and 1-octadecene was completed by repeated precipitation in acetone, centrifugation of the particles, and dispersion in small amounts of toluene. Finally, the NC dispersion was filtered through a 0.2 μm syringe filter to remove any insoluble material.

Prior to using PbS NCs in STS experiments, a ligand exchange was performed using a combination of pentanethiol and pentanedithiol in an effort to improve NC adhesion to the gold substrate and remove highly insulating OA ligands. In a typical ligand exchange procedure 0.3 mL of stock solution of PbS NC (15 mg/mL in toluene) was diluted with 5 mL of pentane in a centrifuge tube with an air-tight lid with septum. Several drops of pentanethiol stock solution (9:1 pentanethiol:pentanedithiol, total concentration 0.15 M in pentane) were added via syringe and then mixed. Pentanethiol capped PbS NCs were precipitated from pentane using methanol and centrifuged at 3500 rpm. Following removal

of the supernatant, NCs were redispersed in toluene. This cleaning procedure was repeated two times. Finally, PbS NCs were dispersed in anhydrous pentane to produce a 0.9 mg/mL stock solution. The suspension was centrifuged to remove aggregates, and the remaining dispersed NCs were transferred to a clean tube under N_2 for use in STM experiments.

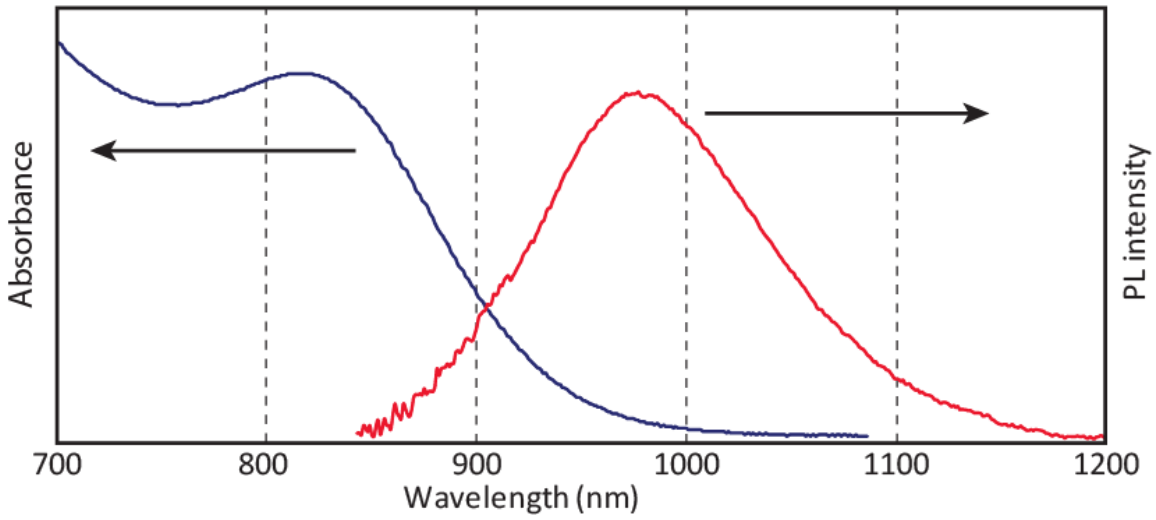

Figure A4. Absorbance and PL spectra of PbS NCs following thiol-ligand exchange. The emission peak at 977 nm (1.27 eV) corresponds to an approximate diameter of 3.2 nm PbS NC.

APPENDIX B

SUPPORTING MATERIAL FOR CHAPTER III

This chapter by Christian F. Gervasi, Dmitry A. Kislitsyn, Thomas L. Allen, Jason D. Hackley, Ryuichiro Maruyama, and George V. Nazin was previously published under the same title in *Nanoscale* **2015**, 7 (46), 19732–19742 Copyright © 2015 Royal Society of Chemistry.

Figure B1. (Right) shows the prominent unoccupied states for NC1. Subfigures (a-f) include (from left to right) a combination of topography(grayscale), and DOS map(color) overlay (where the yellow outline encloses the area of DOS mapping), DOS map only, and DOS map with black lines showing DOS features that are in registry with NC1 crystallographic features from Figure 1g in the main text. Parameter α is defined as the distance between two neighboring {211} planes, as shown in the model in Figures 6a and b in the main text. STS measurements taken with set-point 1.6 V bias, 30 pA tunneling current. STM topography image measured with set-point 2.0 V bias, 2 pA tunneling current.

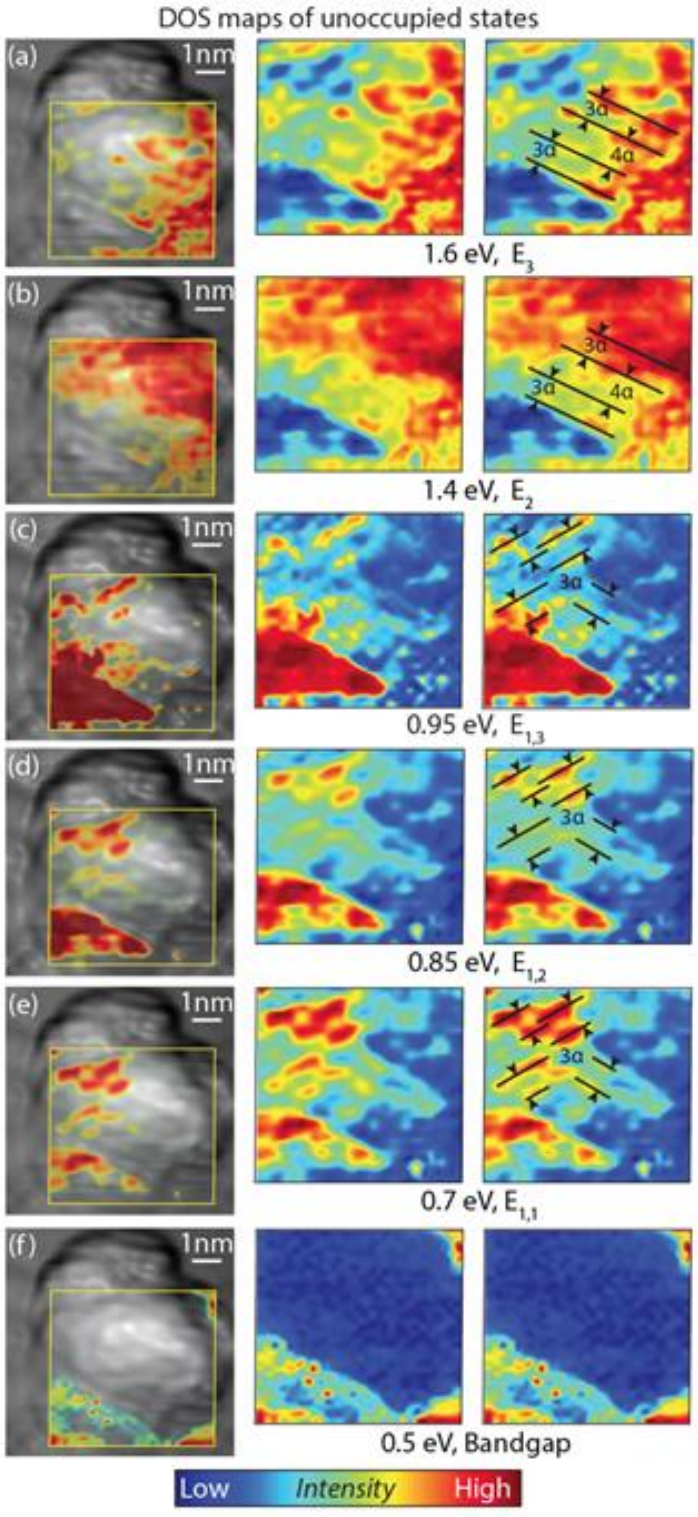

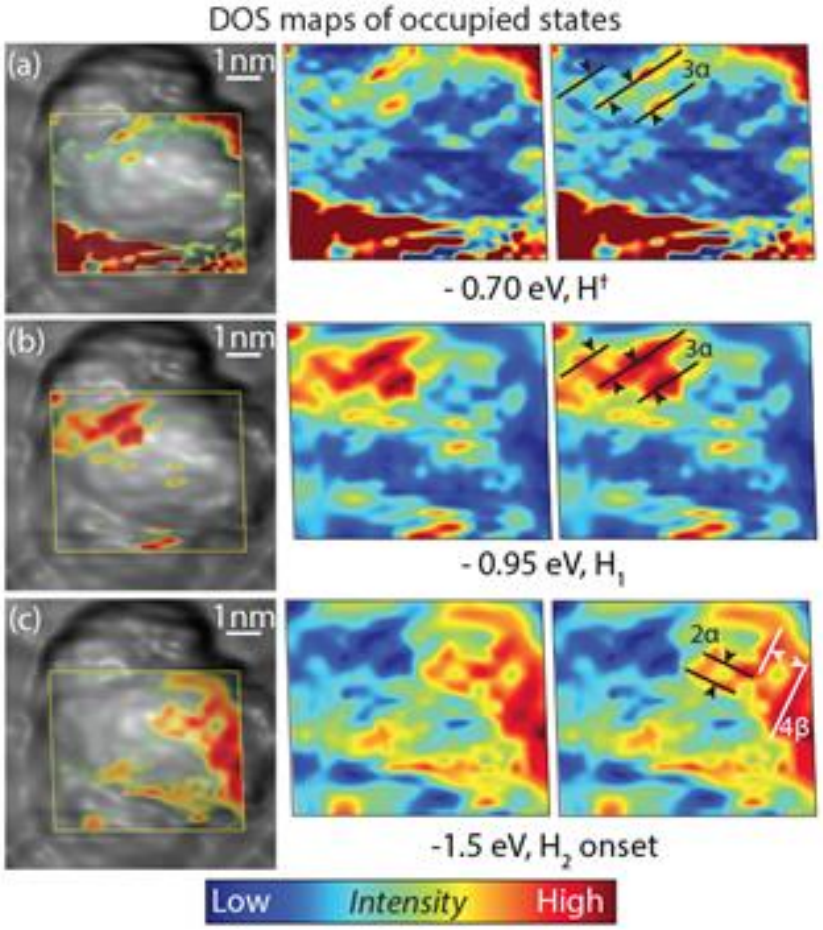

Figure B2. (below) shows the prominent occupied states for NC1. Same area and representation as Figure S1 for the occupied states of NC1. Parameter β is defined as the distance between two neighboring {110} planes, as shown in the model in Figures 6c and d in the main text. Set-points of STM topography image and STS maps same as in Figure B1.

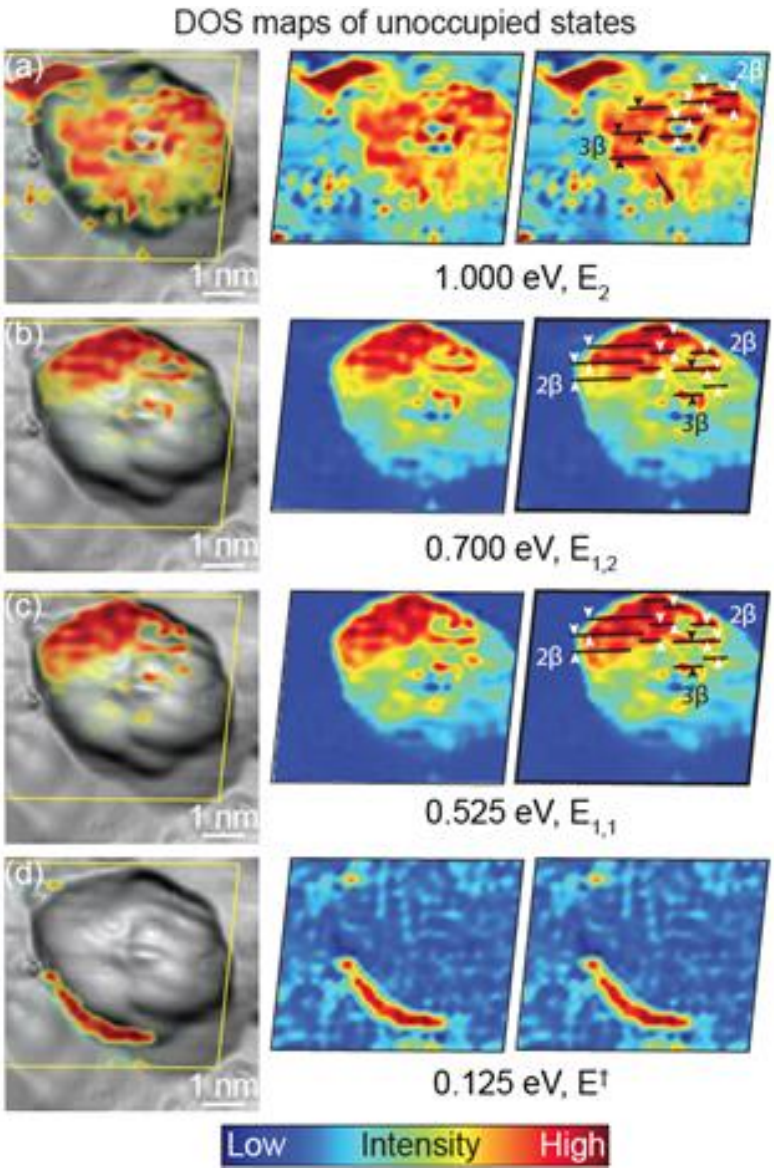

Figure B3. (below) shows the prominent unoccupied states of NC2. Same representation as in Figure S1 for NC1. Parameter β is defined as before for figure S2, and as shown in the model in Figures 6c and d in the main text. STM topography measured with set-point 2.0 V bias, 1 pA tunneling current. STS maps measured with set-point 1.5 V bias, 20 pA tunneling current.

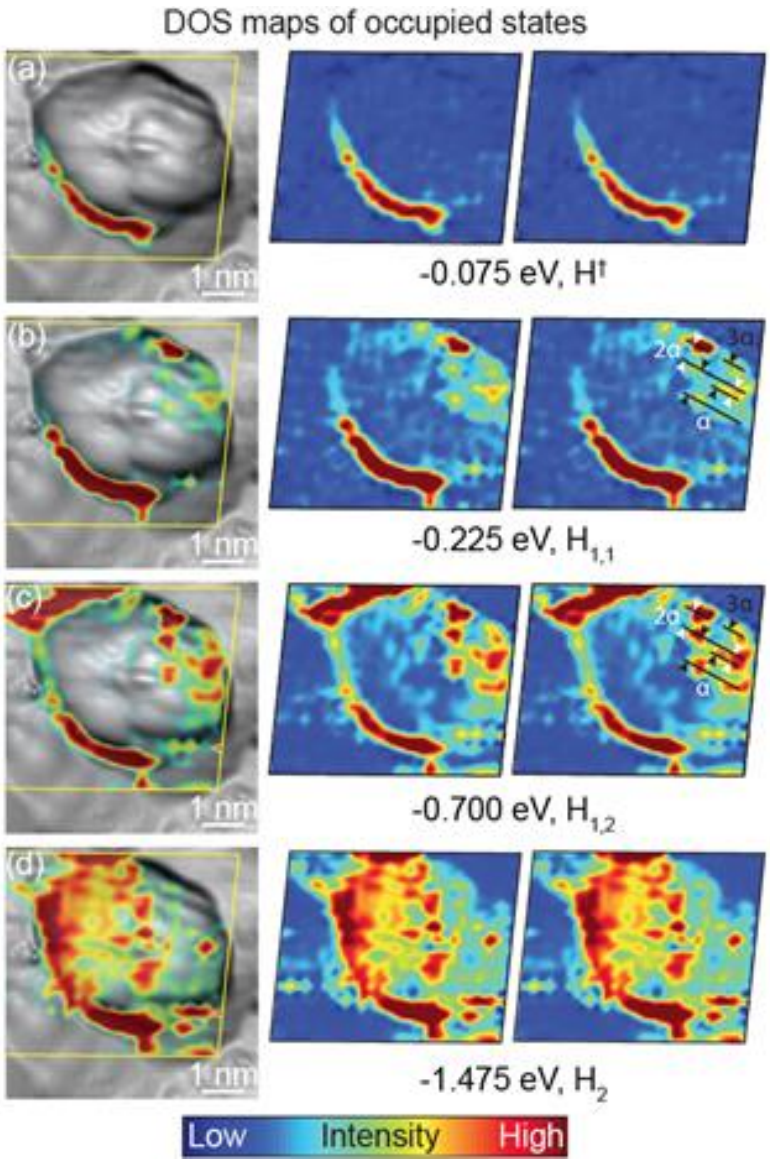

Figure B4. (below) shows the prominent occupied states of NC2. Same representation as in Figure S3 for NC2. Parameter α is defined as the distance between two neighboring {211} planes, as shown in the model in Figures 6a and b in the main text. Set-points of STM topography image and STS maps same as in Figure S3.

Figure B5. (Right) shows examples of PbS NCs displaying localized defect-related states in their DOS. Unoccupied $E_{1,n}$ and occupied H_1 states show marked intensity differences depending on location, and are associated with the reconstruction of polar PbS (111) surfaces or regions of marked non-stoichiometry in which excess S (Pb) atoms at the surface lead to sub-bandgap states broken off from the valence(conduction) bands. These observations are in keeping with and further support conclusions made with regard to the sub-bandgap states observed for NCs discussed in the main journal article.

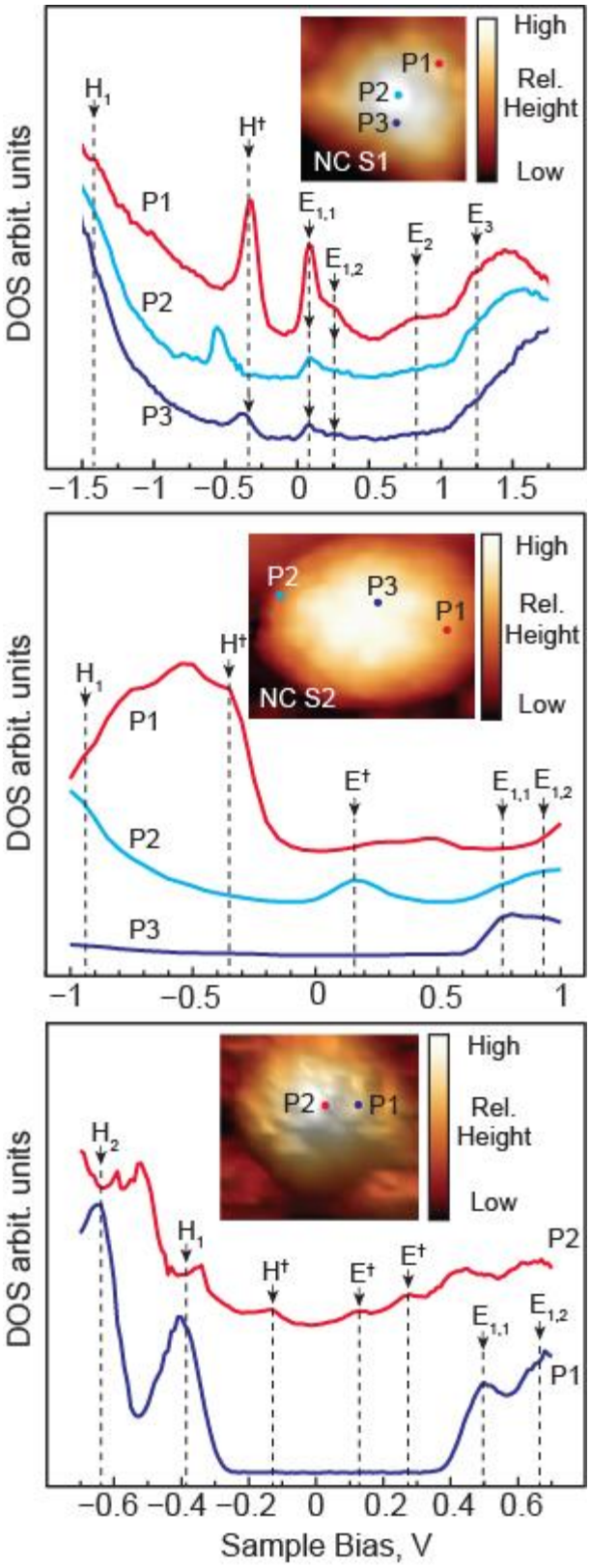

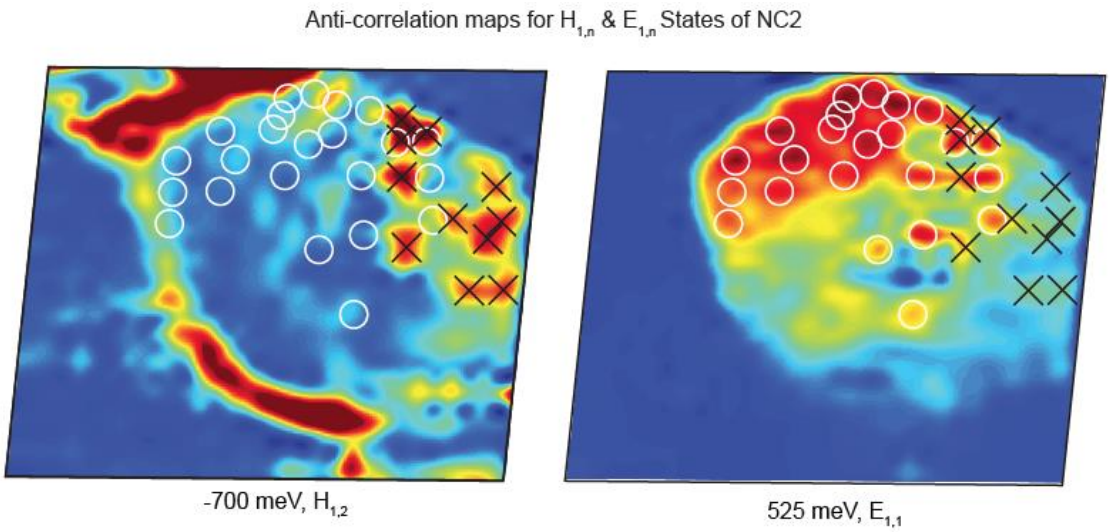

Figure B6. DOS maps for $H_{1,n}$ and $E_{1,n}$ states of NC2 showing anti-correlation in their spatial distributions. White circles (black x's) mark locations of local high intensity for states $E_{1,n}$ ($H_{1,n}$)

DOS intensity maps for the sub-bandgap states of NC2 (Figure B6), show that the locations of high intensity for states $H_{1,n}$ in general correspond (on the atomic scale) to locations of low intensity for states $E_{1,n}$, and vice-versa suggesting that $H_{1,n}$ and $E_{1,n}$ patterns are carried by atoms corresponding to different elements. Theoretical calculations predict that $H_{1,n}$ and $E_{1,n}$ patterns result from non-stoichiometric surface S and Pb atoms respectively.[1]

REFERENCE CITED

REFERENCES CITED FOR CHAPTER I

(1) Chuang, C.-H. M.; Brown, P. R.; Bulović, V.; Bawendi, M. G. Improved Performance and Stability in Quantum Dot Solar Cells through Band Alignment Engineering. *Nat Mater* **2014,** *13* (8), 796-801.

(2) Ning, Z. J.; Voznyy, O.; Pan, J.; Hoogland, S.; Adinolfi, V.; Xu, J. X.; Li, M.; Kirmani, A. R.; Sun, J. P.; Minor, J.; Kemp, K. W.; Dong, H. P.; Rollny, L.; Labelle, A.; Carey, G.; Sutherland, B.; Hill, I.; Amassian, A.; Liu, H.; Tang, J.; Bakr, O. M.; Sargent, E. H. Air-Stable N-Type Colloidal Quantum Dot Solids. *Nature Materials* **2014,** *13* (8), 822-828.

(3) Liu, Y.; Gibbs, M.; Puthussery, J.; Gaik, S.; Ihly, R.; Hillhouse, H. W.; Law, M. Dependence of Carrier Mobility on Nanocrystal Size and Ligand Length in PbSe Nanocrystal Solids. *Nano Letters* **2010,** *10* (5), 1960-1969.

(4) Liu, Y.; Tolentino, J.; Gibbs, M.; Ihly, R.; Perkins, C. L.; Liu, Y.; Crawford, N.; Hemminger, J. C.; Law, M. PbSe Quantum Dot Field-Effect Transistors with Air-Stable Electron Mobilities above 7 cm(2) V-1 s(-1). *Nano Letters* **2013,** *13* (4), 1578-1587.

(5) Lan, X.; Voznyy, O.; García de Arquer, F. P.; Liu, M.; Xu, J.; Proppe, A. H.; Walters, G.; Fan, F.; Tan, H.; Yang, Z.; Hoogland, S.; Sargent, E. H. 10.6% Certified Colloidal Quantum Dot Solar Cells via Solvent-Polarity-Engineered Halide Passivation. *Nano Lett* **2016,** *16* (7), 4630-4.

(6) Choi, M. J.; García de Arquer, F. P.; Proppe, A. H.; Seifitokaldani, A.; Choi, J.; Kim, J.; Baek, S. W.; Liu, M.; Sun, B.; Biondi, M.; Scheffel, B.; Walters, G.; Nam, D. H.; Jo, J. W.; Ouellette, O.; Voznyy, O.; Hoogland, S.; Kelley, S. O.; Jung, Y. S.; Sargent, E. H. Cascade surface modification of colloidal quantum dot inks enables efficient bulk homojunction photovoltaics. *Nat Commun* **2020,** *11* (1), 103.

(7) Hendricks, M. P.; Campos, M. P.; Cleveland, G. T.; Jen-La Plante, I.; Owen, J. S. NANOMATERIALS. A tunable library of substituted thiourea precursors to metal sulfide nanocrystals. *Science* **2015,** *348* (6240), 1226-30.

(8) Campos, M. P.; Hendricks, M. P.; Beecher, A. N.; Walravens, W.; Swain, R. A.; Cleveland, G. T.; Hens, Z.; Sfeir, M. Y.; Owen, J. S. A Library of Selenourea Precursors to PbSe Nanocrystals with Size Distributions near the Homogeneous Limit. *J Am Chem Soc* **2017,** *139* (6), 2296-2305.

(9) Preske, A.; Liu, J.; Prezhdo, O. V.; Krauss, T. D. Large-Scale Programmable Synthesis of PbS Quantum Dots. *Chemphyschem* **2016,** *17* (5), 681-6.

(10) Tang, J. A.; Sargent, E. H. Infrared Colloidal Quantum Dots for Photovoltaics: Fundamentals and Recent Progress. *Advanced Materials* **2011,** *23* (1), 12-29.

(11) Tang, J.; Liu, H.; Zhitomirsky, D.; Hoogland, S.; Wang, X.; Furukawa, M.; Levina, L.; Sargent, E. H. Quantum Junction Solar Cells. *Nano Letters* **2012,** *12* (9), 4889-4894.

(12) Tang, J.; Brzozowski, L.; Barkhouse, D. A. R.; Wang, X.; Debnath, R.; Wolowiec, R.; Palmiano, E.; Levina, L.; Pattantyus-Abraham, A. G.; Jamakosmanovic, D.; Sargent, E. H. Quantum Dot Photovoltaics in the Extreme Quantum Confinement Regime: The Surface-Chemical Origins of Exceptional Air- and Light-Stability. *Acs Nano* **2010,** *4* (2), 869-878.

(13) Thon, S. M.; Ip, A. H.; Voznyy, O.; Levina, L.; Kemp, K. W.; Carey, G. H.; Masala, S.; Sargent, E. H. Role of Bond Adaptability in the Passivation of Colloidal Quantum Dot Solids. *ACS Nano* **2013,** *7* (9), 7680-7688.

(14) Tang, J.; Kemp, K. W.; Hoogland, S.; Jeong, K. S.; Liu, H.; Levina, L.; Furukawa, M.; Wang, X. H.; Debnath, R.; Cha, D. K.; Chou, K. W.; Fischer, A.; Amassian, A.; Asbury, J. B.; Sargent, E. H. Colloidal-Quantum-Dot Photovoltaics Using Atomic-Ligand Passivation. *Nature Materials* **2011,** *10* (10), 765-771.

(15) Soreni-Harari, M.; Yaacobi-Gross, N.; Steiner, D.; Aharoni, A.; Banin, U.; Millo, O.; Tessler, N. Tuning energetic levels in nanocrystal quantum dots through surface manipulations. *Nano Letters* **2008,** *8* (2), 678-684.

(16) Brown, P. R.; Kim, D.; Lunt, R. R.; Zhao, N.; Bawendi, M. G.; Grossman, J. C.; Bulovi, V. Energy level modification in lead sulfide quantum dot thin films through ligand exchange. *ACS Nano* **2014,** *8* (6), 5863-5872.

(17) Ding, B.; Wang, Y.; Huang, P.-s.; Waldeck, D. H.; Lee, J.-k. Depleted Bulk Heterojunctions in Thermally Annealed PbS Quantum Dot Solar Cells Depleted Bulk Heterojunctions in Thermally Annealed PbS Quantum Dot Solar Cells. *The Journal of Physical Chemistry C* **2014,** *118* (7), 14749-14758.

(18) Hetsch, F.; Zhao, N.; Kershaw, S. V.; Rogach, A. L. Quantum Dot Field Effect Transistors. *Materials Today* **2013,** *16* (9), 312-325.

(19) Kovalenko, M. V.; Scheele, M.; Talapin, D. V. Colloidal Nanocrystals with Molecular Metal Chalcogenide Surface Ligands. *Science* **2009,** *324* (5933), 1417-1420.

(20) Hartley, C. L.; Kessler, M. L.; Dempsey, J. L. Molecular-Level Insight into Semiconductor Nanocrystal Surfaces. *J Am Chem Soc* **2021,** *143* (3), 1251-1266.

(21) Kim, D.; Kim, D.-H.; Lee, J.-H.; Grossman, J. C. Impact of Stoichiometry on the Electronic Structure of PbS Quantum Dots. *Physical Review Letters* **2013,** *110* (19), 196802.

(22) Fang, C.; van Huis, M. A.; Vanmaekelbergh, D.; Zandbergen, H. W. Energetics of Polar and Nonpolar Facets of PbSe Nanocrystals from Theory and Experiment. *Acs Nano* **2009,** *4* (1), 211-218.

(23) Kaushik, A. P.; Lukose, B.; Clancy, P. The Role of Shape on Electronic Structure and Charge Transport in Faceted PbSe Nanocrystals. *Acs Nano* **2014,** *8* (3), 2302-2317.

(24) Lu, H.; Carroll, G. M.; Neale, N. R.; Beard, M. C. Infrared Quantum Dots: Progress, Challenges, and Opportunities. *ACS Nano* **2019,** *13* (2), 939-953.

(25) Kislitsyn, D. A.; Gervasi, C. F.; Allen, T.; Palomaki, P. K. B.; Hackley, J. D.; Maruyama, R.; Nazin, G. V. Spatial Mapping of Sub-Bandgap States Induced by Local Nonstoichiometry in Individual Lead Sulfide Nanocrystals. *Journal of Physical Chemistry Letters* **2014,** *5* (21), 3701-3707.

(26) Gervasi, C. F.; Kislitsyn, D. A.; Allen, T. L.; Hackley, J. D.; Maruyama, R.; Nazin, G. V. Diversity of sub-bandgap states in lead-sulfide nanocrystals: real-space spectroscopy and mapping at the atomic-scale. *Nanoscale* **2015,** *7* (46), 19732-19742.

(27) Kislitsyn, D. A.; Kocevski, V.; Mills, J. M.; Chiu, S. K.; Gervasi, C. F.; Taber, B. N.; Rosenfield, A. E.; Eriksson, O.; Rusz, J.; Goforth, A. M.; Nazin, G. V. Mapping of Defects in Individual Silicon Nanocrystals Using Real-Space Spectroscopy. *Journal of Physical Chemistry Letters* **2016,** *7* (6), 1047-1054.

(28) Kislitsyn, D. A.; Mills, J. M.; Kocevski, V.; Chiu, S. K.; DeBenedetti, W. J. I.; Gervasi, C. F.; Taber, B. N.; Rosenfield, A. E.; Eriksson, O.; Rusz, J.; Goforth, A. M.; Nazin, G. V. Communication: Visualization and spectroscopy of defects induced by dehydrogenation in individual silicon nanocrystals. *Journal of Chemical Physics* **2016,** *144* (24).

(29) Alivisatos, A. P. Semiconductor Clusters, Nanocrystals, and Quantum Dots. *Science* **1996,** *271* (5251), 933-937.

(30) Brus, L. Quantum crystallites and nonlinear optics. *Applied Physics A* **1991,** *53*, 465-474.

(31) Klimov, V. I. *Nanocrystal Quantum Dots*. 2nd ed.; CRC Press, Taylor & Francis Group: Boca Raton, **2010**.

(32) Nirmal, M.; Brus, L. Luminescence Photophysics in Semiconductor Nanocrystals. *Accounts of Chemical Research* **1999,** *32* (5), 407-414.

(33) Kang, I.; Wise, F. Electronic structure and optical properties of PbS and PbSe quantum dots. *J. Opt. Soc. Am. B* **1997,** *14* (7), 1632-1646.

(34) Moreels, I.; Justo, Y.; De Geyter, B.; Haustraete, K.; Martins, J. C.; Hens, Z. Size-Tunable, Bright, and Stable PbS Quantum Dots: A Surface Chemistry Study. *Acs Nano* **2011,** *5* (3), 2004-2012.

(35) Giansante, C.; Infante, I.; Fabiano, E.; Grisorio, R.; Suranna, G. P.; Gigli, G. "Darker-than-black" PbS quantum dots: enhancing optical absorption of colloidal semiconductor nanocrystals via short conjugated ligands. *J Am Chem Soc* **2015,** *137* (5), 1875-86.

(36) Saran, R.; Curry, R. J. Lead sulphide nanocrystal photodetector technologies. *Nature Photonics* **2016,** *10* (2), 81-92.

(37) Zhang, J.; Crisp, R. W.; Gao, J.; Kroupa, D. M.; Beard, M. C.; Luther, J. M. Synthetic Conditions for High-Accuracy Size Control of PbS Quantum Dots. *J Phys Chem Lett* **2015,** *6* (10), 1830-3.

(38) Weidman, M. C.; Beck, M. E.; Hoffman, R. S.; Prins, F.; Tisdale, W. A. Monodisperse, air-stable PbS nanocrystals via precursor stoichiometry control. *ACS Nano* **2014,** *8* (6), 6363-71.

(39) Lee, S. M.; Jun, Y. W.; Cho, S. N.; Cheon, J. Single-crystalline star-shaped nanocrystals and their evolution: programming the geometry of nano-building blocks. *J Am Chem Soc* **2002,** *124* (38), 11244-5.

(40) Tang, J.; Kemp, K. W.; Hoogland, S.; Jeong, K. S.; Liu, H.; Levina, L.; Furukawa, M.; Wang, X.; Debnath, R.; Cha, D.; Chou, K. W.; Fischer, A.; Amassian, A.; Asbury, J. B.; Sargent, E. H. Colloidal-Quantum-Dot Photovoltaics Using Atomic-Ligand Passivation. *Nature Materials* **2011,** *10* (10), 765-771.

(41) Brown, P. R.; Kim, D.; Lunt, R. R.; Zhao, N.; Bawendi, M. G.; Grossman, J. C.; Bulović, V. Energy level modification in lead sulfide quantum dot thin films through ligand exchange. *ACS Nano* **2014,** *8* (6), 5863-72.

(42) Chen, C. J. *Introduction to Scanning Tunneling Microscopy*. Second Edition ed.; Oxford University Press: New York, **2008**.

(43) Griffiths, D.; Schroeter, D. *Introduction to Quantum Mechanics*. 3rd ed. ed.; Cambridge University Press.: **2018**; p 508.

(44) Bardeen, J. Tunnelling from a Many-Particle Point of View. *Physical Review Letters* **1961,** *6* (2), 57-59.

(45) Giaever, I. Electron Tunneling Between Two Superconductors. *Physical Review Letters* **1960,** *5* (10), 464-466.

(46) Tersoff, J.; Hamann, D. R. Theory of the scanning tunneling microscope. *Phys Rev B Condens Matter* **1985,** *31* (2), 805-813.

(47) Tersoff, J.; Hamann, D. R. Theory and Application for the Scanning Tunneling Microscope. *Physical Review Letters* **1983,** *50* (25), 1998-2001.

(48) Hackley, J. D.; Kislitsyn, D. A.; Beaman, D. K.; Ulrich, S.; Nazin, G. V. High-Stability Cryogenic Scanning Tunneling Microscope Based on a Closed-Cycle Cryostat. *Review of Scientific Instruments* **2014,** *85* (10), 103704.

(49) Pan, S. H.; Hudson, E. W.; Davis, J. C. 3He refrigerator based very low temperature scanning tunneling microscope. *Review of Scientific Instruments* **1999,** *70* (2), 1459-1463.

(50) Binnig, G.; Smith, D. P. E. Single-tube three-dimensional scanner for scanning tunneling microscopy. *Rev. Sci. Instrum.* **1986,** *57* (8), 1688-1689.

(51) McMahon, H. O.; Gifford, W. E. A New Low-Temperature Gas Expansion Cycle. In *Advances in Cryogenic Engineering*, Timmerhaus, K. D., Ed. Springer US: **1960**; Vol. 5, pp 354-367.

(52) Hodgson, P. A.; Wang, Y.; Mohammad, A. A.; Kruse, P. Note: electrochemical etching of silver tips in concentrated sulfuric acid. *Rev Sci Instrum* **2013,** *84* (2), 026109.

(53) Sasaki, S. S.; Perdue, S. M.; Rodriguez Perez, A.; Tallarida, N.; Majors, J. H.; Apkarian, V. A.; Lee, J. Note: Automated electrochemical etching and polishing of silver scanning tunneling microscope tips. *Rev Sci Instrum* **2013,** *84* (9), 096109.

(54) Wiesendanger, R. *Scanning probe microscopy and spectroscopy: methods and applications*. Cambridge University Press: **1994**.

(55) Hanke, F.; Björk, J. Structure and local reactivity of the Au(111) surface reconstruction. *Physical Review B* **2013,** *87* (23), 235422.

(56) Taber, B. N.; Kislitsyn, D. A.; Gervasi, C. F.; Mills, J. M.; Rosenfield, A. E.; Zhang, L.; Mannsfeld, S. C. B.; Prell, J. S.; Briseno, A. L.; Nazin, G. V. Real-space visualization of conformation-independent oligothiophene electronic structure. *Journal of Chemical Physics* **2016,** *144* (19).

(57) Kislitsyn, D. A.; Taber, B. N.; Gervasi, C. F.; Zhang, L.; Mannsfeld, S. C. B.; Prell, J. S.; Briseno, A. L.; Nazin, G. V. Oligothiophene wires: impact of torsional conformation on the electronic structure. *Physical Chemistry Chemical Physics* **2016,** *18* (6), 4842-4849.

(58) Moreels, I.; Lambert, K.; Smeets, D.; De Muynck, D.; Nollet, T.; Martins, J. C.; Vanhaecke, F.; Vantomme, A.; Delerue, C.; Allan, G.; Hens, Z. Size-Dependent Optical Properties of Colloidal PbS Quantum Dots. *Acs Nano* **2009,** *3* (10), 3023-3030.

REFERENCES CITED FOR CHAPTER II

(1) Kershaw, S. V.; Susha, A. S.; Rogach, A. L. Narrow Bandgap Colloidal Metal Chalcogenide Quantum Dots: Synthetic Methods, Heterostructures, Assemblies, Electronic and Infrared Optical Properties. *Chem. Soc. Rev.* **2013,** *42*, 3033-3087.

(2) Tang, J. A.; Sargent, E. H. Infrared Colloidal Quantum Dots for Photovoltaics: Fundamentals and Recent Progress. *Advanced Materials* **2011,** *23*, 12-29.

(3) Nozik, A. J. Spectroscopy and Hot Electron Relaxation Dynamics in Semiconductor Quantum Wells and Quantum Dots. *Annu. Rev. Phys. Chem.* **2001,** *52*, 193-231.

(4) Nozik, A. J. Quantum Dot Solar Cells. *Physica E* **2002,** *14*, 115-120.

(5) Beard, M. C.; Ellingson, R. J. Multiple Exciton Generation in Semiconductor Nanocrystals: Toward Efficient Solar Energy Conversion. *Laser Photon. Rev.* **2008,** *2*, 377-399.

(6) Beard, M. C.; Midgett, A. G.; Hanna, M. C.; Luther, J. M.; Hughes, B. K.; Nozik, A. J. Comparing Multiple Exciton Generation in Quantum Dots to Impact Ionization in Bulk Semiconductors: Implications for Enhancement of Solar Energy Conversion. *Nano Lett.* **2010,** *10*, 3019-3027.

(7) Sandeep, C. S. S.; Cate, S. t.; Schins, J. M.; Savenije, T. J.; Liu, Y.; Law, M.; Kinge, S.; Houtepen, A. J.; Siebbeles, L. D. A. High Charge-Carrier Mobility Enables Exploitation of Carrier Multiplication in Quantum-Dot Films. *Nat. Commun.* **2013,** *4*.

(8) Tisdale, W. A.; Williams, K. J.; Timp, B. A.; Norris, D. J.; Aydil, E. S.; Zhu, X. Y. Hot-Electron Transfer from Semiconductor Nanocrystals. *Science* **2010,** *328*, 1543-1547.

(9) Shockley, W.; Queisser, H. J. Detailed Balance Limit of Efficiency of P-N Junction Solar Cells. *J. Appl. Phys.* **1961,** *32*, 510-519.

(10) Chuang, C.-H. M.; Brown, P. R.; Bulović, V.; Bawendi, M. G. Improved Performance and Stability in Quantum dot Solar Cells through Band Alignment engineering. *Nat. Mater.* **2014,** *13*, 796-801.

(11) Ning, Z. J.; Voznyy, O.; Pan, J.; Hoogland, S.; Adinolfi, V.; Xu, J. X.; Li, M.; Kirmani, A. R.; Sun, J. P.; Minor, J., et al. Air-Stable N-Type Colloidal Quantum Dot Solids. *Nat. Mater.* **2014,** *13*, 822-828.

(12) Ip, A. H.; Thon, S. M.; Hoogland, S.; Voznyy, O.; Zhitomirsky, D.; Debnath, R.; Levina, L.; Rollny, L. R.; Carey, G. H.; Fischer, A., et al. Hybrid Passivated Colloidal Quantum Dot Solids. *Nat. Nanotechnol.* **2012,** *7*, 577-582.

(13) Fernee, M. J.; Thomsen, E.; Jensen, P.; Rubinsztein-Dunlop, H. Highly Efficient Luminescence from a Hybrid State Found in Strongly Quantum Confined PbS Nanocrystals. *Nanotechnology* **2006,** *17*, 956-962.

(14) Gao, J.; Johnson, J. C. Charge Trapping in Bright and Dark States of Coupled PbS Quantum Dot Films. *ACS Nano* **2012,** *6*, 3292-3303.

(15) Tang, J.; Kemp, K. W.; Hoogland, S.; Jeong, K. S.; Liu, H.; Levina, L.; Furukawa, M.; Wang, X.; Debnath, R.; Cha, D., et al. Colloidal-Quantum-Dot Photovoltaics Using Atomic-Ligand Passivation. *Nat. Mater.* **2011,** *10*, 765-771.

(16) Hughes, B. K.; Ruddy, D. A.; Blackburn, J. L.; Smith, D. K.; Bergren, M. R.; Nozik, A. J.; Johnson, J. C.; Beard, M. C. Control of PbSe Quantum Dot Surface Chemistry and Photophysics Using an Alkylselenide Ligand. *ACS Nano* **2012,** *6*, 5498-5506.

(17) Kovalenko, M. V.; Scheele, M.; Talapin, D. V. Colloidal Nanocrystals with Molecular Metal Chalcogenide Surface Ligands. *Science* **2009,** *324*, 1417-1420.

(18) Luther, J. M.; Law, M.; Song, Q.; Perkins, C. L.; Beard, M. C.; Nozik, A. J. Structural, Optical and Electrical Properties of Self-Assembled Films of PbSe Nanocrystals Treated with 1,2-Ethanedithiol. *ACS Nano* **2008,** *2*, 271-280.

(19) Bozyigit, D.; Volk, S.; Yarema, O.; Wood, V. Quantification of Deep Traps in Nanocrystal Solids, Their Electronic Properties, and Their Influence on Device Behavior. *Nano Lett.* **2013,** *13*, 5284-5288.

(20) Diaconescu, B.; Padilha, L. A.; Nagpal, P.; Swartzentruber, B. S.; Klimov, V. I. Measurement of Electronic States of PbS Nanocrystal Quantum Dots Using Scanning Tunneling Spectroscopy: The Role of Parity Selection Rules in Optical Absorption. *Phys. Rev. Lett.* **2013,** *110*, 127406.

(21) Nagpal, P.; Klimov, V. I. Role of Mid-Gap States in Charge Transport and Photoconductivity in Semiconductor Nanocrystal Films. *Nat. Commun.* **2011,** *2*, 486.

(22) Chen, C. J. *Introduction to Scanning Tunneling Microscopy, Oxford University Press New York* 2008.

(23) Sun, Z. X.; Swart, I.; Delerue, C.; Vanmaekelbergh, D.; Liljeroth, P. Orbital and Charge-Resolved Polaron States in Cdse Dots and Rods Probed by Scanning Tunneling Spectroscopy. *Phys. Rev. Lett.* **2009,** *102*, 196401.

(24) Krauss, T. D.; Wise, F. W.; Tanner, D. B. Observation of Coupled Vibrational Modes of a Semiconductor Nanocrystal. *Phys. Rev. Lett.* **1996,** *76*, 1376-1379.

(25) Overgaag, K.; Vanmaekelbergh, D.; Liljeroth, P.; Mahieu, G.; Grandidier, B.; Delerue, C.; Allan, G. Electron-Phonon Coupling and Intervalley Splitting Determine the Linewidth of Single-Electron Transport through PbSe Nanocrystals. *J. Chem. Phys.* **2009,** *131*, 224510.

(26) Hens, Z.; Vanmaekelbergh, D.; Stoffels, E.; van Kempen, H. Effects of Crystal Shape on the Energy Levels of Zero-Dimensional PbS Quantum Dots. *Phys. Rev. Lett.* **2002,** *88*, 236803.

(27) van Huis, M. A.; Kunneman, L. T.; Overgaag, K.; Xu, Q.; Pandraud, G.; Zandbergen, H. W.; Vanmaekelbergh, D. Low-Temperature Nanocrystal Unification through Rotations and Relaxations Probed by in Situ Transmission Electron Microscopy. *Nano Lett.* **2008,** *8*, 3959-3963.

(28) Baik, S. J.; Kim, K.; Lim, K. S.; Jung, S.; Park, Y.-C.; Han, D. G.; Lim, S.; Yoo, S.; Jeong, S. Low-Temperature Annealing for Highly Conductive Lead Chalcogenide Quantum Dot Solids. *J. Phys. Chem. C* **2011,** *115*, 607-612.

(29) Eggleston, C. M.; Hochella, M. F. Scanning Tunneling Microscopy of Sulfide Surfaces. *Geochim. Cosmochim. Acta* **1990,** *54*, 1511-1517.

(30) Kaushik, A. P.; Lukose, B.; Clancy, P. The Role of Shape on Electronic Structure and Charge Transport in Faceted PbSe Nanocrystals. *ACS Nano* **2014,** *8*, 2302-2317.

(31) Nazin, G. V.; Wu, S. W.; Ho, W. Tunneling Rates in Electron Transport through Double-Barrier Molecular Junctions in a Scanning Tunneling Microscope. *Proc. Natl. Acad. Sci. U. S. A.* **2005,** *102*, 8832-8837.

(32) Nazin, G. V.; Qiu, X. H.; Ho, W. Vibrational Spectroscopy of Individual Doping Centers in a Monolayer Organic Crystal. *J. Chem. Phys.* **2005,** *122*, 181105.

(33) Nguyen, T. H.; Habinshuti, J.; Justo, Y.; Gomes, R.; Mahieu, G.; Godey, S.; Nys, J. P.; Carrillo, S.; Hens, Z.; Robbe, O., et al. Charge Carrier Identification in Tunneling Spectroscopy of Core-Shell Nanocrystals. *Phys. Rev. B* **2011,** *84*, 195133.

(34) Kim, D.; Kim, D.-H.; Lee, J.-H.; Grossman, J. C. Impact of Stoichiometry on the Electronic Structure of PbS Quantum Dots. *Phys. Rev. Lett.* **2013,** *110*, 196802.

(35) Becker, U.; Rosso, K. M. Step Edges on Galena (100): Probing the Basis for Defect Driven Surface Reactivity at the Atomic Scale. *Am. Mineral.* **2001,** *86*, 862-870.

(36) Moreels, I.; Lambert, K.; Smeets, D.; De Muynck, D.; Nollet, T.; Martins, J. C.; Vanhaecke, F.; Vantomme, A.; Delerue, C.; Allan, G., et al. Size-Dependent Optical Properties of Colloidal PbS Quantum Dots. *ACS Nano* **2009,** *3*, 3023-3030.

(37) Moreels, I.; Justo, Y.; De Geyter, B.; Haustraete, K.; Martins, J. C.; Hens, Z. Size-Tunable, Bright, and Stable PbS Quantum Dots: A Surface Chemistry Study. *ACS Nano* **2011,** *5*, 2004-2012.

(38) Nilius, N.; Wallis, T. M.; Ho, W. Development of One-Dimensional Band Structure in Artificial Gold Chains. *Science* **2002,** *297*, 1853-1856.

(39) Folsch, S.; Hyldgaard, P.; Koch, R.; Ploog, K. H. Quantum Confinement in Monatomic Cu Chains on Cu(111). *Phys. Rev. Lett.* **2004,** *92*, 056803.

(40) Fölsch, S.; Yang, J.; Nacci, C.; Kanisawa, K. Atom-by-Atom Quantum State Control in Adatom Chains on a Semiconductor. *Phys. Rev. Lett.* **2009,** *103*, 096104.

(41) Fang, C.; van Huis, M. A.; Vanmaekelbergh, D.; Zandbergen, H. W. Energetics of Polar and Nonpolar Facets of PbSe Nanocrystals from Theory and Experiment. *ACS Nano* **2009,** *4*, 211-218.

(42) Horcas, I.; Fernández, R.; Gómez-Rodríguez, J. M.; Colchero, J.; Gómez-Herrero, J.; Baro, A. M. Wsxm: A Software for Scanning Probe Microscopy and a Tool for Nanotechnology. *Rev. Sci. Instrum.* **2007,** *78*, 2432410.

REFERENCEES CITED FOR CHAPTER III

(1) McDonald, S. A.; Konstantatos, G.; Zhang, S. G.; Cyr, P. W.; Klem, E. J. D.; Levina, L.; Sargent, E. H. Solution-processed PbS quantum dot infrared photodetectors and photovoltaics. *Nature Materials* **2005,** *4* (2), 138-U14.

(2) Tang, J.; Liu, H.; Zhitomirsky, D.; Hoogland, S.; Wang, X. H.; Furukawa, M.; Levina, L.; Sargent, E. H. Quantum Junction Solar Cells. *Nano Letters* **2012,** *12* (9), 4889-4894.

(3) Klem, E. J. D.; MacNeil, D. D.; Cyr, P. W.; Levina, L.; Sargent, E. H. Efficient solution-processed infrared photovoltaic cells: Planarized all-inorganic bulk heterojunction devices via inter-quantum-dot bridging during growth from solution. *Applied Physics Letters* **2007,** *90* (18), 183113.

(4) Sun, L.; Choi, J. J.; Stachnik, D.; Bartnik, A. C.; Hyun, B.-R.; Malliaras, G. G.; Hanrath, T.; Wise, F. W. Bright infrared quantum-dot light-emitting diodes through inter-dot spacing control. *Nat Nano* **2012,** *7* (6), 369-373.

(5) Nozik, A. J. Spectroscopy and Hot Electron Relaxation Dynamics in Semiconductor Quantum Wells and Quantum Dots. *Annual Review of Physical Chemistry* **2001,** *52*, 193-231.

(6) Nozik, A. J. Quantum Dot Solar Cells. *Physica E-Low-Dimensional Systems & Nanostructures* **2002,** *14* (1-2), 115-120.

(7) Beard, M. C.; Ellingson, R. J. Multiple Exciton Generation in Semiconductor Nanocrystals: Toward Efficient Solar Energy Conversion. *Laser & Photonics Reviews* **2008,** *2* (5), 377-399.

(8) Beard, M. C.; Midgett, A. G.; Hanna, M. C.; Luther, J. M.; Hughes, B. K.; Nozik, A. J. Comparing Multiple Exciton Generation in Quantum Dots To Impact Ionization in Bulk Semiconductors: Implications for Enhancement of Solar Energy Conversion. *Nano Letters* **2010,** *10* (8), 3019-3027.

(9) Sandeep, C. S. S.; Cate, S. t.; Schins, J. M.; Savenije, T. J.; Liu, Y.; Law, M.; Kinge, S.; Houtepen, A. J.; Siebbeles, L. D. A. High Charge-Carrier Mobility Enables Exploitation of Carrier Multiplication in Quantum-Dot Films. *Nat Commun* **2013,** *4*, 2360.

(10) Sambur, J. B.; Novet, T.; Parkinson, B. A. Multiple Exciton Collection in a Sensitized Photovoltaic System. *Science* **2010,** *330* (6000), 63-66.

(11) Tisdale, W. A.; Williams, K. J.; Timp, B. A.; Norris, D. J.; Aydil, E. S.; Zhu, X. Y. Hot-Electron Transfer from Semiconductor Nanocrystals. *Science* **2010,** *328* (5985), 1543-1547.

(12) Liu, Y.; Gibbs, M.; Puthussery, J.; Gaik, S.; Ihly, R.; Hillhouse, H. W.; Law, M. Dependence of Carrier Mobility on Nanocrystal Size and Ligand Length in PbSe Nanocrystal Solids. *Nano Letters* **2010,** *10* (5), 1960-1969.

(13) Tang, J.; Kemp, K. W.; Hoogland, S.; Jeong, K. S.; Liu, H.; Levina, L.; Furukawa, M.; Wang, X. H.; Debnath, R.; Cha, D. K.; Chou, K. W.; Fischer, A.; Amassian, A.; Asbury, J. B.; Sargent, E. H. Colloidal-Quantum-Dot Photovoltaics Using Atomic-Ligand Passivation. *Nature Materials* **2011,** *10* (10), 765-771.

(14) Hughes, B. K.; Ruddy, D. A.; Blackburn, J. L.; Smith, D. K.; Bergren, M. R.; Nozik, A. J.; Johnson, J. C.; Beard, M. C. Control of PbSe Quantum Dot Surface Chemistry and Photophysics Using an Alkylselenide Ligand. *Acs Nano* **2012,** *6* (6), 5498-5506.

(15) Hetsch, F.; Zhao, N.; Kershaw, S. V.; Rogach, A. L. Quantum Dot Field Effect Transistors. *Materials Today* **2013,** *16* (9), 312-325.

(16) Kovalenko, M. V.; Scheele, M.; Talapin, D. V. Colloidal Nanocrystals with Molecular Metal Chalcogenide Surface Ligands. *Science* **2009,** *324* (5933), 1417-1420.

(17) Luther, J. M.; Law, M.; Song, Q.; Perkins, C. L.; Beard, M. C.; Nozik, A. J. Structural, Optical and Electrical Properties of Self-Assembled Films of PbSe Nanocrystals Treated with 1,2-Ethanedithiol. *Acs Nano* **2008,** *2* (2), 271-280.

(18) Ding, B.; Wang, Y.; Huang, P.-S.; Waldeck, D. H.; Lee, J.-K. Depleted Bulk Heterojunctions in Thermally Annealed PbS Quantum Dot Solar Cells. *The Journal of Physical Chemistry C* **2014,** *118* (27), 14749-14758.

(19) Baik, S. J.; Kim, K.; Lim, K. S.; Jung, S.; Park, Y.-C.; Han, D. G.; Lim, S.; Yoo, S.; Jeong, S. Low-Temperature Annealing for Highly Conductive Lead Chalcogenide Quantum Dot Solids. *Journal of Physical Chemistry C* **2011,** *115* (3), 607-612.

(20) van Huis, M. A.; Kunneman, L. T.; Overgaag, K.; Xu, Q.; Pandraud, G.; Zandbergen, H. W.; Vanmaekelbergh, D. Low-Temperature Nanocrystal Unification through Rotations and Relaxations Probed by in Situ Transmission Electron Microscopy. *Nano Letters* **2008,** *8* (11), 3959-3963.

(21) Talapin, D. V.; Lee, J.-S.; Kovalenko, M. V.; Shevchenko, E. V. Prospects of Colloidal Nanocrystals for Electronic and Optoelectronic Applications. *Chemical Reviews* **2010,** *110* (1), 389-458.

(22) Ip, A. H.; Thon, S. M.; Hoogland, S.; Voznyy, O.; Zhitomirsky, D.; Debnath, R.; Levina, L.; Rollny, L. R.; Carey, G. H.; Fischer, A.; Kemp, K. W.; Kramer, I. J.; Ning, Z. J.; Labelle, A. J.; Chou, K. W.; Amassian, A.; Sargent, E. H. Hybrid Passivated Colloidal Quantum Dot Solids. *Nature Nanotechnology* **2012,** *7* (9), 577-582.

(23) Zhitomirsky, D.; Kramer, I. J.; Labelle, A. J.; Fischer, A.; Debnath, R.; Pan, J.; Bakr, O. M.; Sargent, E. H. Colloidal Quantum Dot Photovoltaics: The Effect of Polydispersity. *Nano Letters* **2012,** *12* (2), 1007-1012.

(24) Carey, G. H.; Kramer, I. J.; Kanjanaboos, P.; Moreno-Bautista, G.; Voznyy, O.; Rollny, L.; Tang, J. A.; Hoogland, S.; Sargent, E. H. Electronically Active Impurities in Colloidal Quantum Dot Solids. *Acs Nano* **2014,** *8* (11), 11763-11769.

(25) Thon, S. M.; Ip, A. H.; Voznyy, O.; Levina, L.; Kemp, K. W.; Carey, G. H.; Masala, S.; Sargent, E. H. Role of Bond Adaptability in the Passivation of Colloidal Quantum Dot Solids. *ACS Nano* **2013,** *7* (9), 7680-7688.

(26) Chuang, C.-H. M.; Brown, P. R.; Bulović, V.; Bawendi, M. G. Improved Performance and Stability in Quantum Dot Solar Cells through Band Alignment Engineering. *Nat Mater* **2014,** *13* (8), 796-801.

(27) Ning, Z. J.; Voznyy, O.; Pan, J.; Hoogland, S.; Adinolfi, V.; Xu, J. X.; Li, M.; Kirmani, A. R.; Sun, J. P.; Minor, J.; Kemp, K. W.; Dong, H. P.; Rollny, L.; Labelle, A.; Carey, G.; Sutherland, B.; Hill, I.; Amassian, A.; Liu, H.; Tang, J.; Bakr, O. M.; Sargent, E. H. Air-Stable N-Type Colloidal Quantum Dot Solids. *Nature Materials* **2014,** *13* (8), 822-828.

(28) Fernee, M. J.; Thomsen, E.; Jensen, P.; Rubinsztein-Dunlop, H. Highly Efficient Luminescence from a Hybrid State Found in Strongly Quantum Confined PbS Nanocrystals. *Nanotechnology* **2006,** *17* (4), 956-962.

(29) Gao, J.; Johnson, J. C. Charge Trapping in Bright and Dark States of Coupled PbS Quantum Dot Films. *Acs Nano* **2012,** *6* (4), 3292-3303.

(30) Nelson, C. A.; Zhu, X. Y. Reversible Surface Electronic Traps in PbS Quantum Dot Solids Induced by an Order–Disorder Phase Transition in Capping Molecules. *Journal of the American Chemical Society* **2012,** *134* (18), 7592-7595.

(31) Jeong, K. S.; Tang, J.; Liu, H.; Kim, J.; Schaefer, A. W.; Kemp, K.; Levina, L.; Wang, X. H.; Hoogland, S.; Debnath, R.; Brzozowski, L.; Sargent, E. H.; Asbury, J. B. Enhanced Mobility-Lifetime Products in PbS Colloidal Quantum Dot Photovoltaics. *ACS Nano* **2012,** *6* (1), 89-99.

(32) Bozyigit, D.; Volk, S.; Yarema, O.; Wood, V. Quantification of Deep Traps in Nanocrystal Solids, Their Electronic Properties, and Their Influence on Device Behavior. *Nano Letters* **2013,** *13* (11), 5284-5288.

(33) Nagpal, P.; Klimov, V. I. Role of Mid-Gap States in Charge Transport and Photoconductivity in Semiconductor Nanocrystal Films. *Nature Communications* **2011,** *2*, 486.

(34) Diaconescu, B.; Padilha, L. A.; Nagpal, P.; Swartzentruber, B. S.; Klimov, V. I. Measurement of Electronic States of PbS Nanocrystal Quantum Dots Using Scanning Tunneling Spectroscopy: The Role of Parity Selection Rules in Optical Absorption. *Physical Review Letters* **2013,** *110* (12), 127406.

(35) Hackley, J. D.; Kislitsyn, D. A.; Beaman, D. K.; Ulrich, S.; Nazin, G. V. High-Stability Cryogenic Scanning Tunneling Microscope Based on a Closed-Cycle Cryostat. *Review of Scientific Instruments* **2014,** *85* (10), 103704.

(36) Kislitsyn, D. A.; Gervasi, C. F.; Allen, T.; Palomaki, P. K. B.; Hackley, J. D.; Maruyama, R.; Nazin, G. V. Spatial Mapping of Sub-Bandgap States Induced by Local Nonstoichiometry in Individual Lead Sulfide Nanocrystals. *Journal of Physical Chemistry Letters* **2014,** *5* (21), 3701-3707.

(37) Kilina, S. V.; Craig, C. F.; Kilin, D. S.; Prezhdo, O. V. Ab Initio Time-Domain Study of Phonon-Assisted Relaxation of Charge Carriers in a PbSe Quantum Dot. *Journal of Physical Chemistry C* **2007,** *111* (12), 4871-4878.

(38) Kilina, S. V.; Kilin, D. S.; Prezhdo, O. V. Breaking the Phonon Bottleneck in PbSe and CdSe Quantum Dots: Time-Domain Density Functional Theory of Charge Carrier Relaxation. *ACS Nano* **2008,** *3* (1), 93-99.

(39) Kaushik, A. P.; Lukose, B.; Clancy, P. The Role of Shape on Electronic Structure and Charge Transport in Faceted PbSe Nanocrystals. *Acs Nano* **2014,** *8* (3), 2302-2317.

(40) Fang, C.; van Huis, M. A.; Vanmaekelbergh, D.; Zandbergen, H. W. Energetics of Polar and Nonpolar Facets of PbSe Nanocrystals from Theory and Experiment. *Acs Nano* **2009,** *4* (1), 211-218.

(41) Kim, D.; Kim, D.-H.; Lee, J.-H.; Grossman, J. C. Impact of Stoichiometry on the Electronic Structure of PbS Quantum Dots. *Physical Review Letters* **2013,** *110* (19), 196802.

(42) Yang, J.; Elim, H. I.; Zhang, Q.; Lee, J. Y.; Ji, W. Rational Synthesis, Self-Assembly, and Optical Properties of PbS−Au Heterogeneous Nanostructures via Preferential Deposition. *Journal of the American Chemical Society* **2006,** *128* (36), 11921-11926.

(43) Chen, C. J. *Introduction to Scanning Tunneling Microscopy*. Second Edition ed.; Oxford University Press: New York, 2008.

(44) Banin, U.; Cao, Y. W.; Katz, D.; Millo, O. Identification of atomic-like electronic states in indium arsenide nanocrystal quantum dots. *Nature* **1999,** *400* (6744), 542-544.

(45) Moreels, I.; Lambert, K.; Smeets, D.; De Muynck, D.; Nollet, T.; Martins, J. C.; Vanhaecke, F.; Vantomme, A.; Delerue, C.; Allan, G.; Hens, Z. Size-Dependent Optical Properties of Colloidal PbS Quantum Dots. *Acs Nano* **2009,** *3* (10), 3023-3030.

(46) Lee, W.; Dasgupta, N. P.; Jung, H. J.; Lee, J. R.; Sinclair, R.; Prinz, F. B. Scanning tunneling spectroscopy of lead sulfide quantum wells fabricated by atomic layer deposition. *Nanotechnology* **2010,** *21* (48).

(47) Hens, Z.; Vanmaekelbergh, D.; Stoffels, E.; van Kempen, H. Effects of Crystal Shape on the Energy Levels of Zero-Dimensional PbS Quantum Dots. *Physical Review Letters* **2002,** *88* (23), 236803.

(48) Jdira, L.; Liljeroth, P.; Stoffels, E.; Vanmaekelbergh, D.; Speller, S. Size-dependent single-particle energy levels and interparticle Coulomb interactions in CdSe quantum dots measured by scanning tunneling spectroscopy. *Physical Review B* **2006,** *73* (11).

(49) Dasgupta, N. P.; Lee, W.; Prinz, F. B. Atomic Layer Deposition of Lead Sulfide Thin Films for Quantum Confinement. *Chemistry of Materials* **2009,** *21* (17), 3973-3978.

(50) Voznyy, O.; Thon, S. M.; Ip, A. H.; Sargent, E. H. Dynamic Trap Formation and Elimination in Colloidal Quantum Dots. *Journal of Physical Chemistry Letters* **2013,** *4* (6), 987-992.

(51) Krauss, T. D.; Wise, F. W.; Tanner, D. B. Observation of Coupled Vibrational Modes of a Semiconductor Nanocrystal. *Physical Review Letters* **1996,** *76* (8), 1376-1379.

(52) Sun, Z. X.; Swart, I.; Delerue, C.; Vanmaekelbergh, D.; Liljeroth, P. Orbital and Charge-Resolved Polaron States in CdSe Dots and Rods Probed by Scanning Tunneling Spectroscopy. *Physical Review Letters* **2009,** *102* (19), 196401.

(53) Nilius, N.; Wallis, T. M.; Ho, W. Development of One-Dimensional Band Structure in Artificial Gold Chains. *Science* **2002,** *297* (5588), 1853-1856.

(54) Folsch, S.; Hyldgaard, P.; Koch, R.; Ploog, K. H. Quantum confinement in monatomic Cu chains on Cu(111). *Physical Review Letters* **2004,** *92* (5), 056803.

(55) Fölsch, S.; Yang, J.; Nacci, C.; Kanisawa, K. Atom-By-Atom Quantum State Control in Adatom Chains on a Semiconductor. *Physical Review Letters* **2009,** *103* (9), 096104.

(56) Moreels, I.; Justo, Y.; De Geyter, B.; Haustraete, K.; Martins, J. C.; Hens, Z. Size-Tunable, Bright, and Stable PbS Quantum Dots: A Surface Chemistry Study. *Acs Nano* **2011,** *5* (3), 2004-2012.

(57) Kilina, S.; Ivanov, S.; Tretiak, S. Effect of Surface Ligands on Optical and Electronic Spectra of Semiconductor Nanoclusters. *Journal of the American Chemical Society* **2009,** *131* (22), 7717-7726.

(58) Margraf, J. T.; Ruland, A.; Sgobba, V.; Guldi, D. M.; Clark, T. Theoretical and Experimental Insights into the Surface Chemistry of Semiconductor Quantum Dots. *Langmuir* **2013,** *29* (49), 15450-15456.

(59) Horcas, I.; Fernández, R.; Gómez-Rodríguez, J. M.; Colchero, J.; Gómez-Herrero, J.; Baro, A. M. WSXM: A Software for Scanning Probe Microscopy and a Tool for Nanotechnology. *Review of Scientific Instruments* **2007,** *78* (1), 2432410.

REFERENCES CITED FOR CHAPTER IV

(1) Chuang, C.-H. M.; Brown, P. R.; Bulović, V.; Bawendi, M. G. Improved Performance and Stability in Quantum Dot Solar Cells through Band Alignment Engineering. *Nat Mater* **2014,** *13* (8), 796-801.

(2) Ning, Z. J.; Voznyy, O.; Pan, J.; Hoogland, S.; Adinolfi, V.; Xu, J. X.; Li, M.; Kirmani, A. R.; Sun, J. P.; Minor, J.; Kemp, K. W.; Dong, H. P.; Rollny, L.; Labelle, A.; Carey, G.; Sutherland, B.; Hill, I.; Amassian, A.; Liu, H.; Tang, J.; Bakr, O. M.; Sargent, E. H. Air-Stable N-Type Colloidal Quantum Dot Solids. *Nature Materials* **2014,** *13* (8), 822-828.

(3) Liu, Y.; Gibbs, M.; Puthussery, J.; Gaik, S.; Ihly, R.; Hillhouse, H. W.; Law, M. Dependence of Carrier Mobility on Nanocrystal Size and Ligand Length in PbSe Nanocrystal Solids. *Nano Letters* **2010,** *10* (5), 1960-1969.

(4) Liu, Y.; Tolentino, J.; Gibbs, M.; Ihly, R.; Perkins, C. L.; Liu, Y.; Crawford, N.; Hemminger, J. C.; Law, M. PbSe Quantum Dot Field-Effect Transistors with Air-Stable Electron Mobilities above 7 cm(2) V-1 s(-1). *Nano Letters* **2013,** *13* (4), 1578-1587.

(5) Thon, S. M.; Ip, A. H.; Voznyy, O.; Levina, L.; Kemp, K. W.; Carey, G. H.; Masala, S.; Sargent, E. H. Role of Bond Adaptability in the Passivation of Colloidal Quantum Dot Solids. *ACS Nano* **2013,** *7* (9), 7680-7688.

(6) Tang, J.; Kemp, K. W.; Hoogland, S.; Jeong, K. S.; Liu, H.; Levina, L.; Furukawa, M.; Wang, X. H.; Debnath, R.; Cha, D. K.; Chou, K. W.; Fischer, A.; Amassian, A.; Asbury, J. B.; Sargent, E. H. Colloidal-Quantum-Dot Photovoltaics Using Atomic-Ligand Passivation. *Nature Materials* **2011,** *10* (10), 765-771.

(7) Soreni-Harari, M.; Yaacobi-Gross, N.; Steiner, D.; Aharoni, A.; Banin, U.; Millo, O.; Tessler, N. Tuning energetic levels in nanocrystal quantum dots through surface manipulations. *Nano Letters* **2008,** *8* (2), 678-684.

(8) Brown, P. R.; Kim, D.; Lunt, R. R.; Zhao, N.; Bawendi, M. G.; Grossman, J. C.; Bulovi, V. Energy level modification in lead sulfide quantum dot thin films through ligand exchange. *ACS Nano* **2014,** *8* (6), 5863-5872.

(9) Ding, B.; Wang, Y.; Huang, P.-s.; Waldeck, D. H.; Lee, J.-k. Depleted Bulk Heterojunctions in Thermally Annealed PbS Quantum Dot Solar Cells Depleted Bulk Heterojunctions in Thermally Annealed PbS Quantum Dot Solar Cells**2014**.

(10) Hetsch, F.; Zhao, N.; Kershaw, S. V.; Rogach, A. L. Quantum Dot Field Effect Transistors. *Materials Today* **2013,** *16* (9), 312-325.

(11) Kovalenko, M. V.; Scheele, M.; Talapin, D. V. Colloidal Nanocrystals with Molecular Metal Chalcogenide Surface Ligands. *Science* **2009,** *324* (5933), 1417-1420.

(12) Popescu, V.; Zunger, A. Extracting E versus (k)over-right-arrow effective band structure from supercell calculations on alloys and impurities. *Physical Review B* **2012,** *85* (8).

(13) Choi, M. J.; García de Arquer, F. P.; Proppe, A. H.; Seifitokaldani, A.; Choi, J.; Kim, J.; Baek, S. W.; Liu, M.; Sun, B.; Biondi, M.; Scheffel, B.; Walters, G.; Nam, D. H.; Jo, J. W.; Ouellette, O.; Voznyy, O.; Hoogland, S.; Kelley, S. O.; Jung, Y. S.; Sargent, E. H. Cascade surface modification of colloidal quantum dot inks enables efficient bulk homojunction photovoltaics. *Nat Commun* **2020,** *11* (1), 103.

(14) Zhitomirsky, D.; Kramer, I. J.; Labelle, A. J.; Fischer, A.; Debnath, R.; Pan, J.; Bakr, O. M.; Sargent, E. H. Colloidal Quantum Dot Photovoltaics: The Effect of Polydispersity. *Nano Letters* **2012,** *12* (2), 1007-1012.

(15) Talapin, D. V.; Lee, J.-S.; Kovalenko, M. V.; Shevchenko, E. V. Prospects of Colloidal Nanocrystals for Electronic and Optoelectronic Applications. *Chemical Reviews* **2010,** *110* (1), 389-458.

(16) Ip, A. H.; Thon, S. M.; Hoogland, S.; Voznyy, O.; Zhitomirsky, D.; Debnath, R.; Levina, L.; Rollny, L. R.; Carey, G. H.; Fischer, A.; Kemp, K. W.; Kramer, I. J.; Ning, Z. J.; Labelle, A. J.; Chou, K. W.; Amassian, A.; Sargent, E. H. Hybrid Passivated Colloidal Quantum Dot Solids. *Nature Nanotechnology* **2012,** *7* (9), 577-582.

(17) Gao, J.; Johnson, J. C. Charge Trapping in Bright and Dark States of Coupled PbS Quantum Dot Films. *Acs Nano* **2012,** *6* (4), 3292-3303.

(18) Jeong, K. S.; Tang, J.; Liu, H.; Kim, J.; Schaefer, A. W.; Kemp, K.; Levina, L.; Wang, X. H.; Hoogland, S.; Debnath, R.; Brzozowski, L.; Sargent, E. H.; Asbury, J. B. Enhanced Mobility-Lifetime Products in PbS Colloidal Quantum Dot Photovoltaics. *ACS Nano* **2012,** *6* (1), 89-99.

(19) Nelson, C. a.; Zhu, X. Y. Reversible surface electronic traps in PbS quantum dot solids induced by an order-disorder phase transition in capping molecules. *Journal of the American Chemical Society* **2012,** *134* (18), 7592-7595.

(20) Bozyigit, D.; Volk, S.; Yarema, O.; Wood, V. Quantification of Deep Traps in Nanocrystal Solids, Their Electronic Properties, and Their Influence on Device Behavior. *Nano Letters* **2013,** *13* (11), 5284-5288.

(21) Diaconescu, B.; Padilha, L. A.; Nagpal, P.; Swartzentruber, B. S.; Klimov, V. I. Measurement of Electronic States of PbS Nanocrystal Quantum Dots Using Scanning Tunneling Spectroscopy: The Role of Parity Selection Rules in Optical Absorption. *Physical Review Letters* **2013,** *110* (12), 127406.

(22) Gervasi, C. F.; Kislitsyn, D. A.; Allen, T. L.; Hackley, J. D.; Maruyama, R.; Nazin, G. V. Diversity of sub-bandgap states in lead-sulfide nanocrystals: real-space spectroscopy and mapping at the atomic-scale. *Nanoscale* **2015,** *7* (46), 19732-19742.

(23) Kislitsyn, D. A.; Gervasi, C. F.; Allen, T.; Palomaki, P. K. B.; Hackley, J. D.; Maruyama, R.; Nazin, G. V. Spatial Mapping of Sub-Bandgap States Induced by Local Nonstoichiometry in Individual Lead Sul fi de Nanocrystals. *Journal of Physical Chemistry Letters* **2014,** *5*, 3701-3707.

(24) Nagpal, P.; Klimov, V. I. Role of Mid-Gap States in Charge Transport and Photoconductivity in Semiconductor Nanocrystal Films. *Nature Communications* **2011,** *2*, 486.

(25) Gai, Y.; Peng, H.; Li, J. Electronic Properties of Nonstoichiometric PbSe Quantum Dots from First Principles. *Journal of Physical Chemistry C* **2009,** *113* (52), 21506-21511.

(26) Kim, D.; Kim, D.-H.; Lee, J.-H.; Grossman, J. C. Impact of Stoichiometry on the Electronic Structure of PbS Quantum Dots. *Physical Review Letters* **2013,** *110* (19), 196802.

(27) Yang, J.; Elim, H. I.; Zhang, Q.; Lee, J. Y.; Ji, W. Rational synthesis, self-assembly, and optical properties of PbS-Au heterogeneous nanostructures via preferential deposition. *Journal of the American Chemical Society* **2006,** *128* (36), 11921-11926.

(28) Hens, Z.; Vanmaekelbergh, D.; Stoffels, E.; van Kempen, H. Effects of Crystal Shape on the Energy Levels of Zero-Dimensional PbS Quantum Dots. *Physical Review Letters* **2002,** *88* (23), 236803.

(29) Hens, Z.; Kooij, E. S.; Allan, G.; Grandidier, B.; Vanmaekelbergh, D. Electrodeposited nanocrystalline PbSe quantum wells: synthesis, electrical and optical properties. *Nanotechnology* **2005,** *16* (4), 339-343.

(30) Chen, C. J. *Introduction to Scanning Tunneling Microscopy*. Second Edition ed.; Oxford University Press: New York, 2008.

(31) Moreels, I.; Lambert, K.; Smeets, D.; De Muynck, D.; Nollet, T.; Martins, J. C.; Vanhaecke, F.; Vantomme, A.; Delerue, C.; Allan, G.; Hens, Z. Size-Dependent Optical Properties of Colloidal PbS Quantum Dots. *Acs Nano* **2009,** *3* (10), 3023-3030.

(32) Lee, W.; Dasgupta, N. P.; Jung, H. J.; Lee, J. R.; Sinclair, R.; Prinz, F. B. Scanning tunneling spectroscopy of lead sulfide quantum wells fabricated by atomic layer deposition. *Nanotechnology* **2010,** *21* (48).

(33) Kimura, K.; Nakajima, K.; Fujii, Y.; Mannami, M. OBSERVATION OF THE PBSE(111) SURFACE USING HIGH-RESOLUTION RUTHERFORD BACKSCATTERING SPECTROSCOPY. *Surface Science* **1994,** *318* (3), 363-367.

(34) Fang, C.; van Huis, M. A.; Vanmaekelbergh, D.; Zandbergen, H. W. Energetics of Polar and Nonpolar Facets of PbSe Nanocrystals from Theory and Experiment. *Acs Nano* **2009,** *4* (1), 211-218.

(35) Deringer, V. L.; Dronskowski, R. Stabilities and Reconstructions of Clean PbS and PbSe Surfaces: DFT Results and the Role of Dispersion Forces. *Journal of Physical Chemistry C* **2016,** *120* (16), 8813-8820.

(36) Giannozzi, P.; Andreussi, O.; Brumme, T.; Bunau, O.; Buongiorno Nardelli, M.; Calandra, M.; Car, R.; Cavazzoni, C.; Ceresoli, D.; Cococcioni, M.; Colonna, N.; Carnimeo, I.; Dal Corso, A.; de Gironcoli, S.; Delugas, P.; DiStasio, R. A.; Ferretti, A.; Floris, A.; Fratesi, G.; Fugallo, G.; Gebauer, R.; Gerstmann, U.; Giustino, F.; Gorni, T.; Jia, J.; Kawamura, M.; Ko, H. Y.; Kokalj, A.; Küçükbenli, E.; Lazzeri, M.; Marsili, M.; Marzari, N.; Mauri, F.; Nguyen, N. L.; Nguyen, H. V.; Otero-de-la-Roza, A.; Paulatto, L.; Poncé, S.; Rocca, D.; Sabatini, R.; Santra, B.; Schlipf, M.; Seitsonen, A. P.; Smogunov, A.; Timrov, I.; Thonhauser, T.; Umari, P.; Vast, N.; Wu, X.; Baroni, S. Advanced capabilities for materials modelling with Quantum ESPRESSO. *J Phys Condens Matter* **2017,** *29* (46), 465901.

(37) Medeiros, P. V. C.; Stafstrom, S.; Bjork, J. Effects of extrinsic and intrinsic perturbations on the electronic structure of graphene: Retaining an effective primitive cell band structure by band unfolding. *Physical Review B* **2014,** *89* (4).

(38) Inglesfield; E, J. Surface Electronic Structure. *Reports on Progress in Physics* **1982,** *45* (3).

(39) Smidstrup, S.; Markussen, T.; Vancraeyveld, P.; Wellendorff, J.; Schneider, J.; Gunst, T.; Verstichel, B.; Stradi, D.; Khomyakov, P. A.; Vej-Hansen, U. G.; Lee, M. E.; Chill, S. T.; Rasmussen, F.; Penazzi, G.; Corsetti, F.; Ojanperä, A.; Jensen, K.; Palsgaard, M. L. N.; Martinez, U.; Blom, A.; Brandbyge, M.; Stokbro, K. QuantumATK: an integrated platform of electronic and atomic-scale modelling tools. *J Phys Condens Matter* **2020,** *32* (1), 015901.

(40) Stradi, D.; Jelver, L.; Smidstrup, S.; Stokbro, K. Method for determining optimal supercell representation of interfaces. *Journal of Physics: Condensed Matter* **2017,** *29* (18), 185901

(41) Perdew, J. P.; Burke, K.; Ernzerhof, M. Generalized gradient approximation made simple. *Physical Review Letters* **1996,** *77* (18), 3865-3868.

(42) Shishkin, M.; Kresse, G. Self-consistent GW calculations for semiconductors and insulators. *Physical Review B* **2007,** *75* (23).

(43) Blöchl, P. E. Projector augmented-wave method. *Physical Review B* **1994,** *50* (24), 17953-17979.

(44) Kresse, G.; Furthmuller, J. Efficient iterative schemes for ab initio total-energy calculations using a plane-wave basis set. *Physical Review B* **1996,** *54* (16), 11169-11186.

(45) Peng, H. W.; Song, J. H.; Kanatzidis, M. G.; Freeman, A. J. Electronic structure and transport properties of doped PbSe. *Physical Review B* **2011,** *84* (12).

(46) Monkhorst, H. J.; Pack, J. D. SPECIAL POINTS FOR BRILLOUIN-ZONE INTEGRATIONS. *Physical Review B* **1976,** *13* (12), 5188-5192.

(47) Kaushik, A. P.; Lukose, B.; Clancy, P. The Role of Shape on Electronic Structure and Charge Transport in Faceted PbSe Nanocrystals. *Acs Nano* **2014,** *8* (3), 2302-2317.

(48) Moreels, I.; Justo, Y.; De Geyter, B.; Haustraete, K.; Martins, J. C.; Hens, Z. Size-Tunable, Bright, and Stable PbS Quantum Dots: A Surface Chemistry Study. *Acs Nano* **2011,** *5* (3), 2004-2012.

(49) Inglesfield, J. E. Surface Electronic Structure. *Reports on Progress in Physics* **1982,** *45* (3).

(50) Wei, S.-H.; Zunger, A. Electronic and structural anomalies in lead chalcogenides. *Physical Review B* **1997,** *55* (20), 6.

(51) Kang, I.; Wise, F. Electronic structure and optical properties of PbS and PbSe quantum dots. *J. Opt. Soc. Am. B* **1997,** *14* (7), 1632-1646.

(52) Kislitsyn, D. A.; Gervasi, C. F.; Allen, T.; Palomaki, P. K. B.; Hackley, J. D.; Maruyama, R.; Nazin, G. V. Spatial Mapping of Sub-Bandgap States Induced by Local Nonstoichiometry in Individual Lead Sulfide Nanocrystals. *Journal of Physical Chemistry Letters* **2014,** *5* (21), 3701-3707.

(53) Davison, S. G.; Stęślicka, M. *Basic theory of surface states*. Clarendon Press ;

Oxford University Press: Oxford, New York, 1992; p xiii, 223 p.

(54) Popescu, V.; Zunger, A. Effective band structure of random alloys. *Phys Rev Lett* **2010,** *104* (23), 236403.

(55) Ku, W.; Berlijn, T.; Lee, C. C. Unfolding first-principles band structures. *Phys Rev Lett* **2010,** *104* (21), 216401.

(56) Allen, P. B.; Berlijn, T.; Casavant, D. A.; Soler, J. M. Recovering Hidden Bloch character: Unfolding electrons, phonons, and slabs. *Physical Review B* **2013,** *87* (8).

REFERENCES CITED FOR APPENDIX A

(1) Nazin, G. V.; Wu, S. W.; Ho, W. Tunnelling Rates in Electron Transport through Double-Barrier Molecular Junctions in a Scanning Tunnelling Microscope. Proc. Natl. Acad. Sci. U. S. A. 2005, 102, 8832-8837.

(2) Wu, S. W.; Nazin, G. V.; Chen, X.; Qiu, X. H.; Ho, W. Control of Relative Tunnelling Rates in Single Molecule Bipolar Electron Transport. Phys. Rev. Lett. 2004, 93, 236802.

(3) Nazin, G. V.; Qiu, X. H.; Ho, W. Vibrational Spectroscopy of Individual Doping Centers in a Monolayer Organic Crystal. J. Chem. Phys. 2005, 122, 181105.

(4) Hines, M. A.; Scholes, G. D. Colloidal PbS Nanocrystals with Size-Tunable Near-Infrared Emission: Observation of Post-Synthesis Self-Narrowing of the Particle Size Distribution. Adv. Mat. 2003, 15 (21), 1844-1849.

(5) Moreels, I.; Lambert, K.; Smeets, D.; De Muynck, D.; Nollet, T.; Martins, J. C.; Vanhaecke, F.; Vantomme, A.; Delerue, C.; Allen, G.; Hens, Z. Size-Dependent Optical Properties of Colloidal PbS Quantum Dots. ACS Nano, 2009, 3 (10), 3023–3030

REFERENCES CITED FOR APPENDIX B

(1) Kim, D.; Kim, D.-H.; Lee, J.-H.; Grossman, J. C. Impact of Stoichiometry on the Electronic Structure of Pbs Quantum Dots. Physical Review Letters 2013, 110, 196802.